



銅管の蟻巣腐食の調査と微分分極法を用いた銅電極の交換電流密度の推定

メタデータ	言語: eng 出版者: 公開日: 2020-06-08 キーワード (Ja): キーワード (En): 作成者: リキ, ステパヌス スイトウモラン メールアドレス: 所属:
URL	https://doi.org/10.15118/00010188

**Investigation of Ant Nest Corrosion on Copper Tube
and Estimation of Exchange Current Density on
Copper Electrode by Using Differentiating Polarization
Method**

Riky Stepanus Situmorang



**Graduate School of Engineering
Division of Production System Engineering
Muroran Institute of Technology
Muroran Hokkaido, Japan
2020**

**Investigation of Ant Nest Corrosion on Copper Tube
and Estimation of Exchange Current Density on
Copper Electrode by Using Differentiating Polarization
Method**

by

Riky Stepanus Situmorang

DISSERTATION

Submitted in partial fulfillment of the requirements for the degree

DOCTOR OF ENGINEERING

**Graduate School of Engineering
Division of Production System Engineering
Muroran Institute of Technology
Muroran Hokkaido, Japan
2020**

博士論文題目

銅管の蟻巣腐食の調査と微分分極法を用いた銅電極の交換電流密度の推定

氏 名 :

RIKY STEPANUS SITUMORANG

論文内容の要旨

家電製品やコンピュータ、車の電子化などエレクトロニクスの著しい発展や熱交換器の高性能化によって銅材料の用途は増加の一途を辿り、銅腐食の形態も多岐に渡っている。エンジンなどの構成材料を強化するために用いられる銅配合合金もバイオマス化による新たな燃焼形態によって腐食モードが異なる場合が見られる。ここでは銅材料の腐食形態で最近深刻な問題を引き起こしている「蟻巣腐食」を実験的に再現し、そのメカニズムについて考察する。また金属腐食に見られる水素発生反応を、より高精度な微分分極法によって解析し燃料電池などの電極開発に指針を与える基礎データを示した。

またバイオマス燃料化の一環として液体燃料とメタンガスを併用する「デュアルフェューエルモード」を取り上げ、エンジン燃焼試験を実施して燃焼効率などを測定し、これら燃焼形態が材料に及ぼす腐食の可能性について基礎実験を通して考察した。

1. 銅管で最近注目される蟻巣腐食 (ANC) のメカニズムはまだ明確には解っていない。我々は銅試料をギ酸銅溶液(10^3 ppm)に 20 日間浸漬することによる腐食電位と pH 値の変化を測定し、表面観察、断面観察、pH 測定、電気化学測定を実施した。これより、Disproportionation 反応と Comproportionation 反応が ANC メカニズムの解明のために重要な要因となることを示した。更に分極抵抗曲線によって、ANC は腐食速度の大きい高速反応系であることがわかった。
2. 銅電極は、水素発生反応 (HER) の有望な電極である。電極の触媒性能の計算には HER の交換電流密度 (i_0) が用いられるが一般的なターフェル外挿法 (TEM) では、勾配の読み取りが不正確であり、且つ電極表面に発生する物理的な抵抗の評価計算にも問題がある。この点を改良した微分分極法 (DPM) を用い、 $0.5 \text{ mol dm}^{-3} \text{ H}_2\text{SO}_4$ 溶液中の銅電極の HER を測定した。この結果 DPM では TEM より高い精度を有すること、誤差要因である物理抵抗を合理的に除去できることから、ターフェルスローブ領域を正確に読み取ることができた。

3. 本研究ではバイオ燃料(BDF)、並びにメタンガスと CO₂ の成分比率を人工的に調整したバイオガス (メタン比率 40~100%) を Dual Fuel(DF)に見立てて燃焼実験を行い熱発生率、燃焼安定度などの燃焼特性を測定した。実験では低トルク(3.5Nm)から高トルク(24.6Nm)の 4 条件で負荷を変化させ、回転数 1800~2600 rpm の 5 条件で実施した。この結果、低負荷運転時の DFM において正味熱効率は低下し、バイオディーゼル置換率、バイオガスエネルギー率、燃料消費率は増加した。これより DF モードではメタンの影響を大きく受けること、バイオガス中の二酸化炭素は正味熱効率を上昇させる効果があることが示された。全条件において燃焼安定度は 1.7-4.89 %の間であり、実用化において許容できる値であった。

Abstract

The high increasing application of copper due to its advantages attract the author to do research on copper. In addition, research about dual fuel mode in a diesel engine also discussed as follows:

1. Ant nest corrosion (ANC) had been found and observed on the copper tube in the air conditioner. However, the mechanism of ANC is still unclear explained. In order to understand the mechanism and behavior of the ANC, a research investigation of ANC on the copper tube was conducted in terms of the variables of the corrosion potential and pH value in 10^3 ppm copper formate solution over 20 days. The surface observation, cross-sectional observation, daily pH measurement, and electrochemical measurements were conducted in this research. By using all these results, the author explains the mechanisms of the ANC. It was found that Cannizzaro and Comproportionation reaction critically influenced the ANC mechanism.
2. The copper electrode is still a promising electrode in the hydrogen evolution reaction (HER). The Tafel extrapolation method (TEM) is commonly used for the estimation of the exchange current density (i_0) on the HER. However, TEM is still hindered because of some issues, such as the improper reading of Tafel slope and the influence of physical resistant. The differential polarization method (DPM) was introduced in this dissertation as a reliable method to estimate the value of the i_0 . The research was conducted a measurement of HER on copper electrode in $0.5 \text{ mol dm}^{-3} \text{ H}_2\text{SO}_4$ solution. The value of i_0 is calculated using both methods; the TEM and the DPM. It found that the DPM is a promising method in the calculation of i_0 .
3. Biodiesel fuel and biogas fuel as promising alternative energy sources for dual-fuel mode(DFM) diesel engine attract more researchers. Therefore, The DFM operation

of diesel engine using biodiesel fuel from used cooking oil and simulated biogas fuel with different methane contents were conducted and focused on the combustion, rate of heat release, combustion stability, and performance. The observation of diesel engine was conducted by varying the torques and engine speeds. The relation of the results of biodiesel replacement, biogas energy ratio, and brake thermal efficiency with methane content ratio in DFM show that the methane content ratio has the maximum effect in DFM. In addition, the carbon dioxide content in the biogas can enrich the brake thermal efficiency. The combustion stability of all conditions is from 1.7% to 4.89%, which is still acceptable.

Table of Contents

Abstract	i
Table of Contents	v
List of Tables.....	ix
List of Figures	x
Abbreviations	xv
Chapter 1 Introduction	1
1.1 Copper Element	2
1.2 Motivation of the Study	3
1.3 Scope of the research	5
1.3.1 Scope of the Study on Ant-Nest Corrosion on Copper tube	5
1.3.2 Scope of the Study of current density on Coper Electrode	5
1.3.3 Scope of the Study of Dual-fuel Mode in a Small Diesel Engine	6
Reference	6
Chapter 2 Ant-Nest Corrosion Mechanism	9
2.1 Introduction	10
2.2 Materials and Methods	12
2.2.1 Test Material	12
2.2.2 Test Solution	13
2.2.3 Observation Method	14
2.2.4 Measurement Method	17
2.3Results and Discussion	18

2.3.1 Specimen Observation.....	18
2.3.2 E - pH- Time	29
2.3.3 Polarization Curve	32
2.3.4 Polarization Resistance Curve	35
2.4 Ant-Nest Corrosion Mechanism on Copper tube	39
2.4.1 The Comproportionation and Disproportionation Reaction in the Corrosion Mechanism	39
2.4.2. Polarization Curve and Polarization Resistance Curve Analysis	42
2.4.3. The Relationship between $h(i)$ and $E(i)$ Curve	44
2.5 Conclusion	47
Reference	47

**Chapter 3 Estimation of Exchange Current Density on
Copper Electrode by Using Differential Polarization Method ...49**

3.1 Introduction	50
3.2 Experimental Method	52
3.2.1 Specimens	52
3.2.2 Test Solution	52
3.2.3 Experimental Measurement	53
3.3 Results	54
3.3.1 E_{ocp} , pH-Time	54
3.3.2 Polarization Curve Result	55
3.3.3 Polarization Resistance Result	57
3.4 Discussion	59

3.4.1 Reaction on Copper Electrode	59
3.4.2 Proposed the Differential Polarization Method	61
3.4.3 Estimation of i_0 on Copper electrode by using TEM	65
3.4.4 Estimation of i_0 on Copper electrode by using DPM	67
3.5 Conclusion	74
Reference	75

Chapter 4 Performance, Rate of Heat Release, and Combustion

Stability of Dual-fuel Mode in a Small Diesel Engine	78
4.1 Introduction	79
4.2 Materials and Methods	82
4.2.1 Simulated biogas and biodiesel properties	82
4.2.2 Test System	84
4.2.3 Analysis procedure	87
4.3 Results and Discussion	89
4.3.1 Performance of dual fuel (biodiesel-simulated biogas)	89
4.3.1.1 Brake Thermal Efficiency	89
4.3.1.2 Biodiesel replacement and biogas energy ratio	92
4.3.1.3 Specific fuel consumption	94
4.3.1.4 Exhaust gas temperature	96
4.3.1.5 Analysis of methane composition of fuel setup	97
4.3.2 Combustion pressure and rate of heat release of dual fuel (biodiesel-simulated biogas)	99
4.3.3 Combustion stability	104

4.4 Conclusions106

Reference108

Chapter 5 Summary114

Appendix I *E*-pH diagram117

Acknowledgements.....xviii

List of Tables

1.1 Properties of Copper	2
2.1 Typical and standard of copper tube	10
2.2 Thermodynamic data (1 atm, 298 K)	30
4.1 Composition of Biodiesel from many sources	82
4.2 Specification of methane and carbon dioxide	83
4.3 Biodiesel Composition	84
4.4 Engine specification	86

List of Figures

1.1	Application of copper tube in air conditioning	3
2.1	The specimen copper deoxidized phosphor tube	13
2.2	State of immersion in experiment	15
2.3	Embedded Sample in the epoxy resin for the cross-section observation ...	15
2.4	Microscope Lasertec Optelics Hybrid	16
2.5	Polis IMT-P2	16
2.6	Microscope BX51M	17
2.7	Electrochemical measurement	18
2.8	The cross-section observations result of copper tube in 100 ppm HCHO + 1000 ppm Cu(HCOO) ₂ solution	21
2.9	The cross-section observations result of copper tube in 1000 ppm Cu(HCOO) ₂ solution	22
2.10	The cross-section observations result of copper tube in 1000 ppm Cu(HCOO) ₂ added HCOOH to pH=3 solution.....	23
2.11	The surface observations result of copper tube in 100 ppm HCHO + 1000 ppm Cu(HCOO) ₂ solution	24
2.12	The surface observations result of copper tube in 1000 ppm Cu(HCOO) ₂ solution	25
2.13	The surface observations result of copper tube in 1000 ppm Cu(HCOO) ₂ added HCOOH to pH=3 solution	26
2.14	(a) Surface observations and (b) SEM observation of Cu tube specimen immersed in 1000 ppm Cu(HCOO) ₂ after 10 days immersion.....	27

2.15	The result of SEM and EPMA image of the copper tube after being Immersed (a) 15 days and (b) 30 days in 1000 ppm Cu(HCOO) ₂ led to corresponding elements of copper, oxygen, and phosphorus.	28
2.16	E_{corr} and pH measurement result of copper tube in 3 solutions condition ...	31
2.17	E -pH Diagram of Cu and Cu(HCOO) ₂ with the assumption that the Concentration of total dissolved copper ions [Cu ⁺⁺] was 10 ⁻³ mol kg ⁻¹	31
2.18	The polarization curve result of copper tube at 0 day in (a) 100 ppm HCHO+ 1000 ppm Cu(HCOO) ₂ solution, (b) 1000 ppm Cu(HCOO) ₂ solution and (c) 1000 ppm Cu(HCOO) ₂ added HCOOH to pH=3 solution	33
2.19	The polarization curve result of copper tube at 20 days in (a) 100 ppm HCHO+ 1000 ppm Cu(HCOO) ₂ solution, (b) 1000 ppm Cu(HCOO) ₂ solution and (c) 1000 ppm Cu(HCOO) ₂ added HCOOH to pH=3 solution	35
2.20	The polarization resistance curve result of copper tube at 0 day in (a) 100 ppm HCHO+ 1000 ppm Cu(HCOO) ₂ solution, (b) 1000 ppm Cu(HCOO) ₂ solution and (c) 1000 ppm Cu(HCOO) ₂ added HCOOH to pH=3 solution	37
2.21	The polarization resistance curve result of copper tube at 20 days in (a) 100 ppm HCHO+ 1000 ppm Cu(HCOO) ₂ solution, (b) 1000 ppm Cu(HCOO) ₂ solution and (c) 1000 ppm Cu(HCOO) ₂ added HCOOH to pH=3 solution	39
2.22	The experimental polarization curve (Black Line) and theoretical	

	polarization curve (Gray dot line) of the copper tube immersed in	
	(a) 100 ppm HCHO+ 1000 ppm Cu(HCOO) ₂ solution and (b) copper	
	tube immersed in 1000 ppm Cu(HCOO) ₂ solution46
3.1	(a) Copper as working electrode and (b) platinum as a counter electrode	..52
3.2	Measurement method54
3.3	<i>E</i> _{ocp} , pH-Time curve of the copper electrode in 0.5 mol dm ⁻³ H ₂ SO ₄	
	Solution55
3.4	Polarization curve of the copper electrode in 0.5 mol dm ⁻³ H ₂ SO ₄	
	solution, deaerated with H ₂ gas bubbling, stirring, in room temperature	
	and only in cathode and anode condition (1 Cycle)56
3.5	Polarization curve of the copper electrode in 0.5 mol dm ⁻³ H ₂ SO ₄	
	solution, deaerated with H ₂ gas bubbling, stirring, in room temperature	
	in 5 Cycle57
3.6	Polarization resistance curve of the copper electrode in 0.5 mol dm ⁻³ H ₂ SO ₄	
	solution, deaerated with H ₂ gas bubbling, stirring, in room temperature	
	and only in cathode and anode condition (1 Cycle)58
3.7	Polarization curve of the copper electrode in 0.5 mol dm ⁻³ H ₂ SO ₄	
	solution, deaerated with H ₂ gas bubbling, stirring, in room temperature	
	and only in 5 Cycle59
3.8	<i>E</i> -pH equilibrium diagram for the system copper-water at 25°C, that	
	considering to Cu, Cu ₂ O and CuO and unconsidering to Cu(OH) ₂61
3.9	The TEM area for <i>i</i> ₀ estimation of Figure 3.466
3.10	The TEM area for <i>i</i> ₀ estimation of Figure 3.566
3.11	Polarization resistance data (Original curve) plots (light blue circle) and	

its revised plot $\{h_{\text{exp}}(i)-0.004\}$ (dark blue). A green vertical lines ($ i =0.2 \text{ mAcm}^{-2}$ and 2 mAcm^{-2}) are added which satisfied the tafel slope And the purple dashed line is added as the tafel slope.	70
3.12 Polarization resistance data (Original curve) plots (light color circle) and its revised plot $\{h_{\text{exp}}(i)-0.003\}$ (dark color). A green vertical lines ($ i =0.3 \text{ mAcm}^{-2}$ and 3 mAcm^{-2}) are added which satisfied the tafel slope And the purple dashed line is added as the tafel slope.	71
3.13 The result of α_c (red line) and i_0 (blue line) in range of estimated area for 1 cycle measurement ($ i =0.2 \text{ mAcm}^{-2}$ and 2 mAcm^{-2})	73
3.14 The result of α_c (red line) and i_0 (blue line) in range of estimated area for 5 cycles measurement ($0.3 \text{ mAcm}^{-2} \leq i \leq 3 \text{ mAcm}^{-2}$)	74
4.1 Experimental Set up	85
4.2 Brake thermal efficiency in variation applied torque at (a) 1800 rpm, (b) 2000 rpm, (c) 2200 rpm, (d) 2400 rpm, and (e) 2600 rpm	91
4.3 Biodiesel replacement in variation applied torque at (a) 1800 rpm, (b) 2000 rpm, (c) 2200 rpm, (d) 2400 rpm, and (e) 2600 rpm	93
4.4 Biogas Energy ratio in variation applied torque at (a) 1800 rpm, (b) 2000 rpm, (c) 2200 rpm, (d) 2400 rpm, and (e) 2600 rpm	94
4.5 Specific fuel consumption in variation applied torque at (a) 1800 rpm, (b) 2000 rpm, (c) 2200 rpm, (d) 2400 rpm, and (e) 2600 rpm.....	95
4.6 Exhaust gas temperature in variation applied torque at (a) 1800 rpm, (b) 2000 rpm, (c) 2200 rpm, (d) 2400 rpm, and (e) 2600 rpm	97
4.7 Brake thermal efficiency vs. biogas energy ratio in (a) 3.5 Nm (b) 10.5 Nm (c) 17.6 Nm and (d) 24.6 Nm.	98

4.8	Pressure in cylinder and ROHR vs. crankshaft angle position of the engine with speed 1800 rpm at (a) 3.5 Nm (b) 10.5 Nm (c)17.6 Nm and (d) 24.6 Nm	101
4.9	Pressure in cylinder and ROHR vs. crankshaft angle position of the engine with speed 2000 rpm at (a) 3.5 Nm (b) 10.5 Nm (c)17.6 Nm and (d) 24.6 Nm	101
4.10	Pressure in cylinder and ROHR vs. crankshaft angle position of the engine with speed 2200 rpm at (a) 3.5 Nm (b) 10.5 Nm (c)17.6 Nm and (d) 24.6 Nm	102
4.11	Pressure in cylinder and ROHR vs. crankshaft angle position of the engine with speed 2400 rpm at (a) 3.5 Nm (b) 10.5 Nm (c)17.6 Nm and (d) 24.6 Nm	102
4.12	Pressure in cylinder and ROHR vs. crankshaft angle position of the engine with speed 2600 rpm at (a) 3.5 Nm (b) 10.5 Nm (c)17.6 Nm and (d) 24.6 Nm	103
4.13	COV_{imep} vs. torque in 2400 rpm	105
4.14	COV_{imep} vs. Biogas fuel ratio in 2400 rpm	106

Abbreviations

i is the net current density ($i = i_a + i_c$) (mA cm^{-2})

δ is the Nernst diffusion layer thickness (cm)

$i_{\text{Cu}(\text{HCOO})_2}$ is the limiting diffusion current density of $\text{Cu}(\text{HCOO})_2$ (mA cm^{-2})

$[\text{Cu}(\text{HCOO})_2]_{\text{bulk}}$ is the activity of $\text{Cu}(\text{HCOO})_2$ in the bulk solution (-)

$k_{\text{Cu}(\text{HCOO})_2, \text{L}}$ is the limiting diffusion rate constant of $\text{Cu}(\text{HCOO})_2$ (cm s^{-1})

$D_{\text{Cu}(\text{HCOO})_2}$ is the limiting diffusion coefficient of the $\text{Cu}(\text{HCOO})_2$ ($\text{cm}^2 \text{s}^{-1}$)

E_{eq} is the equilibrium electrode potential (V vs. SHE).

E^0 is the standard electrode potential (V vs. SHE).

E^ϕ is the formal electrode potential (V vs. SHE).

$\{\text{Red}\}_{\text{bulk}}$ is the activity of the reductant in a bulk solution (-).

$\{\text{Ox}^{z+}\}_{\text{bulk}}$ is the activity of the oxidant in a bulk solution (-).

γ_{Red} is the activity coefficient of the Red (-).

$\gamma_{\text{Ox}^{z+}}$ is the activity coefficient of the Ox^{z+} (-).

$[\text{Red}]_{\text{bulk}}$ is the concentration of the Red in the bulk solution (mol dm^{-3}).

$[\text{Ox}^{z+}]_{\text{bulk}}$ is the concentration of the Ox^{z+} in the bulk solution (mol dm^{-3}).

$[\text{Red}]_{\text{el}}$ is the concentration of the Red near the electrode surface (mol dm^{-3}).

$[\text{Ox}^{z+}]_{\text{el}}$ is the concentration of the Ox^{z+} near the electrode surface (mol dm^{-3}).

z is the number of electrons transferred (-).

F is the Faraday's constant ($F = 96.5 \times 10^3 \text{ A s mol}^{-1}$).

R is the gas constant ($R = 8.31 \text{ J mol}^{-1} \text{ K}^{-1}$).

T is the absolute temperature (K).

$i(\eta)$ is the net current density as a function of the overvoltage (mA cm^{-2}).

η is the overvoltage between an applied potential E , and the E_{eq} ($\eta = E - E_{\text{eq}}$) (V).

η^ϕ is the overvoltage according to the standard E^ϕ ($\eta^\phi = E - E^\phi$) (V).

i_0 is the exchange current density (mA cm^{-2}).

$$f_a = \frac{\alpha_a nF}{RT} \quad (\text{V}^{-1})$$

$$f_c = \frac{-\alpha_c nF}{RT} \quad (\text{V}^{-1})$$

$i_{\text{Red,L}}$ is the limiting diffusion current density of the Red, (mA cm^{-2}).

$i_{\text{Ox}^{z+},\text{L}}$ is the limiting diffusion current density of the Ox^{z+} , (mA cm^{-2}).

The relations and details are shown as follows:

$$\left. \begin{aligned} i_{\text{Red,L}} &= zF \frac{D_{\text{Red}}}{\delta_{\text{Red}}} [\text{Red}]_{\text{bulk}} = zF k_{\text{Red}} [\text{Red}]_{\text{bulk}} \\ i_{\text{Ox}^{z+},\text{L}} &= -zF \frac{D_{\text{Ox}^{z+}}}{\delta_{\text{Ox}^{z+}}} [\text{Ox}^{z+}]_{\text{bulk}} = -zF k_{\text{Ox}^{z+}} [\text{Ox}^{z+}]_{\text{bulk}} \end{aligned} \right\}$$

D_{Red} is a diffusion coefficient of the Red ($\text{cm}^2 \text{s}^{-1}$).

$D_{\text{Ox}^{z+}}$ is a diffusion coefficient of the Ox^{z+} ($\text{cm}^2 \text{s}^{-1}$).

δ_{Red} is the Nernst diffusion layer thickness for the Red (cm).

$\delta_{\text{Ox}^{z+}}$ is the Nernst diffusion layer thickness for the Ox^{z+} (cm).

k_{Red} is the rate constant of the Red (cm s^{-1}).

$k_{\text{Ox}^{z+}}$ is the rate constant of the Ox^{z+} (cm s^{-1}).

i_a is the anodic branch current density (mA cm^{-2}).

i_c is the cathodic branch current density (mA cm^{-2}).

$h_a(i_a)$ is the anodic branch polarization resistance ($\text{k}\Omega \text{ cm}^2$).

$h_c(i_c)$ is the cathodic branch polarization resistance ($\text{k}\Omega \text{ cm}^2$).

$h(j)$ is the polarization resistance ($\text{k}\Omega \text{ cm}^2$).

l_c/κ_c is the polarization resistance due to the oxide film ($\text{k}\Omega \text{ cm}^2$).

l_s/κ_s is the polarization resistance due to the solution resistance ($\text{k}\Omega \text{ cm}^2$).

l_c is the thickness of the oxide film (cm).

l_s is the distance between the anodic and the cathodic site (cm).

κ_c is the conductivity of the oxide film $((k\Omega \text{ cm})^{-1})$.

κ_s is the conductivity of the solution $((k\Omega \text{ cm})^{-1})$.

Chapter 1

Introduction

1.1 Copper Element

Copper is one of the noble metals that was found in the earliest and used around 8000 BCE by Neolithic Man [1]. In the first time, Copper was used almost exclusively since copper has many advantages. Copper was used in many applications by hammered into sheets or another shape. However, due to its softness, Egyptian people in 2000BC improving the fabrication of copper by melting with the gold. Since that, the skill and technology about copper are gradually increasing until now. The applications of copper in our daily life are also increasing by year to year.

Copper has chemical symbol as Cu (from the Latin: Cuprum). Copper is located in group IB in table periodic with atomic number 29. Copper color is peculiar red color, pinkish-orange color, in the pure condition [3]. Copper properties is mentioned in Table 1.1.

Table 1 Properties of Copper [3]

Atomic radius of Copper	1.28 Å
Ionic radius of Copper	0.96 Å
Occurrence of copper in the earth's crust	0.01 %
Atomic weight	63.57
Melting point, °C	1083
Boiling point, °C	2360
Specific gravity at 20 °C	8.89
Specific gravity at 1083 °C	8.22
Specific gravity at 1100 °C	7.96
Specific gravity at 1200 °C	7.81
Specific heat at 17 °C, cal/g	0.0911

Latent heat of fusion, cal/g	43.3
Electric resistivity of a copper wire 1m long and 1mm ² In cross section at 20 °C, ohm	0.017241
Normal potential	0.34

1.2 Motivation of the Study

Global warming is giving the great impact to air conditioning and refrigerator application in our daily life [4]. However, increasing application of air conditioning and refrigerator are also increasing the application of copper tube. Copper has advantages on its thermal conductivity. Therefore, copper is commonly used in air conditioner and refrigerator [5-6]. Figure 1.1 shows the application of copper tube in air conditioning.

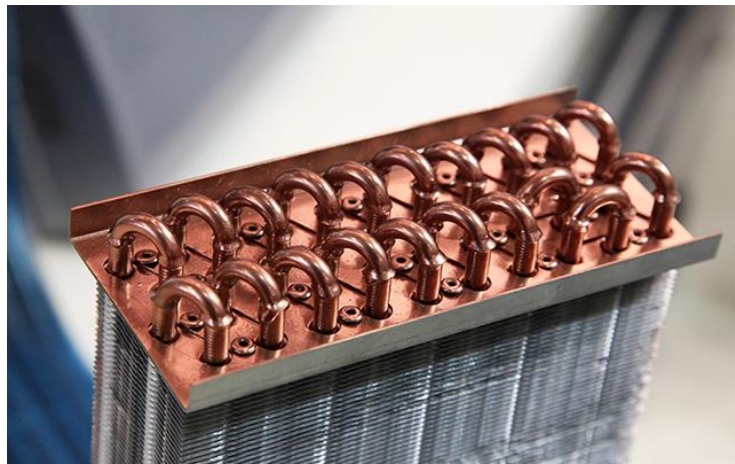


Figure 1.1 Application of copper tube in air conditioning.

(Source:<https://copperindia.org/air-conditioners/>)

Copper tube has many failure problems in its application. Ant-nest corrosion is one of the most serious problems that occur in the application of copper tube in the air conditioning [7-11]. Ant nest corrosion is a typical of local corrosion leakage that has form like ant nest that can contribute to decrease the performance of air conditioner.

However, solving this issue can contribute to the energy use that can influence the global warming [12]. Due to increasing number of application of air conditioner as the effect of global warming, the ant-nest corrosion issue is important to be solved to keep the efficiency of the air conditioner. Therefore, the mechanism of ANC is important to be solved. This issue is one of motivations in conducting this research.

In the other application, Copper is also considered in applications on electrode in the hydrogen evolution reaction. As well known, renewable alternative energy attract interest of many researchers around the world to replace the consumption of fossil fuel in our daily life. As one of promising energy, hydrogen fuel is famous known with some advantages such as: sustainable, cost effectiveness, high efficiency, and zero emission [13-14]. One of many methods to produce hydrogen is water electrolysis. Many researchers have been conducted some researches to investigate the hydrogen evolution reaction to find lower cost production, higher efficiency, and the stability of catalyst [15-18]. Copper electrode is one of electrode that used in the hydrogen evolution reaction. The hydrogen evolution reaction using copper electrode or its complex much less have been investigated by many researchers [19-22]. To evaluate the catalyst performance of electrode in hydrogen evolution reaction, the exchange current density (i_0) is commonly used in the application. One proposed method that called differential polarization method is introduced to calculate the exchange current density (i_0) in the hydrogen evolution reaction on copper electrode. This differential polarization method is a promising method in the calculation of current density (i_0) since the commonly used method that called Tafel extrapolation method is often to find inaccurate and unreliable calculation. This second issue is another motivation in conducting this research.

Since copper also used on engine composition, a research about diesel engine are

conducted. However, the research about diesel engine were focused on dual fuel mode. As well known, biodiesel and biogas are the promising alternative energy source for diesel engine due to the resource availability, un Hazardous environment, economically, and engine efficiency. Therefore, research about performance, rate of heat release and combustion stability of dual-fuel mode in a small diesel engine are discussed in this dissertation.

1.3 Scope of the Research

1.3.1 Scope of the Study on Ant-Nest Corrosion on Copper Tube

The mechanism of Ant-Nest corrosion in this research is conducted in Copper Formate solution, Formaldehyde solution and Formic acid solution. However, the attention be conducted more in the condition of Copper Formate solution. These solutions were chosen as test solution because: (A) Copper reacts with formic acid to form copper formate and formaldehyde as a corrosion product. Therefore, the pitting cavities will be occupied with the copper formate solution and formaldehyde solution. (B) The replacement of the pit solution to the bulk solution is complicated due to the narrow pitting mouth of the ant nest corrosion. Therefore, the copper formate solution probably abides in the pitting cavities and (C) The comproportionation reaction between a copper formate and metallic copper is indispensable for the explanation of the ant nest corrosion that will be discussed in chapter 2.

1.3.2 Scope of the Study of Exchange Current Density on Copper Electrode

The estimation of exchange current density on copper electrode examine the proposed DPM technique in the copper electrode from two points: (A) how to sight the tafel slope region accurately and (B) how to remove the physical resistance of the copper electrode that can be dissolved in acid solution like in H_2SO_4 solution.

1.3.3 Scope of the Study of Dual-fuel Mode in a Small Diesel Engine

Fossil fuel have been used in many several years for engine at industries and automobiles. The large increasing number of industries and automobiles make the consumption of fossil fuel increasing in this recent years. Biodiesel and biofuel are the promising alternative energy source for diesel engine due to the resource availability, unhazardous environment, economically, and engine efficiency. In rural area, farm field, the dual-fuel mode diesel engine is seem to be potential applied on-farm energy utilization. This research is focused in the study of CI engine run in dual-fuel mode without dominant modification. The objectives of this study are to examine the performance and combustion of the small diesel engine run in dual-fuel mode. In this paper, the phenomena of the thermal brake efficiency also be discussed. The results be used as recommendation for the future operation of the engine.

Reference

1. Ellis O.W. Copper and Copper alloys, American society of metal, Cleveland-Ohio, 1948.
2. Carl Schnabel, Handbook of Metalurgy, third edition, Vol. 1, Macmillan and Co., 1921. Page 1-25.
3. A. A. Tseidler, Metallurgy of Copper and Nickel, Israel program for scientific Translation, Jerusalem 1964, page 5.
4. Lundgren, K.; Kjellstrom, T. Sustainability challenges from climate change and air conditioning use in urban areas. Sustainability 2013, 5, 3116–3128.
5. Bastidas, D.M.; Cayuela, I.; Bastidas, J.M. Ant-nest corrosion of copper tubing in air-conditioning units. Rev. Metal. 2006, 42, 367–381.
6. Cano, E.; Polo, J.L.; López-Caballero, A.; Bastidas, J.M. Copper corrosion in air-

- conditioning systems. *Corros. Prev. Control* 2005, 52, 56–58
7. Elliott, P.; Corbett, R.A. CORROSION/99; Paper Number 99342; NACE International: Houston, TX, USA, 1999.
 8. Corbett, R.A.; Elliott, P. CORROSION/2000; Paper Number 00646; NACE International: Houston, TX, USA, 2000.
 9. Chandra, K.; Kain, V.; Shetty, P.S.; Kishan, R. Failure analysis of copper tube used in a refrigerating plant. *Eng. Fail. Anal.* 2014, 37, 1–11.
 10. Zhou, J.; Yan, L.; Tang, J.; Sun, Z.; Ma, L. Interactive effect of ant nest corrosion and stress corrosion on the failure of copper tubes. *Eng. Fail. Anal.* 2018, 83, 9–16.
 11. Peltola, H.; Lindgren, M. Failure analysis of a copper tube in a finned heat exchanger. *Eng. Fail. Anal.* 2015, 51, 83–97.
 12. Davis, L.W.; Gertler, P.J. Contribution of air conditioning adoption to future energy use under global warming. *Proc. Natl. Acad. Sci. USA* 2015, 112, 5962–5967.
 13. S.E Hosseini, M.A. Wahid, Hydrogen production from renewable and sustainable energy resources: promising green energy carrier for clean development. *Renewable Sustainable Energy Reviews* 57 (2016), pp. 850-866
 14. W. Lubitz, W. Tumas, Hydrogen: An overview. *Chemical Review* 107 (2007), pp. 3900-3903.
 15. N. Pentland, J.O.M. Bockris, E. Sheldon Hydrogen evolution reaction on copper, gold, molybdenum, palladium, rhodium and iron. *J Electrochem Soc*, 104 (1957), pp. 182-194
 16. A. Abbaspour, E. Mirahmadi, Electrocatalytic hydrogen evolution reaction on carbon paste electrode modified with Ni ferrite nanoparticles. *Fuel*, 104 (2013), pp. 575-582

17. Sheng, W.; Gasteiger, H. A.; Shao-Horn, Y. Hydrogen Oxidation and Evolution Reaction Kinetics on Platinum: Acid vs Alkaline Electrolytes. *J. Electrochem. Soc.* 2010, 157, B1529–B1536.
18. Mckone, J. R.; Warren, E. L.; Bierman, M. J.; Boettcher, S. W.; Brunschwig, B. S.; Lewis, N. S.; Gray, H. B. Evaluation of Pt, Ni, and Ni-Mo Electro catalysts for Hydrogen Evolution on Crystalline Si Electrodes. *Energy Environmental Science*, 4 (2011), pp. 3573–3583.
19. Du, J.; Wang, J.; Ji, I.; Xu, X.; Chen, Z. A highly active and robust copper-based electrocatalyst toward hydrogen evolution reaction with low overpotential in neutral solution. *ACS Applied Material & Interfaces*, 8 (2016), pp 30205-30211.
20. Vaduva, C. C.; Naszilcsin, N.; Kellenberger, A.; Medeleanu, M. Catalytic enhancement of hydrogen evolution reaction on copper in the presence of benzylamine. *International Journal of hydrogen Energy* 36 (2011), pp 6994-7001.
21. Raoof, J .B.; Ojani, R.; KIani, A.; Nadimi, S.R. Fabrication of highly porous Pt coated nanostructured Cu-foam modified copper electrode and its enhanced catalytic ability for hydrogen evolution reaction. *International Journal of hydrogen Energy* 35 (2010), pp 452-458.
22. Hosseini, S.R.; Ghasemi, S.; Hasemi, S.A. Effect of surfactants on electrocatalytic performance of copper nanoparticles for hydrogen evolution reaction. *Journal of Molecular Liquids* 222 (2016), pp. 1068-1075.

Chapter 2

Ant-Nest Corrosion Mechanism

2.1. Introduction

Since copper was discovered, the development application of copper is widely used in piping or tube, because copper has many advantages such as strong, light, corrosion resistant and easy for installation. Copper tube is commonly chosen for plumbing, heat exchanger apparatus, air conditioner and other system with ASTM standards 99.9 percent of pure copper in application [1]. The typical and standard of copper tube is shown in table 1. However, the use of copper tube is getting increase due to the global warming effect especially for the application of copper tube in air conditioner. The copper tube in air conditioner has a common failure problem that called ant nest corrosion (ANC). Many research was conducted to solve the ANC but less researchers explained about the mechanism of ANC. Since ANC much less also contribute to the efficiency of the air conditioner which can be effected to the global warming [2], it is important to research about the ANC on copper tube and explain about its behavior and mechanism.

Table 2.1 Typical and standard of copper tube [1]

Tube type	Color code	Standard	Application
Type K	Green	ASTM B 88	- Domestic water service and distribution - Fire protection - Solar - Fuel/fuel oil - HVAC - Snow melting - Compressed air - Natural gas - Liquified petroleum (LP) gas - Vacuum
Type L	Blue	ASTM B 88	- Domestic water service and distribution - Fire protection - Solar - Fuel/fuel oil - Natural gas - Liquified petroleum (LP) gas - HVAC -

			Snow melting - Compressed air - Vacuum
Type M	Red	ASTM B 88	- Domestic water service and distribution - Fire protection - Solar - Fuel/fuel oil - HVAC - Snow melting - Vacuum
DWV	Yellow	ASTM B 306	- Drain, waste, vent - HVAC - Solar
ACR	Blue	ASTM B 280	- Air conditioning - Refrigeration - Natural gas - Liquefied petroleum (LP) gas - Compressed air
OXY,MED	(K)	ASTM	- Medical gas - Compressed medical air -
OXY/MED	Green	B 819	Vacuum
OXY/ACR	(L) Blue		
ACR/MED			

The ANC is the typical of corrosion that also called as formicary corrosion. Edwards et. al reported this formicary corrosion as first report of formicary corrosion in the 1970s [3]. López-Delgado et. al [4] and Cano, E. et. al [5] report that the carboxylic acids such as formic and acetic acid played an important role in mechanism of ANC. Characteristics of the ANC are: (1) the ANC size is about several microns therefore ANC can not be observed by bare eyes inspection. (2) ANC has complicated forms of its corrosion; it looks like a tunnel and has a number of wormholes randomly in the thickness direction of the copper tube; (3) ANC has fast corrosion rate; for example, the corrosion rate of the phosphorus deoxidized copper tube was shown as approximately 10 $\mu\text{m}/\text{day}$ (about 0.3 mA cm^{-2}) [6].

The form of corrosion, branch tunnel, and worm pits attack of the ANC are depended

on the chemical environment of copper tube but the acetic acid atmosphere is less resulted a branch hole of corrosion compared to the formic acid atmosphere. The formic acid atmosphere provokes ANC on the copper tube to be a more perplexing branch hole [7-9]. However, Bastidas et.al. report that formic acid has a lower corrosion rate compared to acetic acid in the vapor experimental conditions [10].

The phosphorus deoxidized copper tube (Cu-PDC) and an oxygen-free copper tube (Cu-OFC) without phosphorus are two kinds of copper tube that commonly used. But, Sakai et. al. [11] report phosphorus in copper is not a crucial factor for the generation of ANC. Some researchers have reported some the mechanism of the ANC [12-16] but the environment conditions in the ANC mechanism were almost in acetic acid and formic acid environment. O. Seri et.al [17] report that copper formate could be formed from reaction of copper and formic acid. Therefore, it is important to conduct a research of ANC using more complex chemical solution such as copper formate solution and observe its behavior on it. In addition, metallic copper and copper formate may be resulted a proportionate reaction which can became a good consideration on explaining the ANC mechanism.

2.2. Material and Methods

2.2.1. Test Material

This ANC mechanism research is conducted using the commercial copper deoxidized phosphor tube (JIS1220, $\varnothing 15 \text{ mm} \times t 0.7 \text{ mm}$, $\text{Cu} \geq 99.90 \text{ mass\%}$, $\text{P}: 0.015 \sim 0.040 \text{ mass\%}$). Figure 2.1 shows the copper tube specimen for the research. Before the test, all copper tubes were rinsed with acetone, then washed with deionized water and then air-dried.



Figure 2.1 The copper deoxidized phosphor tube specimen
(JIS1220, $\varnothing 15 \text{ mm} \times t 0.7 \text{ mm}$, $\text{Cu} \geq 99.90 \text{ mass\%}$, $\text{P}: 0.015 \sim 0.040 \text{ mass\%}$)

2.2.2. Test Solution

Test reagent were copper formate (98 mass% $\text{Cu}(\text{HCOO})_2$, Wako Pure Chemical Ltd.), formaldehyde (36-38 mass % HCOH Wako Pure Chemical Industries, Ltd.), and formic acid (98 mass% HCOOH , Wako Pure Chemical Ltd.). The test solutions were:

1. 100 ppm HCHO + 1000 ppm $\text{Cu}(\text{HCOO})_2$ solution.

The solution pH was 5.5, electric conductivity κ was 90 mS/m, and the dissolved oxygen (DO) was around 5 ppm.

2. 1000 ppm $\text{Cu}(\text{HCOO})_2$ solution

The solution pH was 5.5, electric conductivity κ was 80 mS/m, and the dissolved oxygen (DO) was around 5 ppm.

3. 1000 ppm $\text{Cu}(\text{HCOO})_2$ added HCOOH to pH=3 solution

The solution pH was 3, electric conductivity κ was 86 mS/m, and the dissolved oxygen (DO) was around 5 ppm.

The solution temperature was room temperature (about 298 K).

2.2.3. Observation Method

The Figure 2.2 shows the Copper tube specimen was immersed in 1000 ppm $\text{Cu}(\text{HCOO})_2$ solution. This condition is respectively in all solution conditions. The copper tube was checked in the periods of 0 day, 5 days, 10 days, 15 days, 20 days and 30 days. The immersed copper tube sample was cleaned by ion-exchanged water and air-dried before observed. Microscope Lasertec Optelics Hybrid (Figure 2.3) was occupied for the surface observation. For the cross-section observation, the sample was cut, embedded in the epoxy resin (Figure 2.4) and polished by using the fine polishing machine (Polis IMT-P2) (Figure 2.5) and finally observed by using microscope BX51M-33MB (Figure 2.6). The cross-section observation was carried out whether the ANC occurs or not. The areas of copper tube that attacked by ANC were investigated then with EPMA analyzer (JEOL JXA8900R).

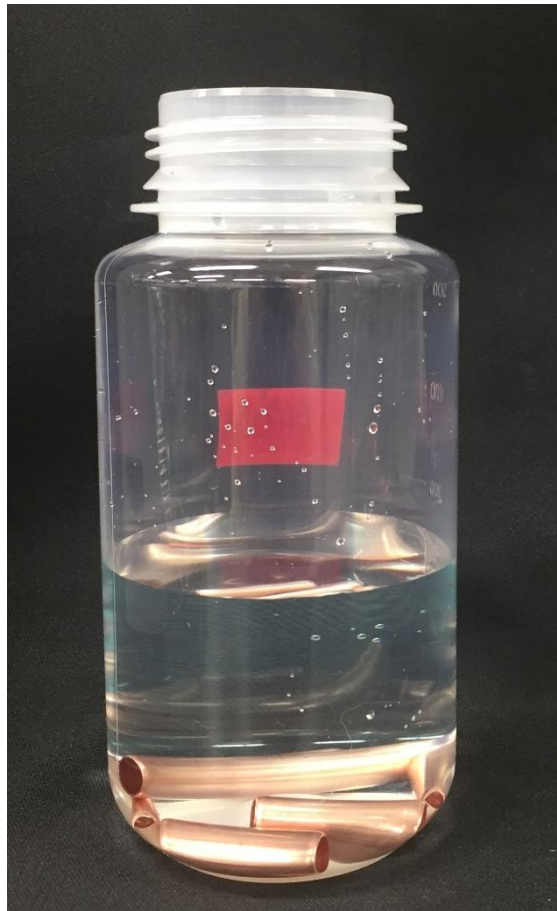


Figure 2.2 State of immersion in experiment

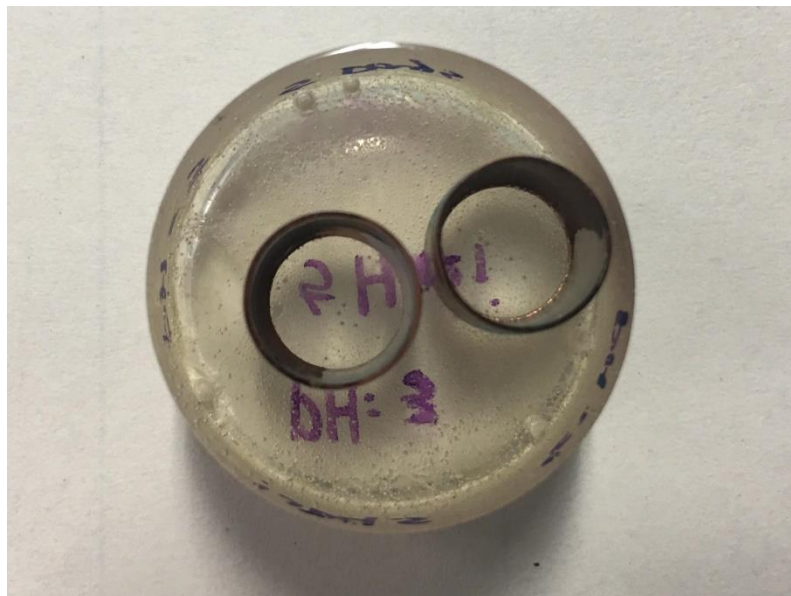


Figure 2.3 Embedded Sample in the epoxy resin for the cross-section observation



Figure 2.4 Microscope Lasertec Optelics Hybrid



Figure 2.5 Polis IMT-P2



Figure 2.6 Microscope BX51M.

2.2.4. Electrochemical Measurement Method

Figure 2.7 shows the electrochemical measurement condition by using an electrochemical measurement system (HZ7000 Hokuto Denko Ltd.) for polarization measurement. The scan rate was 0.1mV/s. The surface of the copper specimen was masked with insulating tape and silicon resin, except for the exposed surface area of 5.6 cm². As a reference electrode, an Ag/AgCl electrode (DKK-TOA Co) in the saturated potassium chloride solution was used and the counter electrode is Pt. In this paper, the electrode potential related to the Ag/AgCl reference electrode (V vs. SSE) was simplified as V unless otherwise noted.

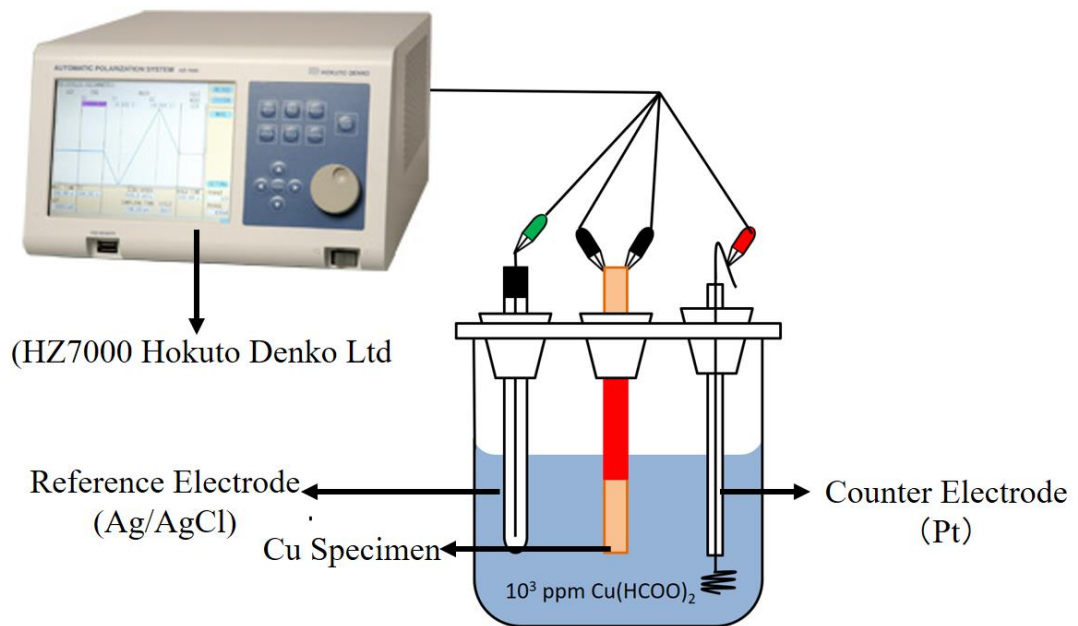


Figure 2.7 Electrochemical measurement

2.3. Results and Discussion

2.3.1. Specimen Observation

Figure 2.8 to Figure 2.10 show respectively the cross section observation result of copper tube in 100 ppm HCHO+ 1000 ppm $\text{Cu}(\text{HCOO})_2$ solution (Figure 2.8), 1000 ppm $\text{Cu}(\text{HCOO})_2$ solution (Figure 2.9) and 1000 ppm $\text{Cu}(\text{HCOO})_2$ added HCOOH to pH=3 solution (Figure 2.10). The cross section observation result of copper tube in 100 ppm HCHO+ 1000 ppm $\text{Cu}(\text{HCOO})_2$ solution in figure 2.8 shows that ANC was started after 15 days immersion time period and at 20 days many ANC occurred in the copper tube. With the almost same result, the cross section observation result of copper tube in 1000 ppm $\text{Cu}(\text{HCOO})_2$ solution in figure 2.9 shows that ANC was started in 15 days immersion time period and after 30 days immersion time period the ANC occurred deep to the center of copper tube. But, the cross section observation result of copper tube in 1000 ppm $\text{Cu}(\text{HCOO})_2$ added HCOOH to pH=3 solution had different results in Figure 2.10. the

corrosion occurred more prominently on the surface of the copper tube in this condition. The condition of Figure 2.8 and Figure 2.9 had more branching tunnel corrosion track than Figure 2.10. However, in all conditions the ANC obviously occurred after being immersed for 20 days. Therefore, the measurement of natural corrosion potential and the polarization curve were done in 20 days.

If the results from Figure 2.8 to Figure 2.10 are compared, it found that the ANC occurred more in the condition on copper tube that immersed in $\text{Cu}(\text{HCOO})_2$ solution. The result of copper tube in 100 ppm HCHO+ 1000 ppm $\text{Cu}(\text{HCOO})_2$ solution also show many ANC result compared to the result of copper tube in 1000 ppm $\text{Cu}(\text{HCOO})_2$ added HCOOH to pH=3 solution. The ANC in 100 ppm HCHO+ 1000 ppm $\text{Cu}(\text{HCOO})_2$ solution and $\text{Cu}(\text{HCOO})_2$ solution were more branching and has same prominent on surface and deep in pitting attack. But the ANC in 1000 ppm $\text{Cu}(\text{HCOO})_2$ added HCOOH to pH=3 solution were more prominent in the surface of copper tube. But in all condition at the late immersion time, the branch of pitting corrosion was random with complex structure tunnels, which means all of the corrosion is typical of the ANC [8,9,16,18]. Therefore, results from Figure 2.8 to Figure 2.10 confirm that the ANC occurred in the phosphorus deoxidized copper tube and show that increasing immersion time increased the number of ANC on the copper tube in 100 ppm HCHO+ 1000 ppm $\text{Cu}(\text{HCOO})_2$ solution, 1000 ppm $\text{Cu}(\text{HCOO})_2$ solution, and 1000 ppm $\text{Cu}(\text{HCOO})_2$ added HCOOH to pH=3 solution.

Figure 2.11 to Figure 2.13 show respectively the surface observation result of copper tube in 100 ppm HCHO+ 1000 ppm $\text{Cu}(\text{HCOO})_2$ solution (Figure 2.11), 1000 ppm $\text{Cu}(\text{HCOO})_2$ solution (Figure 2.12) and 1000 ppm $\text{Cu}(\text{HCOO})_2$ added HCOOH to pH=3 solution (Figure 2.13). The surface colors of the copper tube in the visual observation

were reddish brown, reddish purple, or black as presented in the optical microscope of the surface observation result in Figure 2.11 to Figure 2.13. It took 10 days until all of the surfaces were covered by corrosion. In the early immersion time (0-10 days), the color of copper tube was reddish brown. In the middle of immersion time (15-20 days), the color was reddish purple, and it turn to black color in the end of immersion (30 days). This black color was sign of a step of oxidized copper as reported by Elliot et. al. [12].

The small stain black holes were found on the copper tube surface after being immersed for 10 days. Figure 2.14 (a) shows the small strain black holes in the surface observation of copper tube specimen immersed in 1000 ppm $\text{Cu}(\text{HCOO})_2$ after 10 days immersion. It be assumed that the small strain black hole is the embryo of pitting attack of ANC that had confirmed from the result of cross section observation in Figure 2.8 to Figure 2.10. However, Figure 2.14 (b) show the result of SEM observation due to this condition. Therefore, this typical of corrosion can be classified to local corrosion [13] and also this result shown that the mouth opening for ANC occurred only need a several microns [6].

The observation of the chemical component inside of the hole pitting attack of the ANC was conducted by using the EPMA Analysis and the result is shown in Figure 2.15. the observations were conducted on copper tube that immersed in 1000 ppm $\text{Cu}(\text{COOH})_2$ solution after 15 days (Figure 2.15(a)) and after 30 days (Figure 2.15(b)). The component of copper, oxygen, and phosphorus are focused in this observation. The the presence of phosphorus was at a low level in all areas at both condition. In 15 and 30 days immersion, the presence of copper was high level in all areas and also in the border of the pitting hole. For the oxygen in 15 and 30 days immersion, The presence of oxygen was only detected in the pitting hole of the copper tube and the surface. The interesting point is the presence level of oxygen in 30 days immersion less than the presence level of oxygen in 15 days

immersion. It found that the presence of oxygen in the deep of pitting attack of the ANC was difficult to exist.

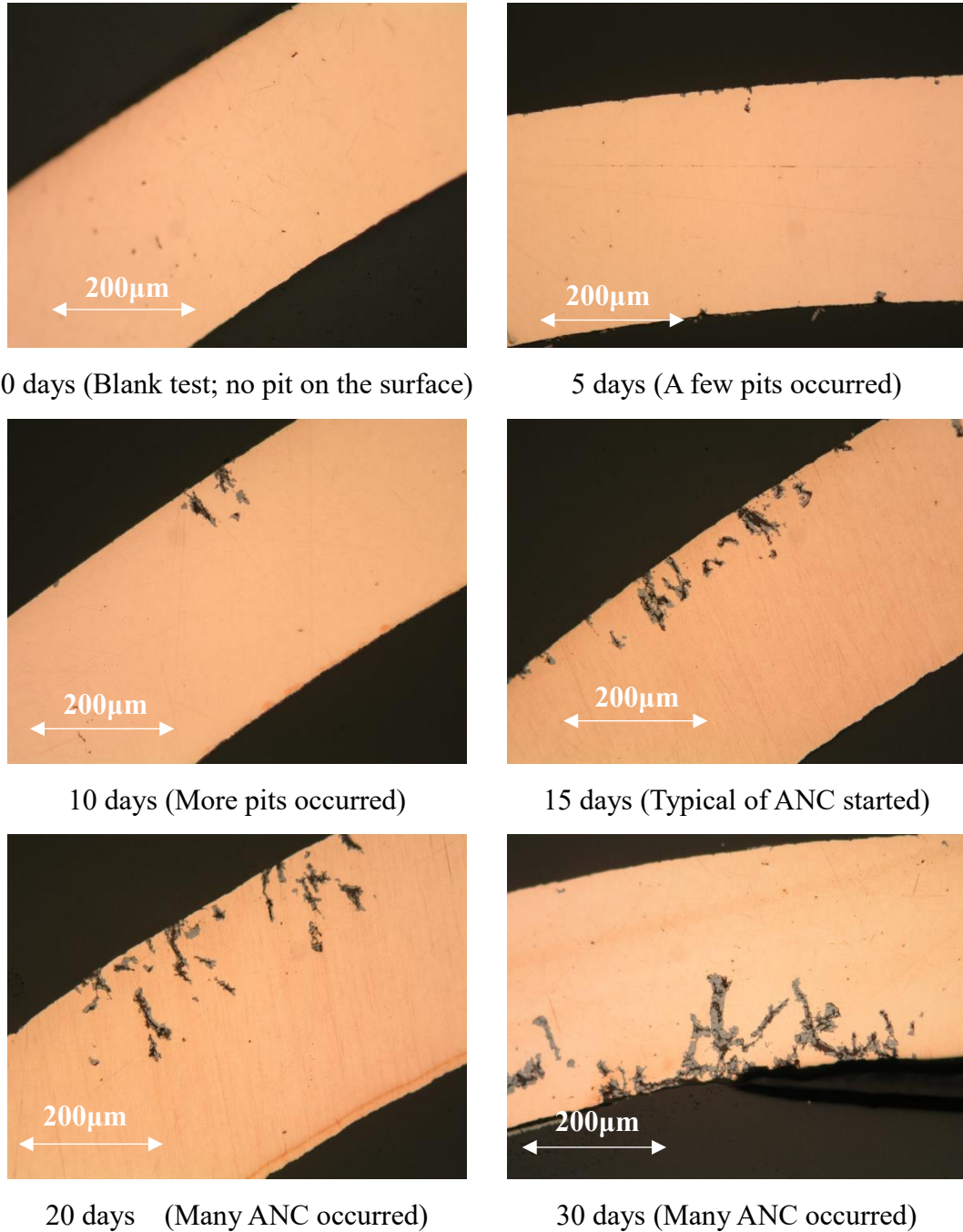
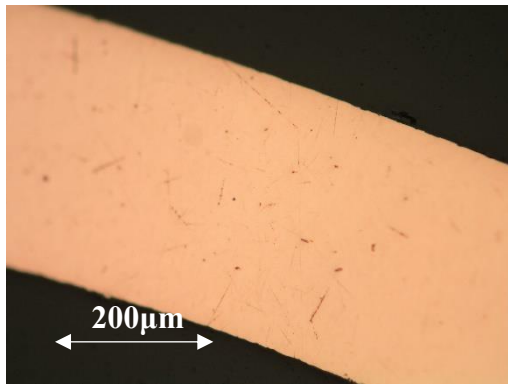
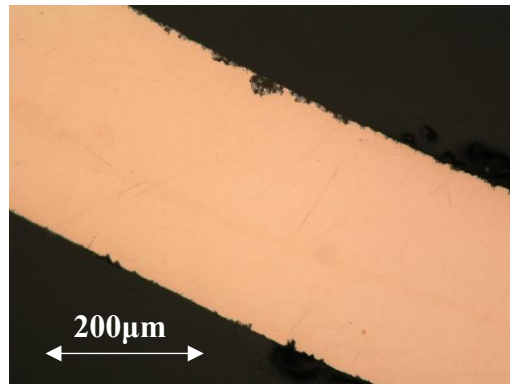


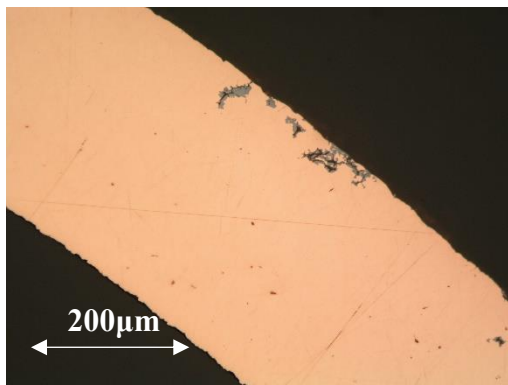
Figure 2.8 The cross-section observations result of copper tube in 100 ppm HCHO+
1000 ppm Cu(HCOO)₂ solution



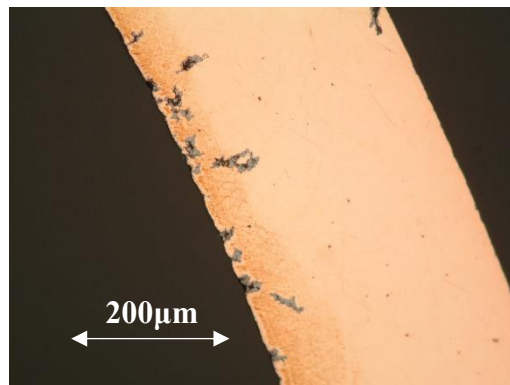
0 days (Blank test; no pit on the surface)



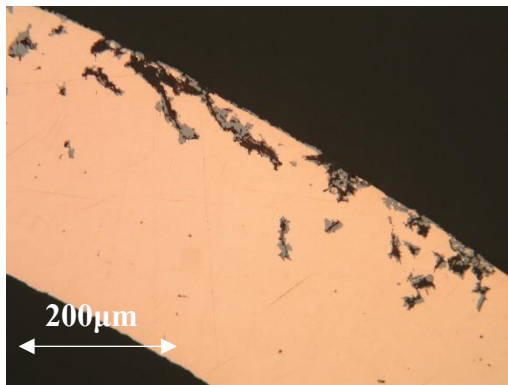
5 days (A few pits occurred)



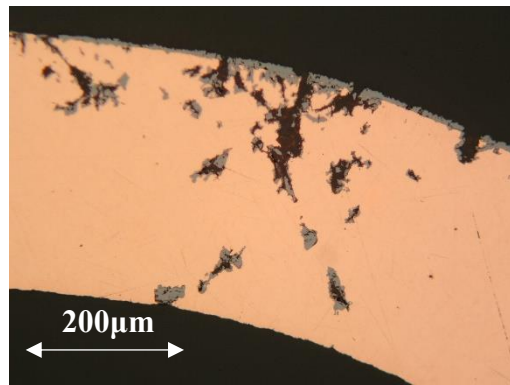
10 days (More pits occurred)



15 days (Typical of ANC started)

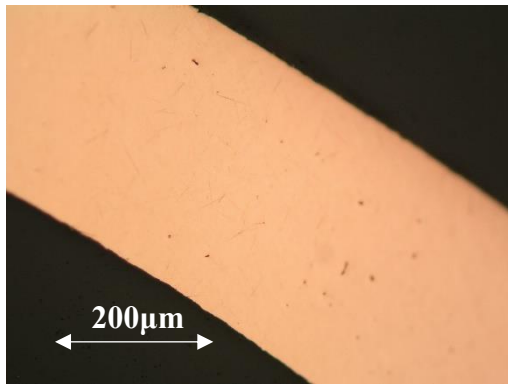


20 days (Many ANC occurred)

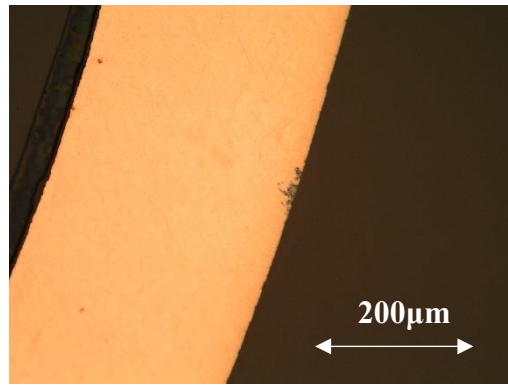


30 days (ANC occurred in center)

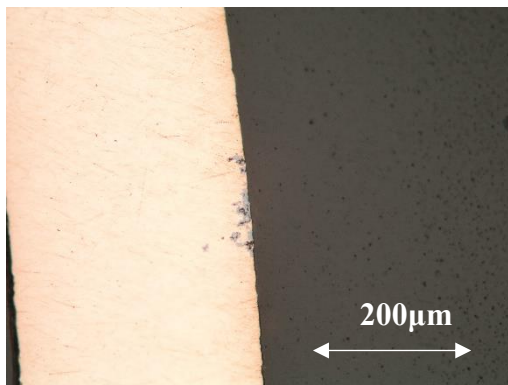
Figure 2.9 The cross-section observations result of copper tube in 1000 ppm $\text{Cu}(\text{HCOO})_2$ solution



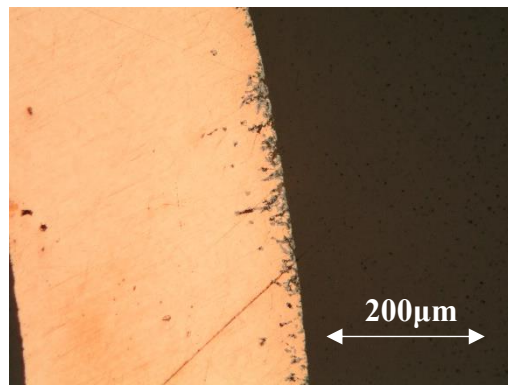
0 days (Blank test; no pit on the surface)



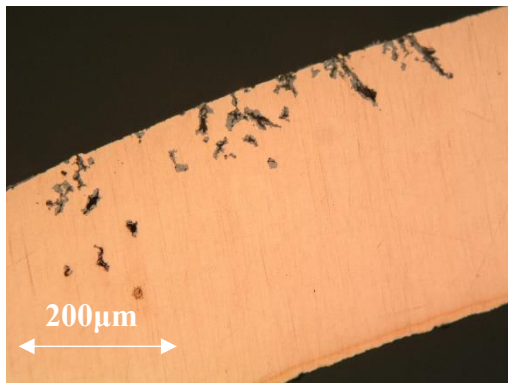
5 days (A few pits occurred)



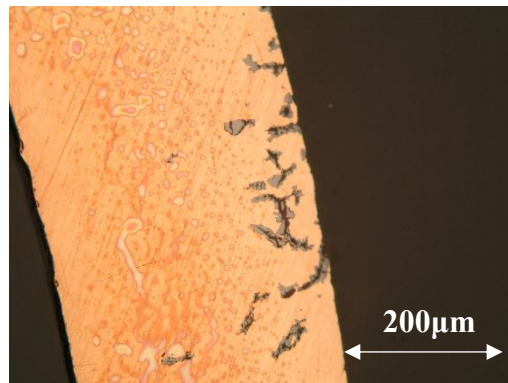
10 days (More pits occurred)



15 days (Typical of ANC started)



20 days (Many ANC occurred)



30 days (ANC occurred in center)

Figure 2.10 The cross-section observations result of copper tube in 1000 ppm $\text{Cu}(\text{HCOO})_2$ added HCOOH to pH=3 solution

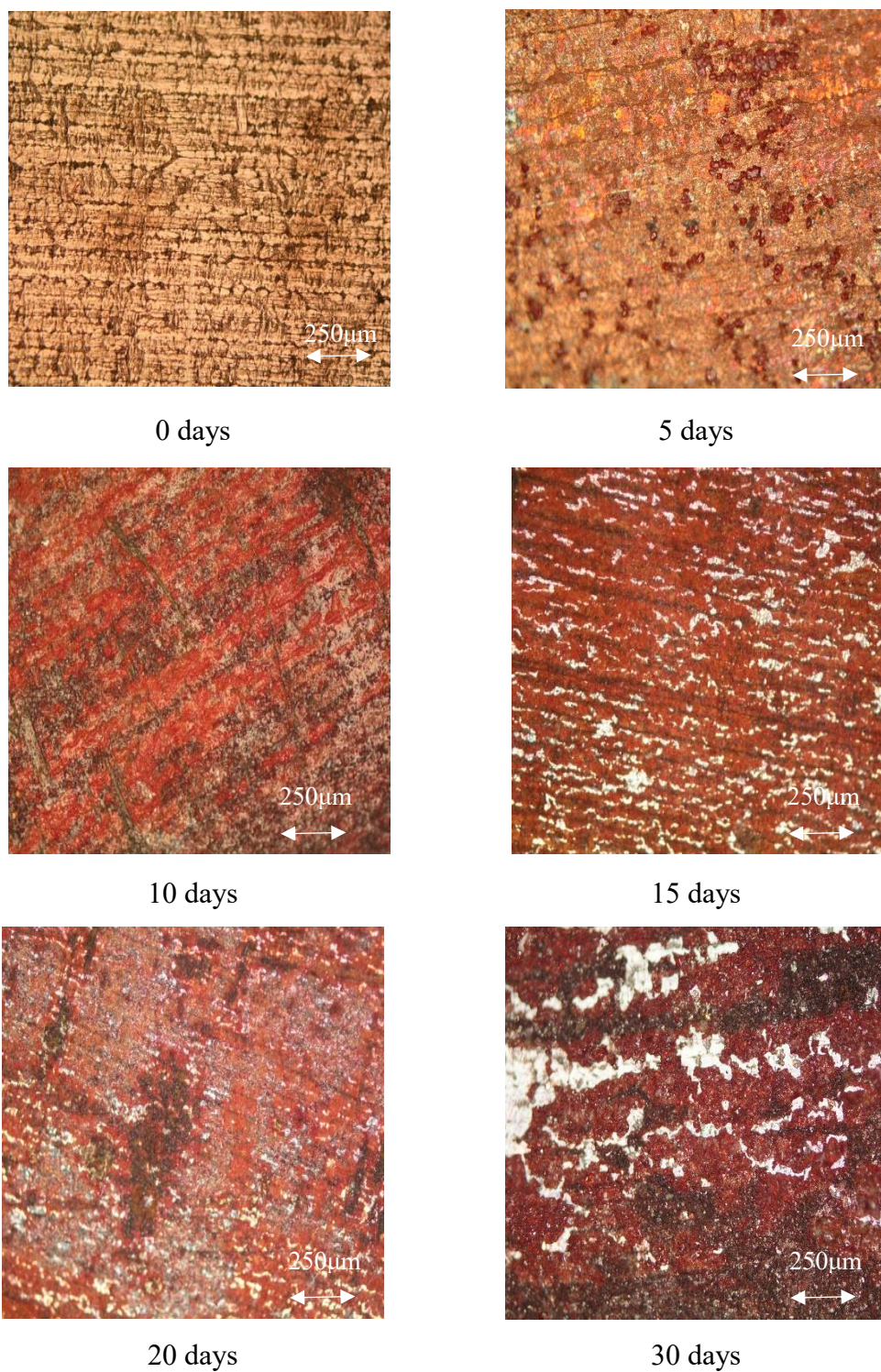
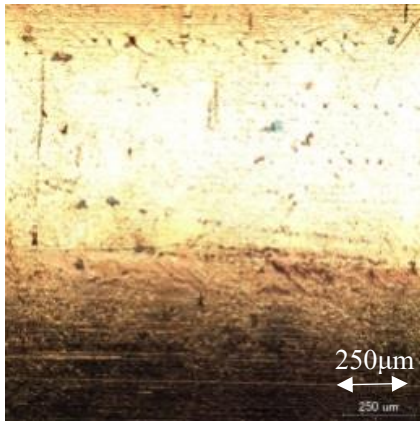
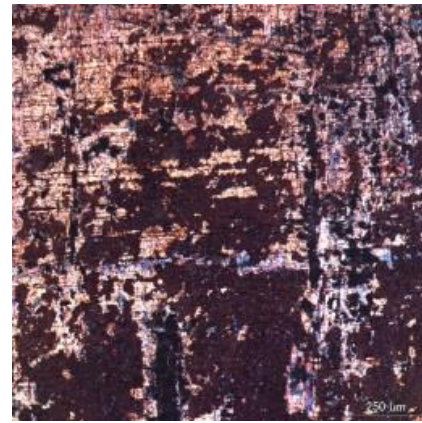


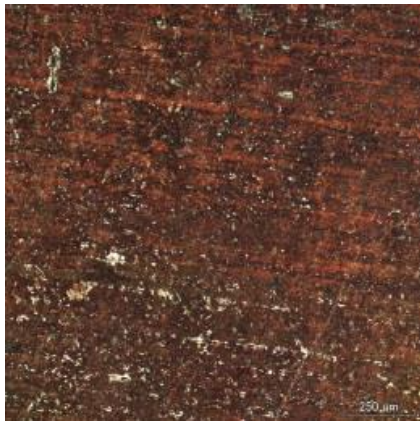
Figure 2.11 The surface observations result of copper tube in 100 ppm HCHO+
1000 ppm $\text{Cu}(\text{HCOO})_2$ solution



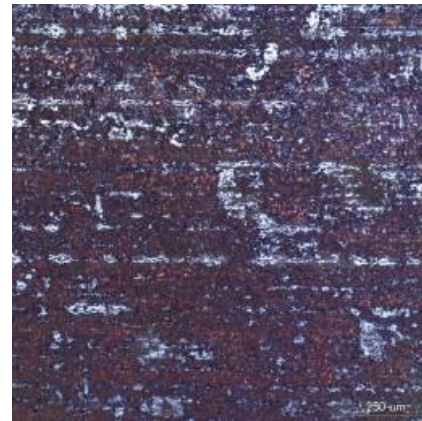
0 days



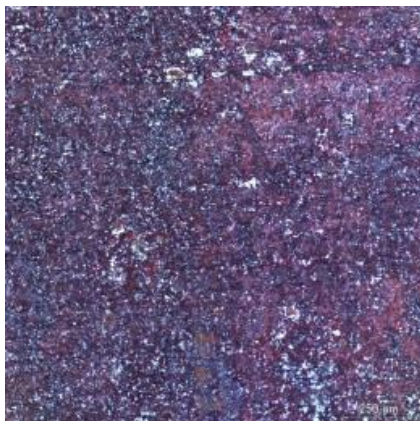
5 days



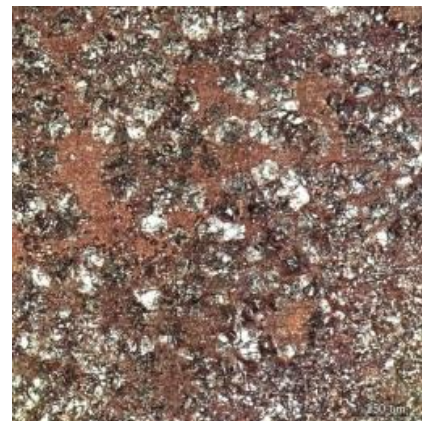
10 days



15 days



20 days

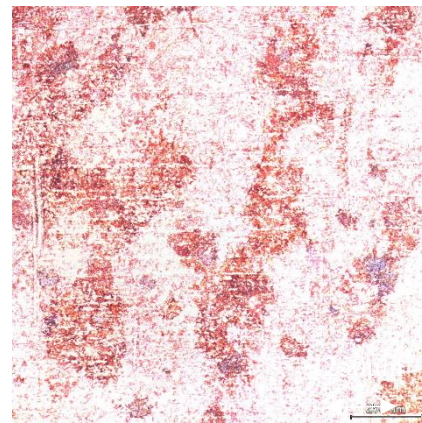


30 days

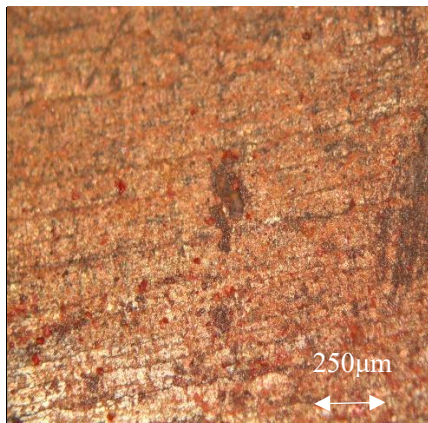
Figure 2.12 The surface observations result of copper tube in 1000 ppm $\text{Cu}(\text{HCOO})_2$ solution



0 days



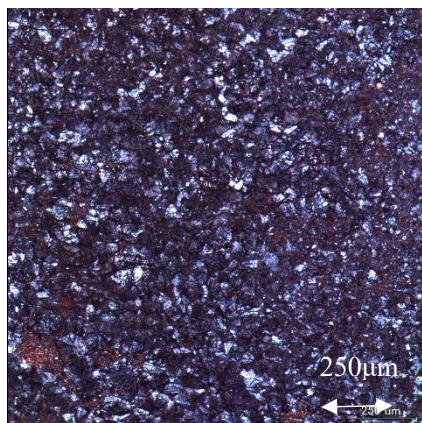
5 days



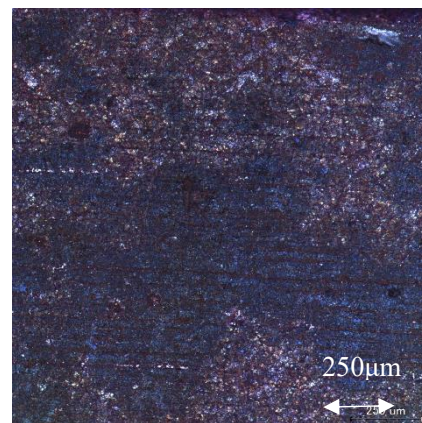
10 days



15 days

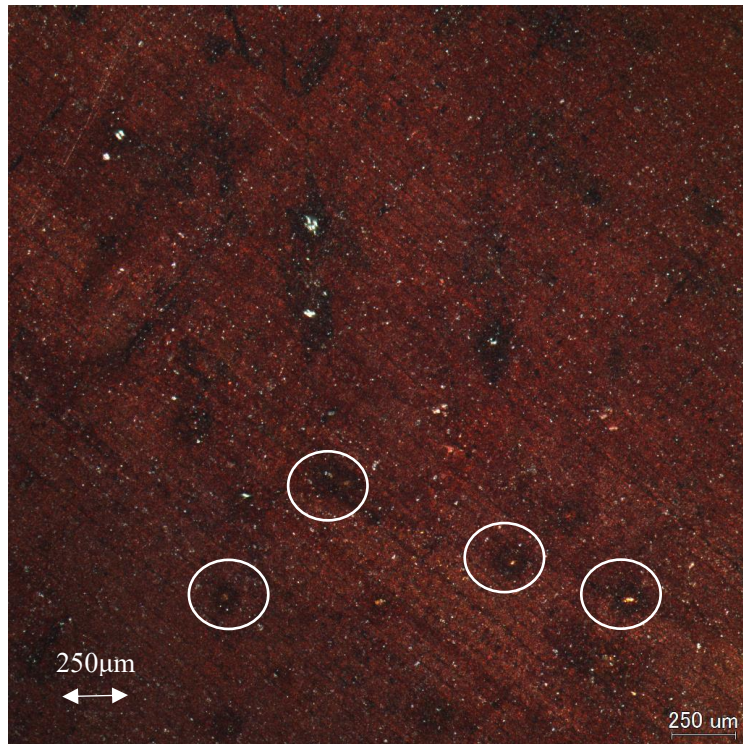


20 days

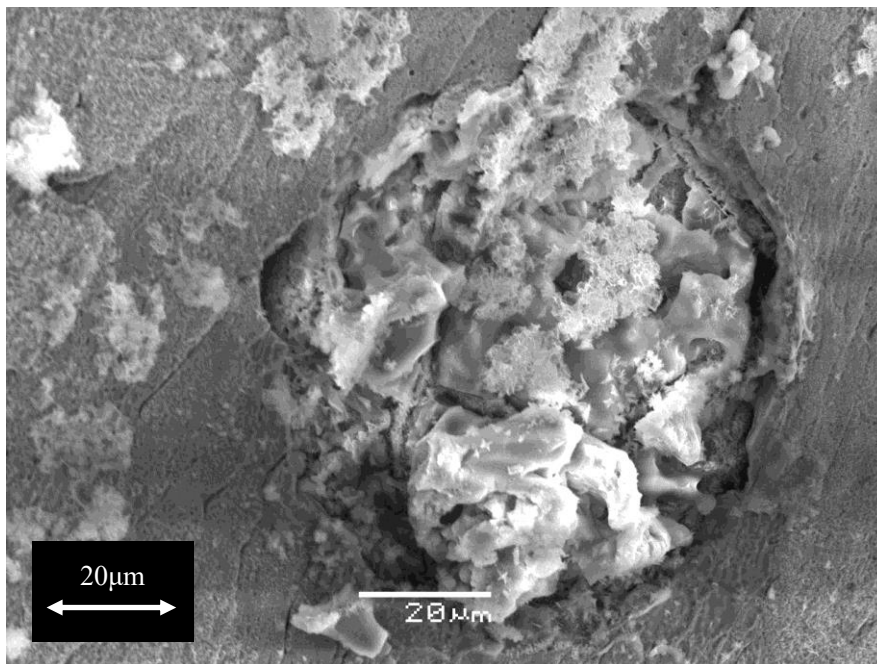


30 days

Figure 2.13 The surface observations result of copper tube in 1000 ppm $\text{Cu}(\text{HCOO})_2$ added HCOOH to $\text{pH}=3$ solution

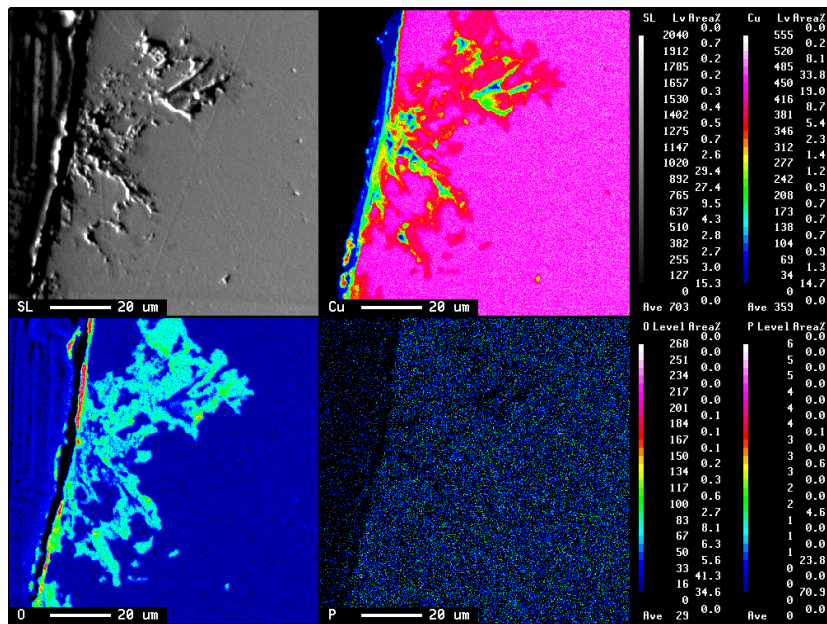


(a)

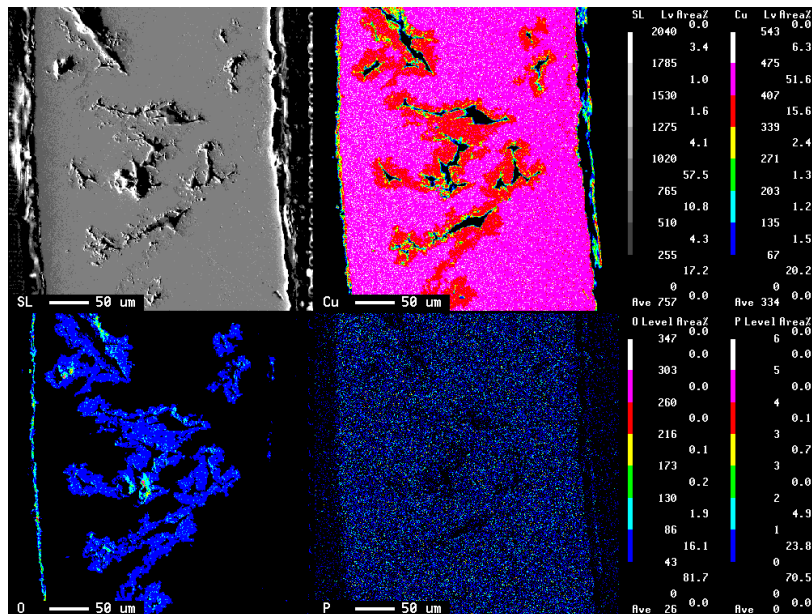


(b)

Figure 2.14 (a) Surface observations and (b) SEM observation of Cu tube specimen immersed in 1000 ppm $\text{Cu}(\text{HCOO})_2$ after 10 days immersion.



(a)



(b)

Figure 2.15 The result of SEM and EPMA image of the copper tube after being immersed (a) 15 days and (b) 30 days in 1000 ppm $\text{Cu}(\text{HCOO})_2$ led to corresponding elements of copper, oxygen, and phosphorus.

(Situmorang, R.S.; Kawai, H. Investigating the Mechanism behind ‘Ant Nest’ Corrosion on Copper Tube. *Materials* **2018**, *11*, 533.)

2.3.2. E_{corr} -pH-Time

The 20 days E_{corr} and pH measurement result of copper tube in 100 ppm HCHO+ 1000 ppm $\text{Cu}(\text{HCOO})_2$ solution, 1000 ppm $\text{Cu}(\text{HCOO})_2$ solution, and 1000 ppm $\text{Cu}(\text{HCOO})_2$ added HCOOH to pH=3 solution are shown in figure 2.16 that respectively shown in red, orange and green color. E_{corr} for 100 ppm HCHO+ 1000 ppm $\text{Cu}(\text{HCOO})_2$ solution was in the range 0.07 V vs. SSE to 0.17 V vs. SSE for 20 days immersion time. E_{corr} started from 0.1V vs. SSE, then increased to 0.14 V vs. SSE in 2 days immersion time, and then the value is around 0.1V vs. SSE to 0.17 V vs. SSE until the end of the measurement. The solution pH measurement shows that at the first immersion time the solution pH was 5.5 and at the fifth day the pH increased then in the 6 days decreased then constatanly increased again, and the pH final in 20 days is 5.51. E_{corr} for 1000 ppm $\text{Cu}(\text{HCOO})_2$ solution was in the range 0.01 to 0.08 V vs. SSE for 20 days immersion time. E_{corr} started from 0.01 V vs. SSE and then increased rapidly to 0.06 V vs. SSE in 3 days and after that was almost constant in the range 0.06 to 0.08 V vs. SSE. The solution pH measurement shows that at first immersion time the solution pH was 5.58 and it decreased to 4.59 in 3 days, then after that it increased slowly until the end of the measurement time to 5.29. E_{corr} for 1000 ppm $\text{Cu}(\text{HCOO})_2$ added HCOOH to pH=3 solution was in the range 0.04 to 0.11 V Vs. SSE for 20 days immersion time. E_{corr} started from 0.04, then increased to 0.1 in 3 days immersion time, and decreased slowly to reach 0.07 V Vs. SSE until the end of the measurement. The solution pH measurement shows that at the first immersion time the solution pH was 3 and continuously increased to 3.85 until the end of the measurement time.

All values of E_{corr} -pH-Time in Figure 2.16 are added to Figure 2.17. Table 2.2 is used to make the E -pH [19,20] diagram in Figure 2.17. All the chemcial potential values for the calculation are listed in Table 2.2 with assumption that the concentration of total dissolved copper ions $[\text{Cu}^{++}]$ was $10^{-3} \text{ mol kg}^{-1}$. In addition, the clear calculation to build E -pH diagram are explained in Appendix E -pH. The stable chemical species for copper tube that was immersed in 100 ppm HCHO+ 1000 ppm $\text{Cu}(\text{HCOO})_2$ solution is $\text{Cu}(\text{HCOO})_2$ at initial immersion; and after 20 days immersion, the stable chemical species is Cu_2O . The stable chemical species is for a copper tube that was immersed in 1000 ppm $\text{Cu}(\text{COOH})_2$ solution with solution pH 5.5 is Cu_2O . However, the stable

chemical species for copper tube that was immersed in 1000 ppm $\text{Cu}(\text{HCOO})_2$ added HCOOH to $\text{pH}=3$ solution is Cu^{++} at initial immersion; and after 20 days immersion, the stable chemical species is $\text{Cu}(\text{HCOO})_2$. This is also the reason why copper tube that had been immersed in the 1000 ppm $\text{Cu}(\text{HCOO})_2$ added HCOOH to $\text{pH}=3$ solution has a more prominent influence on the surface.

Table 2.2. Thermodynamic data (1 atm, 298 K). [20]

Substance Formula	State	Chemical Potential, $\mu^\phi/\text{kJ mol}^{-1}$
HCHO	aq	-131
HCOOH	aq	-372
HCOO^-	aq	-351
H_2CO_3	aq	-623
HCO_3^-	aq	-587
CO_2	aq	-386
H_2O	l	-237
OH^-	aq	-157
$\text{Cu}(\text{OH})_2$	aq	-249
CuO	cr	-130
Cu_2O	cr	-146
Cu^{2+}	aq	65
Cu^+	aq	50
$\text{Cu}(\text{HCOO})^+$	aq	-297
$\text{Cu}(\text{HCOO})_2$	aq	-636

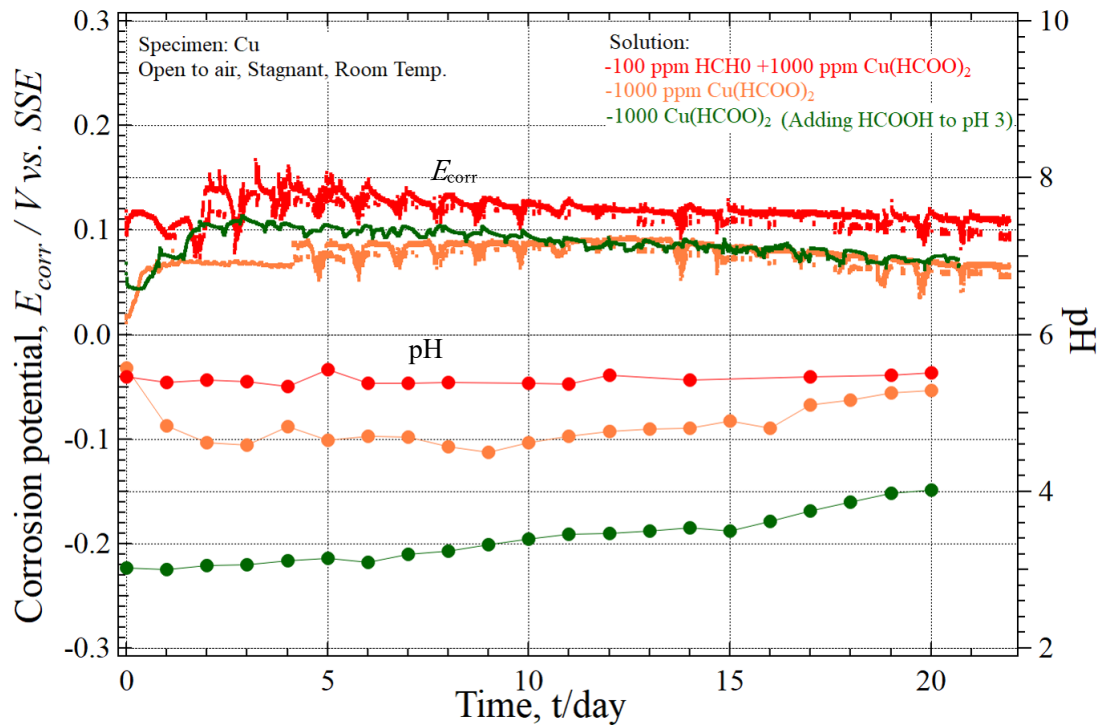


Figure 2.16 E_{corr} and pH measurement result of copper tube in 3 solutions condition.

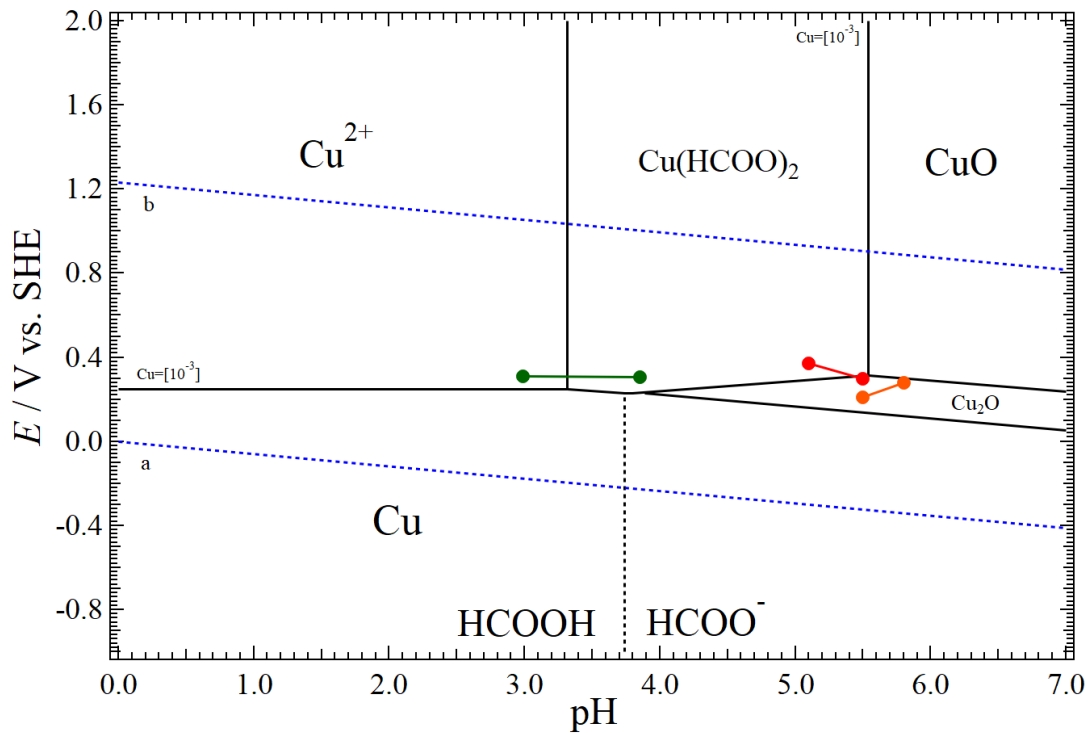
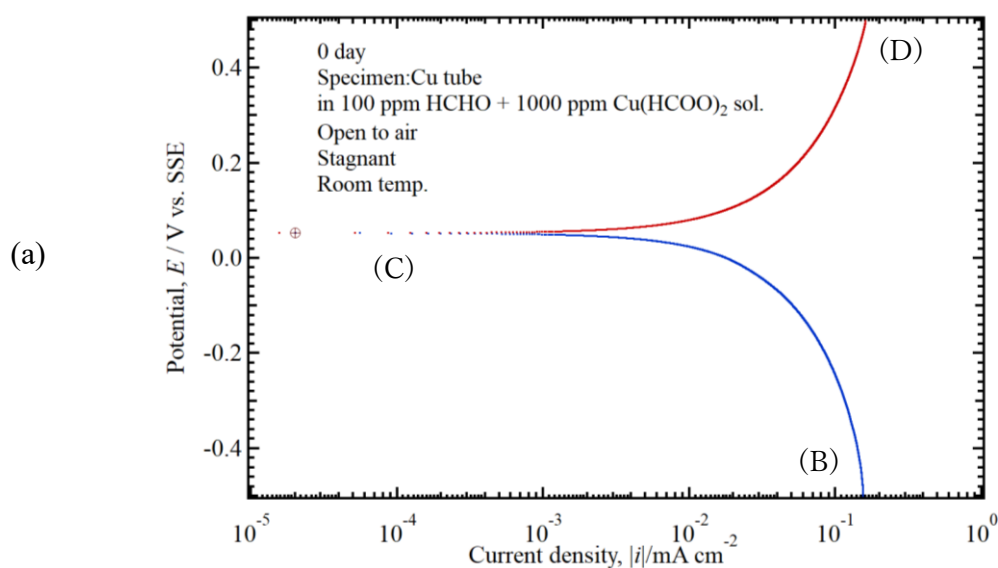


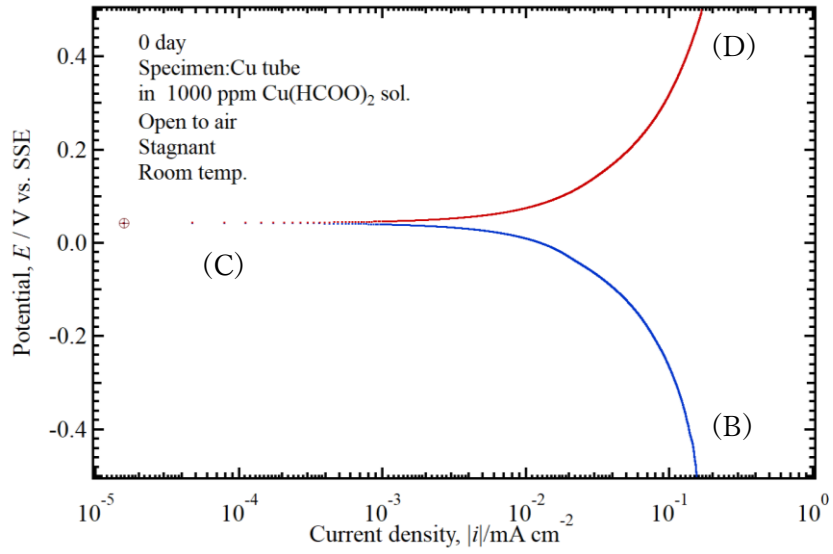
Figure 2.17 E -pH Diagram of Cu and $Cu(HCOO)_2$ with the assumption that the concentration of total dissolved copper ions $[Cu^{++}]$ was $10^{-3} \text{ mol kg}^{-1}$.

2.3.3. Polarization Curve

In this chapter, the result of polarization curve in 0 day and 20 days only be discussed. These are decided due to the result of cross section observation that the ant nest corrosion was found after 20 days immersion. Figure 2.18 is the polarization curve result of copper tube at 0 day and Figure 2.19 at 20 days in (a) 100 ppm HCHO+ 1000 ppm Cu(HCOO)₂ solution, (b) 1000 ppm Cu(HCOO)₂ solution and (c) 1000 ppm Cu(HCOO)₂ added HCOOH to pH=3 solution, respectively. The blue dot line is cathodic measurement and the red dot line is anodic measurement. The measurement was started after E_{ocp} for about 1 ks, then the measurement was performed from the E_{ocp} to point (B), and from point (B) the polarization operation was reserved to point (C). Then the anodic current begins to be observed at point (C), and beyond point (C) the anodic current exponentially flowed. At point (D) the polarization operation was finished. All of the polarization curve measurements show the current route of (B)–(C)–(D).



(b)



(c)

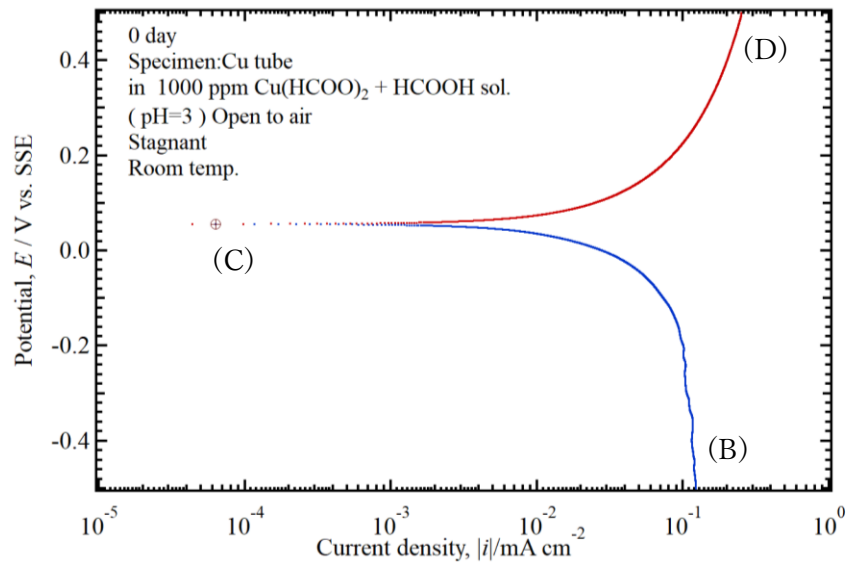
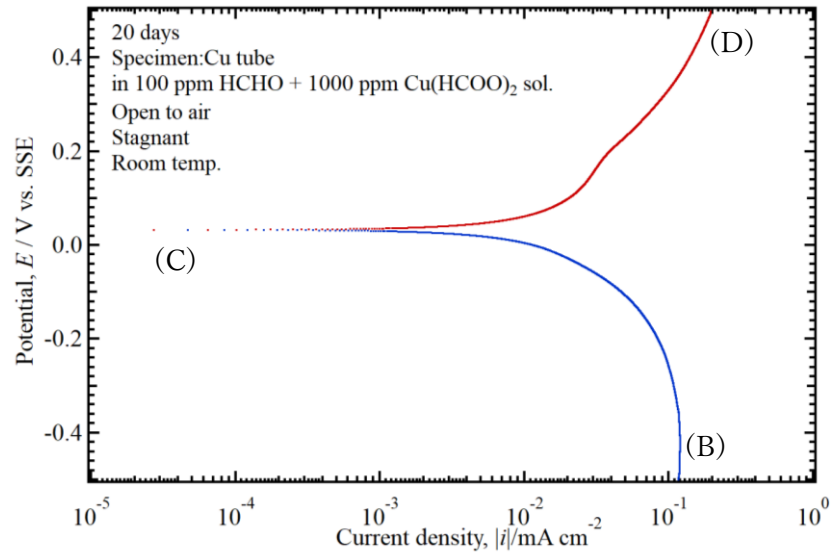
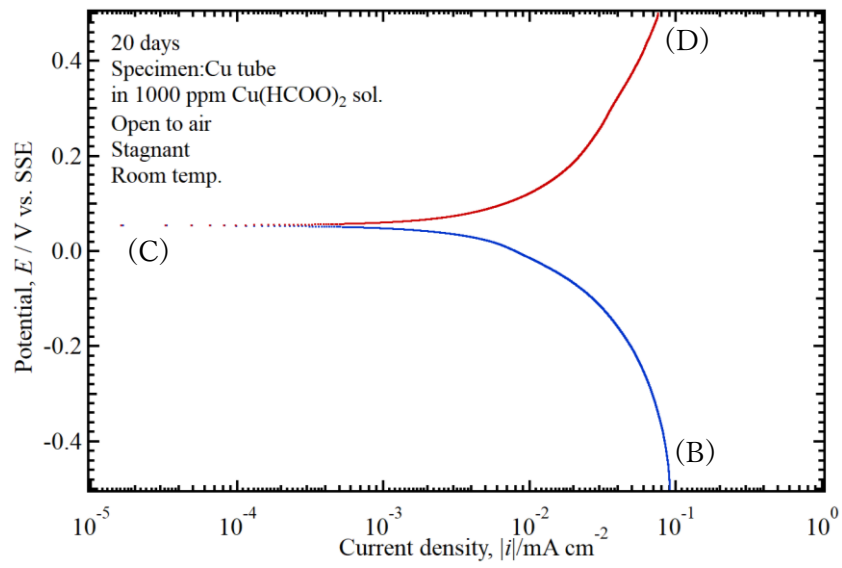


Figure 2.18 The polarization curve result of copper tube at 0 day in (a) 100 ppm HCHO+ 1000 ppm $\text{Cu}(\text{HCOO})_2$ solution, (b) 1000 ppm $\text{Cu}(\text{HCOO})_2$ solution and (c) 1000 ppm $\text{Cu}(\text{HCOO})_2$ added HCOOH to pH=3 solution

(a)



(b)



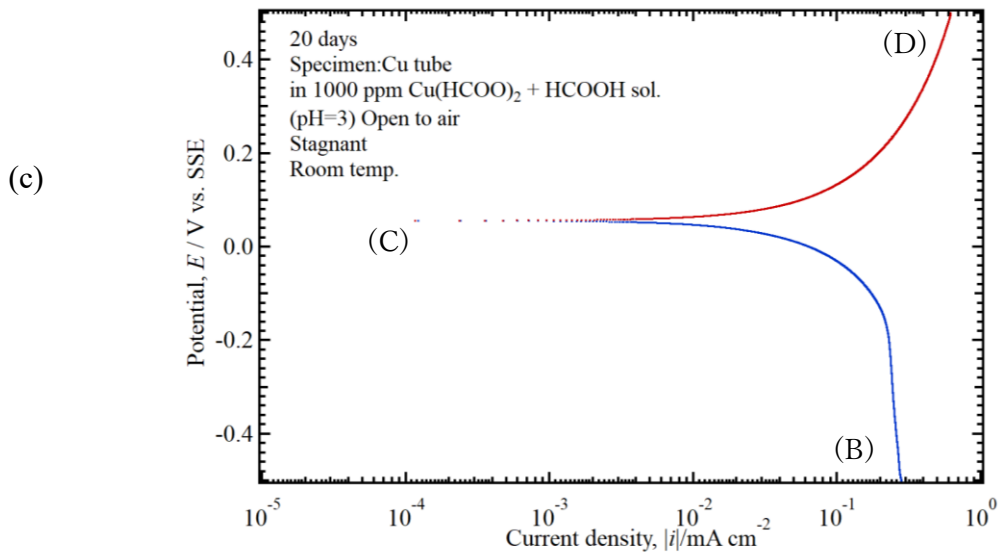


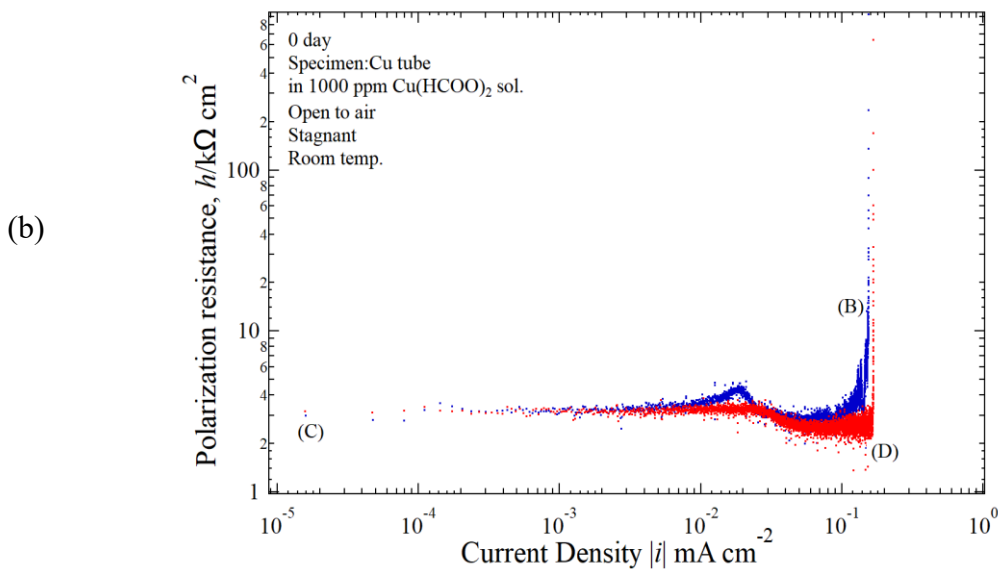
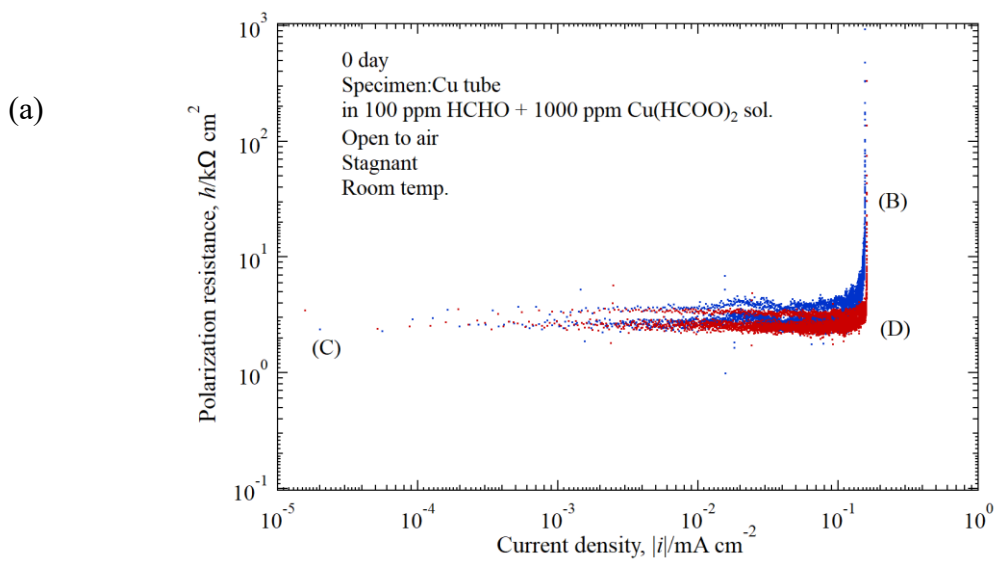
Figure 2.19 The polarization curve result of copper tube at 20 days in (a) 100 ppm HCHO+ 1000 ppm $\text{Cu}(\text{HCOO})_2$ solution, (b) 1000 ppm $\text{Cu}(\text{HCOO})_2$ solution and (c) 1000 ppm $\text{Cu}(\text{HCOO})_2$ added HCOOH to pH=3 solution

The $E(0)$ value for 0 days and 20 days for copper tube in 100 ppm HCHO+ 1000 ppm $\text{Cu}(\text{HCOO})_2$ solution respectively are 0.04 and 0.05 V vs. SSE and the $|i|$ plot around ($|i| < 0.05 \text{ mA cm}^{-2}$) for 0 day and ($|i| < 0.2 \text{ mA cm}^{-2}$) for 20 days. The $E(0)$ value for 0 days and 20 days for copper tube in 1000 ppm $\text{Cu}(\text{HCOO})_2$ solution respectively are 0.04 and 0.05 V vs. SSE and the $|i|$ plot around ($|i| < 0.05 \text{ mA cm}^{-2}$) for 0 day and ($|i| < 0.2 \text{ mA cm}^{-2}$) for 20 days. The $E(0)$ value for 0 days and 20 days for copper tube in 1000 ppm $\text{Cu}(\text{HCOO})_2$ solution and (c) 1000 ppm $\text{Cu}(\text{HCOO})_2$ added HCOOH to pH=3 solution respectively are 0.05 V vs. SSE and the $|i|$ plot around ($|i| < 0.25 \text{ mA cm}^{-2}$) for 0 days and ($|i| < 0.62 \text{ mA cm}^{-2}$) for 20 days.

2.3.4 Polarization Resistance Curve

The polarization resistance curve is made from the differential between potential divided to current density, $h(i)$ ($=dE/di$). The polarization resistance curve often has the advantage

of making a distinctive shape compared to the $E(i)$ expression curve. Figures 2.18 and 2.19 were converted to $\log h \sim \log |i|$ expression, as show in Figure 2.20 and 2.21. The result of polarization resistance curve in Figure 2.20 and 2.21 show horizontal line that can indicate that ANC was a rapid reaction system [5,14]. Also, the branch curve for anodic polarization resistance and cathodic polarization resistance were almost overlapped.



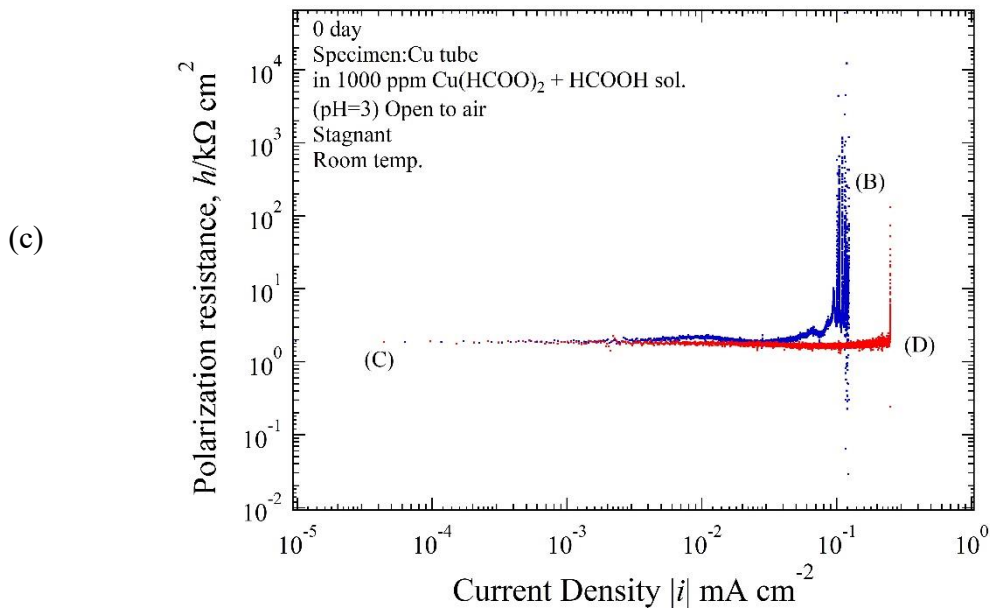
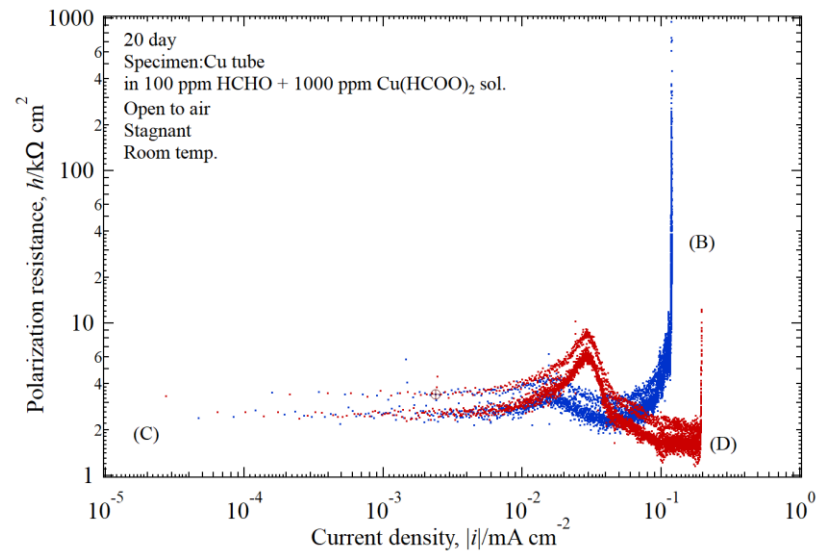


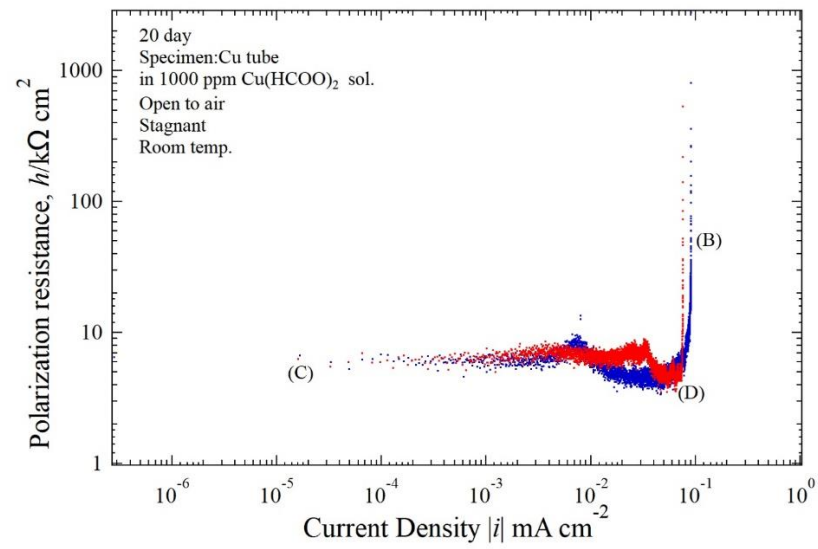
Figure 2.20 The polarization resistance curve result of copper tube at 0 day in (a) 100 ppm HCHO+ 1000 ppm $\text{Cu}(\text{HCOO})_2$ solution, (b) 1000 ppm $\text{Cu}(\text{HCOO})_2$ solution and (c) 1000 ppm $\text{Cu}(\text{HCOO})_2$ added HCOOH to pH=3 solution

The $h(0)$ values for 0 days and 20 days in for copper tube in 100 ppm HCHO+ 1000 ppm $\text{Cu}(\text{HCOO})_2$ solution respectively were $2.4 \text{ k}\Omega \text{ cm}^2$ and $2.4 \text{ k}\Omega \text{ cm}^2$. The $h(0)$ values for 0 days and 20 days in for copper tube in 1000 ppm $\text{Cu}(\text{HCOO})_2$ solution respectively were $3.2 \text{ k}\Omega \text{ cm}^2$ and $6.4 \text{ k}\Omega \text{ cm}^2$. The $h(0)$ values for 0 days and 20 days in for copper tube in 1000 ppm $\text{Cu}(\text{HCOO})_2$ added HCOOH to pH=3 solution respectively were $1.9 \text{ k}\Omega \text{ cm}^2$ and $0.9 \text{ k}\Omega \text{ cm}^2$.

(a)



(b)



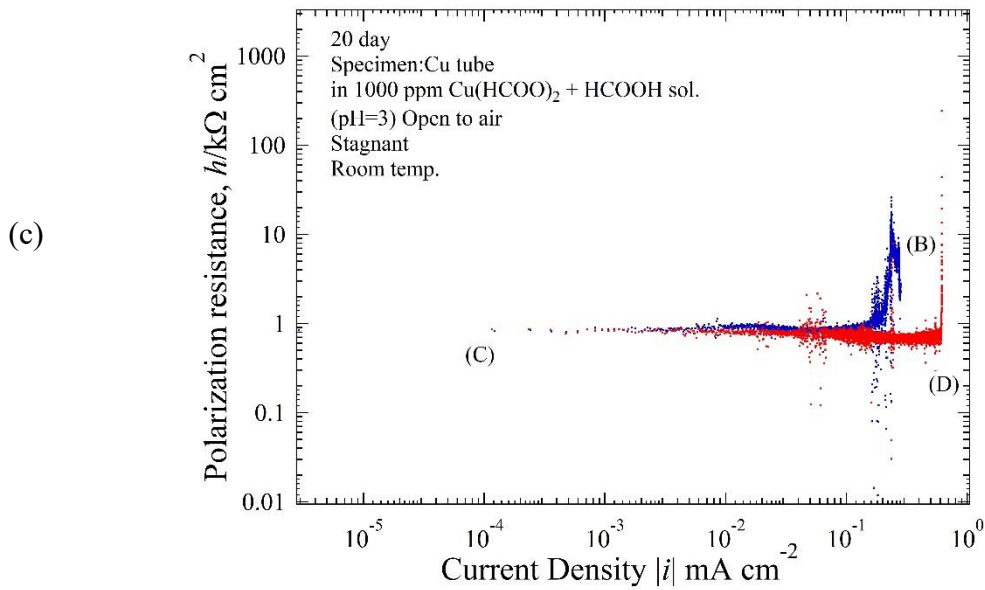


Figure 2.21 The polarization resistance curve result of copper tube at 20 days in (a) 100 ppm HCHO+ 1000 ppm Cu(HCOO)₂ solution, (b) 1000 ppm Cu(HCOO)₂ solution and (c) 1000 ppm Cu(HCOO)₂ added HCOOH to pH=3 solution

2.4. Ant-Nest Corrosion Mechanism on Copper tube

Section 2.3.2 explain the detail chemical compound result in all condition. Copper tube immersed in 100 ppm HCHO+ 1000 ppm Cu(HCOO)₂ solution and copper tube immersed in 1000 ppm Cu(HCOO)₂ solution have the same chemical compound result after 20 days immersion time. In addition, the cross section result show that the condition in these both condition almost have the same result. Therefore, in this sub chapter the mechanism and electrochemical value are focused in these both condition.

2.4.1. The Comproportionation and Disproportionation Reaction in the Corrosion Mechanism

Seri et.al. [17] reported that Cannizzaro reaction involved in the ANC in HCOOH solution is disproportionation reaction, which is expressed in equation (2.1):

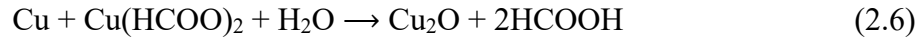
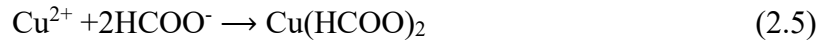
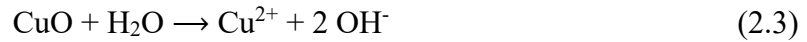


However, $\text{Cu}(\text{HCOO})_2$ will be dissociated as follow:



The dissociation constant ($\text{p}K_a$) of HCOO^- is 3.55, Therefore, HCOO^- in reaction equation (2.2) stay in the solution as a chemical form of HCOOH . The dissociation constant ($\text{p}K_a$) of HCOO^- is 3.55, Therefore, HCOO^- in reaction equation 2.2 stays in the solution as a chemical form of HCOOH . In other words, the environment in the test solution is composed of mixtures of Cu^{2+} , HCOOH , $\text{Cu}(\text{HCOO})_2$ and HCHO .

As mentioned before, Cu_2O were the chemical compound of copper tube that immersed in 100 ppm HCHO + 1000 ppm $\text{Cu}(\text{HCOO})_2$ solution and copper tube immersed in 1000 ppm $\text{Cu}(\text{HCOO})_2$ solution. Therefore, the copper tube immersed in this solution will change to Cu_2O . The literature [9,16,17] reported that the ANC starts from the weak point of copper tube that does not have oxide film. The oxide film such as CuO and $\text{Cu}(\text{OH})_2$ on the copper tube surface will also be changed into the Cu_2O by the following comproportionation reaction of Equation (6) via the acid-base reactions of Equations (2.3)–(2.5):



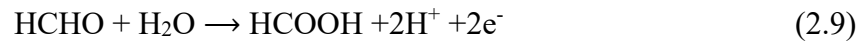
The DO as a reduction reaction also involved in at the early stage.



If, it is assumed that δ is 0.05 cm, so the diffusion limiting current density ($i_{\text{O}_2,\text{L}}$) of this case DO appears.

$$\begin{aligned}
i_{O_2,L} &= -4F \times \log[O_2]_{\text{bulk}} \\
&= -4F \times \frac{D_{O_2}}{\delta} \times [O_2]_{\text{bulk}} \\
&= -4 \times (96.5 \times 10^3 \text{ A s mol}^{-1}) \left(\frac{2 \times 10^{-5} \text{ cm}^2 \text{ s}^{-1}}{0.05 \text{ cm}} \right) \left(\frac{7 \times 10^{-3} \text{ g dm}^{-1}}{32 \text{ g mol}^{-1}} \right) \\
&\approx -34 \times 10^{-3} \text{ mA cm}^{-2} \tag{2.8}
\end{aligned}$$

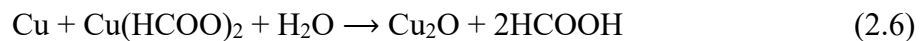
Limiting current range of $i_{O_2,L}$ appears in the vicinity of $-34 \times 10^{-3} \text{ mA} \cdot \text{cm}^{-2}$. However, The consuming electron in the oxidation reaction by Equation (2.7) is considered as a pair reaction of oxidation reaction of HCHO, which is shown as below:



The total reaction by summation of Equation (2.7) and (2.9) is shown as:



Therefore, the DO in the process of the ANC will be consumed by the oxidation of HCHO, especially in the pitting hole. Reaction in equation (2.7) as a cathode reaction is hardly involved in the whole process for the ANC, except for the early immersion time. Sakai et al [21] reports that the dissolved oxygen is one of the strong influences in the mechanism of the copper tube. The DO will probably not always become a major cathodic reaction for the ANC process not only because of the consumption of DO by Equation (2.10) but it will also be difficult to access the narrow pitting hole with complex hole routes. As shown in Figures 2.15, the result of EPMA analysis indicates that the oxygen in the pitting hole in 30 days was less than oxygen in the pitting hole in 15 days. The following comproportionation reaction had an important role in the deep pitting attack, which is expressed as Equation (2.6).



Dividing the whole reaction into the redox reactions, the half reactions composed above are:



Cu_2O as the reaction product is considered to act as a highly positive catalyst for Cannizzaro reaction in the pitting hole. Coexistence of HCHO , H_2CO_3 , and HCOOH in the narrow pitting hole probably will make an important factor for unstable corrosion environment such as change of the solution pH.

2.4.2. Polarization Curve and Polarization Resistance Curve Analysis.

The polarization resistance curve of Copper tube immersed in 100 ppm HCHO + 1000 ppm $\text{Cu}(\text{HCOO})_2$ solution and copper tube immersed in 1000 ppm $\text{Cu}(\text{HCOO})_2$ solution for 20 days immersion time show that there were no straight line with gradient of $\frac{d \log h}{d \log i} = -1$. Therefore, it is classified as a fast system [22]. Seri et al [23] report observations about the classification of irreversible, reversible and quasi reversible reaction. Since all the polarization resistance curve (Figures 2.20-2.21) have a longer horizontal line with smaller $h(0)$, this can be classified as a resersible reaction which means that the value of α_{Z_a} and β_{Z_b} approximated 1. The values of $i_{Ox,L}$ are from the polarization resistance curve (Figures 2.20-2.21). Since the polarization resistance curve of copper tube immersed in 100 ppm HCHO + 1000 ppm $\text{Cu}(\text{HCOO})_2$ solution and copper tube immersed in 1000 ppm $\text{Cu}(\text{HCOO})_2$ solution for 20 days immersion time is classified as a fast system. The fast system then leads us to the spontaneous situation described as the following spontaneous equations [22]:

$$i = i_a + i_c \quad (2.13)$$

$$h(i) = \frac{1}{1/h_a(i_a) + 1/h_c(i_c)} \quad (2.14)$$

$$h_a(i_a) = \frac{RT}{zF} \frac{1}{i_a} + r_A = \frac{0.013}{i_a} + r_A \quad (2.15)$$

$$h_c(i_c) = \frac{RT}{zF} \left(\frac{2}{-i_c} + \frac{1}{i_c - i_{\text{Cu(HCOO)}_2, \text{L}}} \right) + r_C \quad (2.16)$$

$$i_a(i) = i_a(0) + \frac{h(0)}{h_a(i_a(0))} \cdot i \quad (2.17)$$

$$i_c(i) = i_c(0) + \frac{h(0)}{h_c(i_c(0))} \cdot i \quad (2.18)$$

where r_A and r_C represent the physical resistances such as an oxide film. In this experiment, we could assume that the oxide film resistance of the anode direction and cathode reaction are almost the same; $r_A = r_C$. The ANC is categorized as the fast system. Therefore, the $i_{\text{Cu(HCOO)}_2, \text{L}}$ as the anodic branch rate in equation 2.12 can participate in the corrosion rate as the limiting current density, because the activity of the metallic copper shows a unit and there is plenty of water as reactant. So, the total net current i is simplified as:

$$i = i_a + i_c = i_a + i_{\text{Cu(HCOO)}_2, \text{L}} \quad (2.19)$$

In this situation, $h(i)$ will be arranged into:

$$h(i) = \frac{dE}{di} = \frac{dE}{d(i_a + i_{\text{Cu(HCOO)}_2, \text{L}})} \approx h_a(i_a) \quad (2.20)$$

Rearranging Equation (2.14), moreover (2.15), we can obtain the following relation:

$$h(i) = h_a(i - i_{\text{Cu(HCOO)}_2, \text{L}}) = \frac{0.013}{i - i_{\text{Cu(HCOO)}_2, \text{L}}} + r_A \quad (2.21)$$

The theoretical value for the $i_{\text{Cu(HCOO)}_2, \text{L}}$ at the stagnant state ($\delta \approx 0.05$ cm) can be calculated as:

$$i_{\text{Cu(HCOO)}_2, \text{L}} = -zFk_{\text{Cu(HCOO)}_2} [\text{Cu(HCOO)}_2]_{\text{bulk}} \quad (2.22)$$

$$\begin{aligned}
&= -zF \frac{D_{\text{Cu}(\text{HCOO})_2}}{\delta} [\text{Cu}(\text{HCOO})_2]_{\text{bulk}} \\
&\approx -0.12 \text{ mA cm}^{-2}
\end{aligned}$$

In this case, Equation (2.21) is corrected to:

$$h(i) = \frac{0.013}{i + 0.12} + r_A \quad (2.23)$$

Using the above equation, the theoretical $h(0)$ value is calculated as:

$$h(0) = \frac{0.013}{0.12} + r_A = 0.11 \text{ k}\Omega \text{ cm}^2 + r_A \quad (2.24)$$

On the other hand, the experimental $h(0)$ value copper tube immersed in 100 ppm HCHO+ 1000 ppm $\text{Cu}(\text{HCOO})_2$ solution is $2.4 \text{ k}\Omega \text{ cm}^2$. The experimental $h(0)$ value copper tube immersed in 1000 ppm $\text{Cu}(\text{HCOO})_2$ solution is $6.4 \text{ k}\Omega \text{ cm}^2$. Therefore, r_A will be estimated by $r_A = 2.4 - 0.11 \approx 2.3 \text{ k}\Omega \text{ cm}^2$ for copper tube immersed in 100 ppm HCHO+ 1000 ppm $\text{Cu}(\text{HCOO})_2$ solution and $r_A = 6.4 - 0.11 \approx 6.3 \text{ k}\Omega \text{ cm}^2$ for copper tube immersed in 1000 ppm $\text{Cu}(\text{HCOO})_2$ solution. Then Equation (2.25) and (2.26) expressed both conditions:

$$h(i) = \frac{0.013}{i + 0.12} + 2.3 \quad (2.25)$$

$$h(i) = \frac{0.013}{i + 0.12} + 6.3 \quad (2.26)$$

2.4.3. The Relationship between $h(i)$ and $E(i)$ Curve

The characteristics of $E(i)$ of the copper tube copper tube immersed in 100 ppm HCHO+ 1000 ppm $\text{Cu}(\text{HCOO})_2$ solution and copper tube immersed in 1000 ppm $\text{Cu}(\text{HCOO})_2$ solution are categorized as a fast system. In addition, if the $h(i)$ in equation 2.25 and 2.26 are correct, the experimental $E(i)$ curve in Figure 2.22 will agree with the curve when theoretically solving the differential equation of $h(i)$ at an initial condition of $(0 \text{ mA cm}^{-2}, E(0))$. Since the E_{ocp} in the steady state (20 days immersion) indicates around 0.05 V for copper tube copper tube immersed in 100 ppm HCHO+ 1000 ppm $\text{Cu}(\text{HCOO})_2$ solution and 0.04 V for copper tube immersed in 1000 ppm $\text{Cu}(\text{HCOO})_2$ solution, the equation is concretely shown as equation 2.27 for copper tube immersed in 100 ppm

HCHO+ 1000 ppm Cu(HCOO)₂ solution and equation 2.28 for copper tube immersed in 1000 ppm Cu(HCOO)₂ solution :

$$\int_{E(0)}^{E(i)} dE = \int_0^i \left(\frac{0.013}{i + 0.12} + 2.3 \right) di \quad (2.27)$$

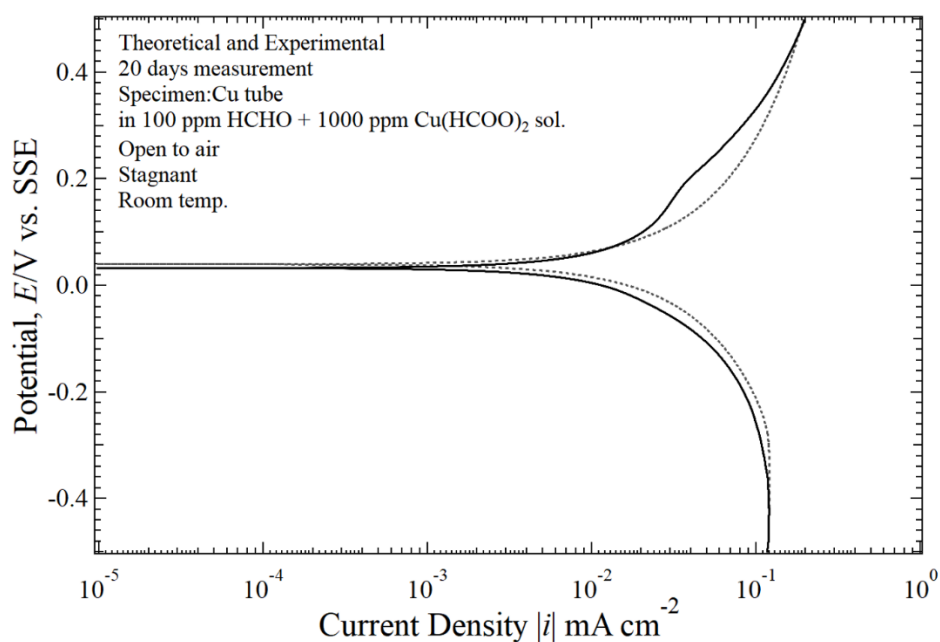
$$\int_{E(0)}^{E(i)} dE = \int_0^i \left(\frac{0.013}{i + 0.12} + 6.3 \right) di \quad (2.28)$$

To solve the above, the following relation is obtained:

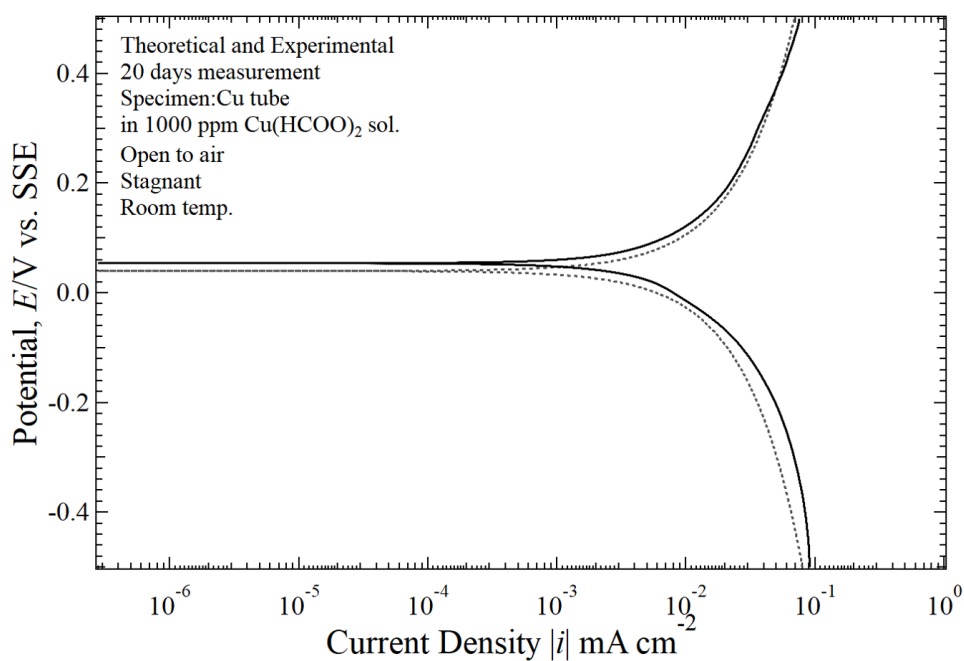
$$\begin{aligned} E(i) &= E(0) + 0.013 \ln \frac{i + 0.12}{0.12} + 3.2i \\ &= 0.05 + 0.013 \ln \frac{i + 0.12}{0.12} + 2.3i \end{aligned} \quad (2.29)$$

$$\begin{aligned} E(i) &= E(0) + 0.013 \ln \frac{i + 0.12}{0.12} + 2.6i \\ &= 0.04 + 0.013 \ln \frac{i + 0.12}{0.12} + 6.3i \end{aligned} \quad (2.30)$$

Figure 2.22 shows the result of superimposition of the experimental polarization curve between theoretical and experimental. The theoretical curve overlapped with the experimental curve indicates that theoretical analysis using the polarization resistance technique is almost correct and is useful for describing the behavior in this experiment.



(a)



(b)

Figure 2.22. The experimental polarization curve (Black Line) and theoretical polarization curve (Gray dot line) of the copper tube immersed in (a) 100 ppm HCHO+ 1000 ppm Cu(HCOO)₂ solution and (b) copper tube immersed in 1000 ppm Cu(HCOO)₂ solution

2.5. Conclusion

Ant Nest corrosion is typical of local corrosion that has corroded pitting hole traces of several micron size morphologies that are similar to the nest of ants. Ant Nest corrosion occurred on copper tube that immersed in 100 ppm HCHO+ 1000 ppm Cu(HCOO)₂ solution, 1000 ppm Cu(HCOO)₂ solution and 1000 ppm Cu(HCOO)₂ added HCOOH to pH=3 solution. It took 20 days immersion time period to produce ANC. Copper tube that immersed in 100 ppm HCHO+ 1000 ppm Cu(HCOO)₂ solution, 1000 ppm Cu(HCOO)₂ solution almost have the same behaviour compared to copper tube that immersed in 1000 ppm Cu(HCOO)₂ added HCOOH to pH=3 solution. The polarization curve of the copper tube specimens were measured at initial immersion (0 days) and late immersion time (20 days). It was shown that the polarization curve for 0 days and 20 days do not appear changed. Analysis using the polarization resistance curves revealed that these is typical of extremely fast corrosion. In addition, the diffusion limiting current of Cu(HCOO)₂, and oxide film resistance influenced the ant nest corrosion mechanism in the steady state. It was explained that the comproportional reaction and disproportional reaction play an important role in the whole mechanism of ant nest corrosion on the copper tube.

Reference

1. CDA Publication A4015-14/19: Copper Tube Handbook.
2. Davis, L.W.; Gertler, P.J. Contribution of air conditioning adoption to future energy use under global warming. *Proc. Natl. Acad. Sci. USA* 2015, 112, 5962–5967.
3. J.O. Edwards, R.I. Hamilton, J.B. Gilmour, Early Corrosion Failures in Copper Heat Exchanger Tubing, 16 (1977), pp. 18–20.
4. López-Delgado, A.; Cano, E.; Bastidas, J.M.; López, F.A. A laboratory study of the

- effect of acetic acid vapor on atmospheric copper corrosion. *J. Electrochem. Soc.* 1998, 145, 4140–4147.
5. Cano, E.; Simancas, J.; Polo, J.L.; Torres, C.L.; Bastidas, J.M.; Alcolea, J. Early corrosion failure of copper tubing used in air-conditioning units. *Mater. Corros.* 1999, 50, 103–110.
 6. Miya, K. Proceeding of the 58th Japan Conference on Materials and Environments (JSCE 2011), Japan, 2011; p. 117.
 7. Sakai, M.; Watanabe J., Corrosion Behavior of Phosphorous Deoxidized Copper Tubes in Copper (II) Formate and Copper (II) Acetate Solution. *Zairyo_to_Kankyo/Corros. Eng. Jpn.* 2016, 65, pp. 462-466.
 8. Notoya, T.; Atsumi, T.; Kawano, K.; Nagata, K.; Kelly, G.J. Localized “ant’s nest” corrosion in copper tubes and its prevention. In *Trends in Electrochemistry and Corrosion at the Beginning of 21st Century*, Brillas, E., Ed.; Spain, 2004; pp. 845–855.
 9. Baba, H.; Kodama, T. Localized corrosion of copper in wet organic acid vapor. *Zairyo Kankyo/Corros. Eng.* 1995, 44, 233–239.
 10. Bastidas, J.M.; López-Delgado, A.; Cano, E.; Polo, J.L.; López, F.A. Copper corrosion mechanism in the presence of formic acid vapor for short exposure times. *J. Electrochem. Soc.* 2000, 147, 999–1005.
 11. Sakai, M.; Shirahata, K. Ant Nest Corrosion Developed on Phosphorus Deoxidized and Oxygen-Free Copper Tube. *Zairyo_to_Kankyo/Corros. Eng. Jpn.* 2016, 65, 341–349.
 12. Elliott, P.; Corbett, R.A. *CORROSION/99, Paper Number 99342*; NACE International: Houston, TX, USA, 1999.

13. Corbett, R.A.; Elliott, P.; *CORROSION/2000, Paper Number 00646*; NACE International: Houston, TX, USA, 2000.
14. Chandra, K.; Kain, V.; Shetty, P.S.; Kishan, R. Failure analysis of copper tube used in a refrigerating plant. *Eng. Fail. Anal.* 2014, *37*, 1–11.
15. Zhou, J.; Yan, L.; Tang, J.; Sun, Z.; Ma, L. Interactive effect of ant nest corrosion and stress corrosion on the failure of copper tubes. *Eng. Fail. Anal.* 2018, *83*, 9–16.
16. Peltola, H.; Lindgren, M. Failure analysis of a copper tube in a finned heat exchanger. *Eng. Fail. Anal.* 2015, *51*, 83–97.
17. Seri, O.; Ichimiya, H.; Sakai, M. Ant's Nest-Like Pitting Attack on Copper Tubes and Its Analysis. *Zairyo_to_Kankyo/Corros. Eng. Jpn.* 2016, *65*, 21–30.
18. Takashi, U.; Situmorang, R.S.; Seri, O. Effect of Copper Formate on Ant's Nest-like Pitting Attack on Copper Tube. *J. Jpn. Inst. Copp.* 2017, *56*, 147–152.
19. Pourbaix, M. *Atlas of Electrochemical Equilibria in Aqueous Solution*; Pergamon Press: Oxford, UK, 1966; pp. 385, 504.
20. Wagman, D.D.; Evans, W.H.; Parker, V.B.; Schumm, R.H.; Halow, I. The NBS Table of Chemical Thermodynamic properties. *J. Phys. Chem. Ref. Data* 1982, *11* (Suppl. 2), 37, 38, 154.
21. Sakai, M.; Takahashi, H. Effect of Dissolved Oxygen on Corrosion behavior of Phosphorous Deoxidized Copper Tube in Formic Acid Solution. *Zairyo_to_Kankyo/Corros. Eng. Jpn.* 2016, *65*, 510–514.
22. Seri, O.; Itoh, Y. Differentiating polarization curve technique for determining the exchange current density of hydrogen electrode reaction. *Electrochim. Acta* 2016, *218*, 345–355.
23. Seri, O.; Siree, B. The Differentiating Polarization Curve Technique for the Tafel Parameter Estimation. *Catalysts* 2017, *7*, 239, doi:10.3390/catal7080239.

Chapter 3
Estimation of Exchange Current Density
on Copper Electrode by Using
Differential Polarization Method

3.1. Introduction

One of the most fundamental and important reactions in the electrochemistry is hydrogen evolution reaction because hydrogen evolution reaction (HER) contributes in the next energy society such as fuel cell, battery development, etc [1-3]. Pt electrode is commonly used for *HER* due to its electro-activity efficiency but its high price increase production cost. In this research is focused in copper electrode since *HER* using copper metal or its complex much less have been investigated [4-7]. However, many researches have been done to find another electrode with higher efficiency, stability and lower cost [8,9].

As well known, exchange current density (i_0) is used to evaluate the catalyst performance of an electrode. The exchange current density (i_0) is commonly calculated by using Tafel extrapolation method (TEM) [10]. Tafel extrapolation method ($\eta = a + b \log |i|$) have been using in many papers, books and publication research to calculate the exchange current density (i_0) on the hydrogen evolution reaction; but in same condition environment by different publication, it showed a different value of the exchanges current density [11-16]. For the example: the i_0 of the copper electrode from the same H_2SO_4 solution environment has variation values from $10^{-5.6}$ to $10^{-2.9}$ mA.cm⁻². [13]. This different results might be caused by the improper reading or interpretation and also the individual error on reading the Tafel graph since the TEM is calculated by using the logarithm of the cathodic current density ($\log |i|$) and its overvoltage (η) [14-15]. In addition, it is important to detail in many factors that influence the calculation such as the physical factors like solution resistance and oxide film on electrode [16-22].

For this reason, the new method that called differential polarization method (DPM) is introduced to answer the improper reading of i_0 from the Tafel graph [17,18]. In addition,

the physical resistance that might influenced the i_0 calculation can be removed rationally in DPM. In the This research, the hydrogen evolution reaction experiment is conducted by using copper electrode in $0.5 \text{ mol dm}^{-3} \text{ H}_2\text{SO}_4$ solution. The i_0 result of measurements are calculated and compared by using The differential polarization method (DPM) and Tafel extrapolation method (TEM).

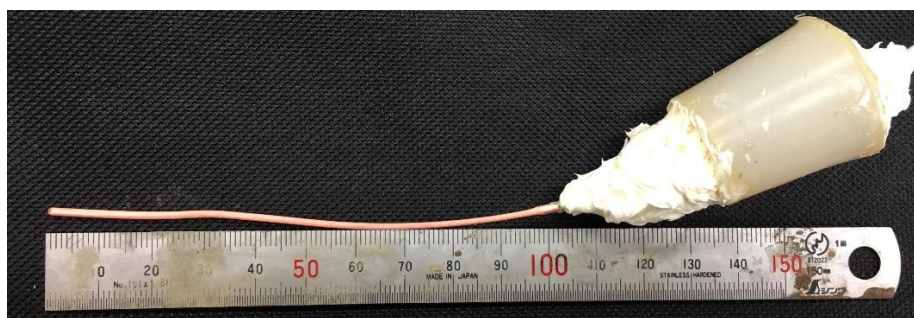
3.2. Experimental Method

3.2.1 Specimens

Figure 1 (a) is the copper electrode produced by Sigma-Aldrich with 99.999% Cu as working electrode. The copper electrode exposed surface area is 6.63 cm^2 . The Cu electrode was pretreated by ultrasonic vibration in H_2SO_4 solution for 300 s at room temperature ($\approx 298 \text{ K}$). Figure 1 (b) is the counter electrode, Platinum, produced by NILACO Ltd with 99.98% Pt. The counter electrode was a coiled Pt wire with an exposure area of 5 cm^2 . The Pt was washed with acetone and then dipped into 30% nitric acid solution at room temperature ($\approx 298 \text{ K}$) to clean up its surface. At last, it was rinsed thoroughly with deionized water and then air-dried before the test.

3.2.2 Test Solution

The sulfuric acid solution was used as the test solution (98% H_2SO_4 , Wako Pure Chemical Industries Ltd.). The test solution was adjusted to $0.5 \text{ mol dm}^{-3} \text{ H}_2\text{SO}_4$ solution. The solution temperature was at room temperature ($\approx 298 \text{ K}$). The pH of the $0.5 \text{ mol dm}^{-3} \text{ H}_2\text{SO}_4$ solution was 0.3, the electric conductivity, κ , was $\geq 20 \text{ S m}^{-1}$, and the dissolved oxygen (DO) was around 0.4 ppm or lower. During the experiment, was continuously bubbled with hydrogen gas (99.9999 % H_2).



(a)



(b)

Figure 3.1 (a) Copper as working electrode and (b) platinum as a counter electrode

3.2.3 Measurement Method

The measurement method is shown in figure 3.2. Hokuto Denko Inc. HZ7000 was employed for the linear sweep voltammetry. The reference electrode is Ag/AgCl electrode in the saturated KCl solution (DKK-TOA Co., HS-305D). All electrode potentials that were experimentally measured are converted to V vs. SHE. The distance between the working and reference electrode was 1 cm or less. The experimental polarization curve, $E_{\text{exp}}(i)$, was not converted for iR drop.

There are 2 condition of measurement:

1. Measurement in both Cathode and anode condition (1 cycle)
2. Measurement in 5 Cycle

In all measurements, the scan rate is 0.1 mV s^{-1} and solutions were stirred. Igor Pro 6 was used as mathematically smoothed software for the result of measurement that caused by the scattering data from slow scan rate operation

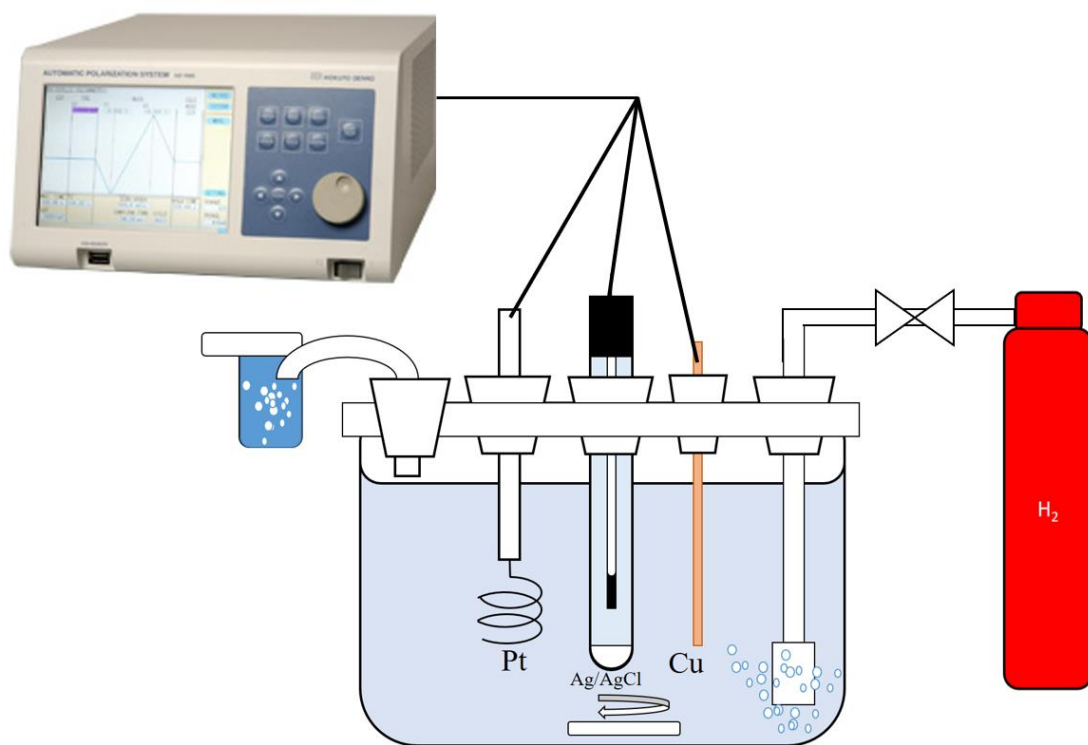


Figure 3.2 Measurement method

3.3. Results

3.3.1. E_{ocp} , pH-Time.

The result of open circuit potential measurement (E_{ocp}) of copper tube in 0.5 mol dm^{-3} H_2SO_4 aqueous solution at room temperature, stagnant, and was continuously bubbled with hydrogen is shown in Figure 3.3. The measurement was conducted in around 16 hours. The pH solution was constant in 0.3 during the measurement. In the initial stage (0 hours), E_{ocp} at the initial stage of the immersion was around -0.19 V vs SHE. Then, it decreased rapidly to around -0.25 V vs. SHE during 1 hour. It showed an almost constant value of around -0.25 V vs. SHE after 2 hours.

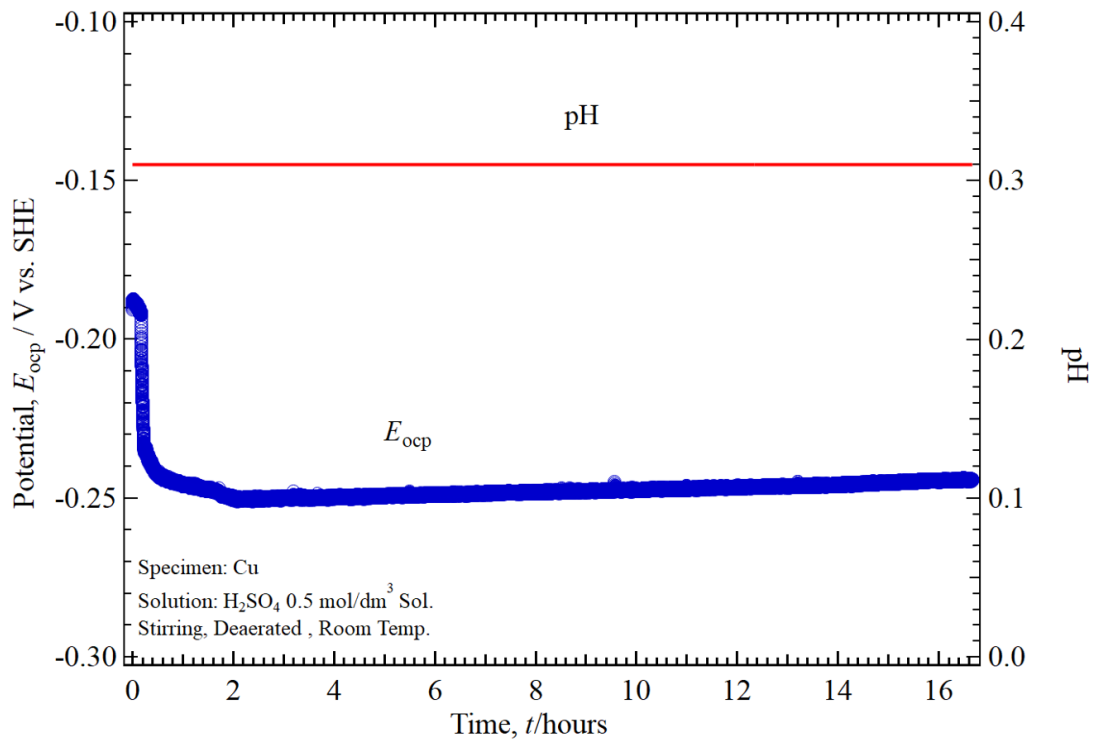


Figure 3.3 E_{oxp} , pH-Time curve of the copper electrode in $0.5 \text{ mol dm}^{-3} \text{ H}_2\text{SO}_4$ solution.

3.3.2. Polarization Curve Result

The polarization measurement curve result of the copper electrode experiment that was conducted in $0.5 \text{ mol.dm}^{-3} \text{ H}_2\text{SO}_4$ solution and continuously bubbled with H_2 gas is shown as $E_{exp} \sim \log |i|$ curve in Figure 3.4 and Figure 3.5. Figure 3.4 shows the polarization curve result of the copper electrode in cathode and anode condition (1 cycle). (B)→(A) is cathode measurement (blue color) and (A)→(C) is anode measurement (red color). Figure 3.5 shows the polarization curve result of the copper electrode in $0.5 \text{ mol dm}^{-3} \text{ H}_2\text{SO}_4$ solution in 5 Cycle. The measurement started from point (A) to point (B) and from point (B) reversed to point (A). From point (A), it was continuous to point (C), and after reaching point (C), it reversed back to point (A). It repeated for 5 cycles and stopped in point (A). Cycles 1 to 5 are distinguished by different colors which are blue, brown,

yellow, red, and black, respectively. In each cycle, the experimental polarization curve is shown with a light-colored circle and its smoothed curve is shown with a dark-colored dot. The behavior of cycle 1 was influenced by the dissolved oxygen of the solution [23]. Therefore, if cycle 1 is compared to cycle 2~5, cycle 1 has a different behavior. In addition, Figure 3.4 and Figure 3.5 show $E_{\text{exp}}(0) \approx -0.14$ V vs. SHE.

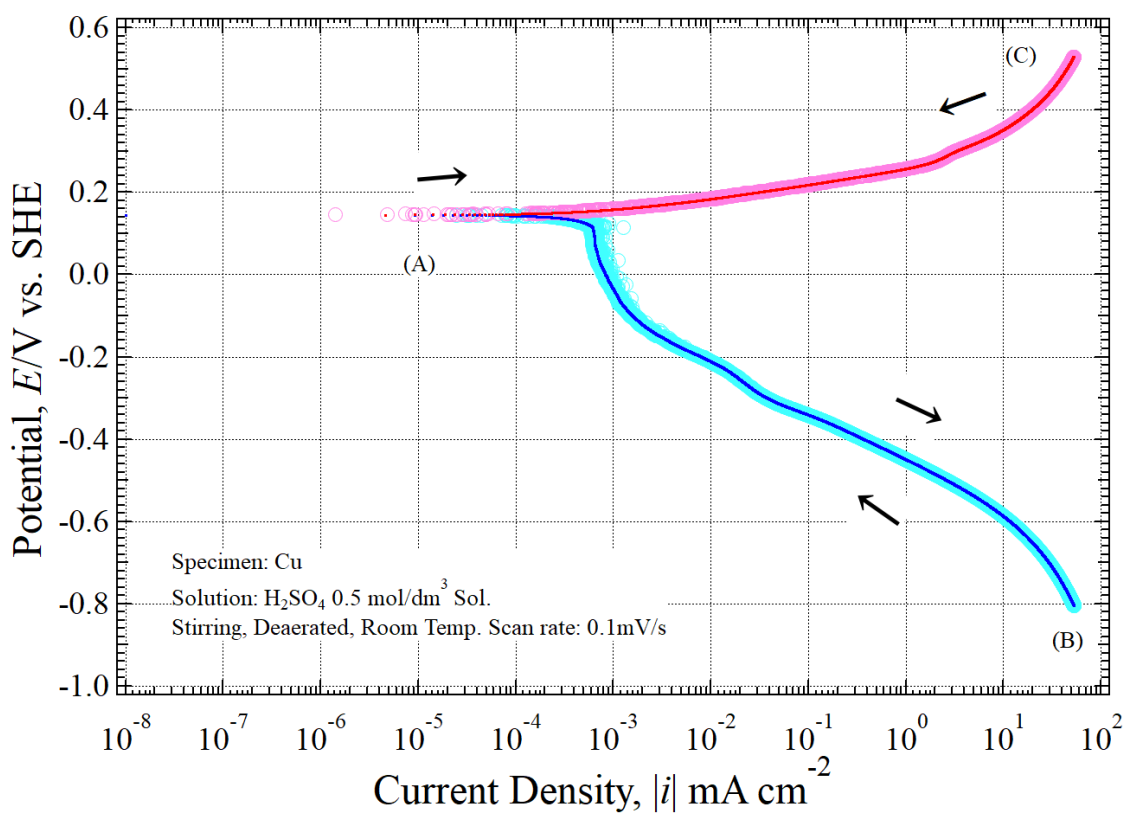


Figure 3.4 Polarization curve of the copper electrode in $0.5 \text{ mol dm}^{-3} \text{ H}_2\text{SO}_4$ solution, deaerated with H_2 gas bubbling, stirring, in room temperature and only in cathode and anode condition (1 Cycle)

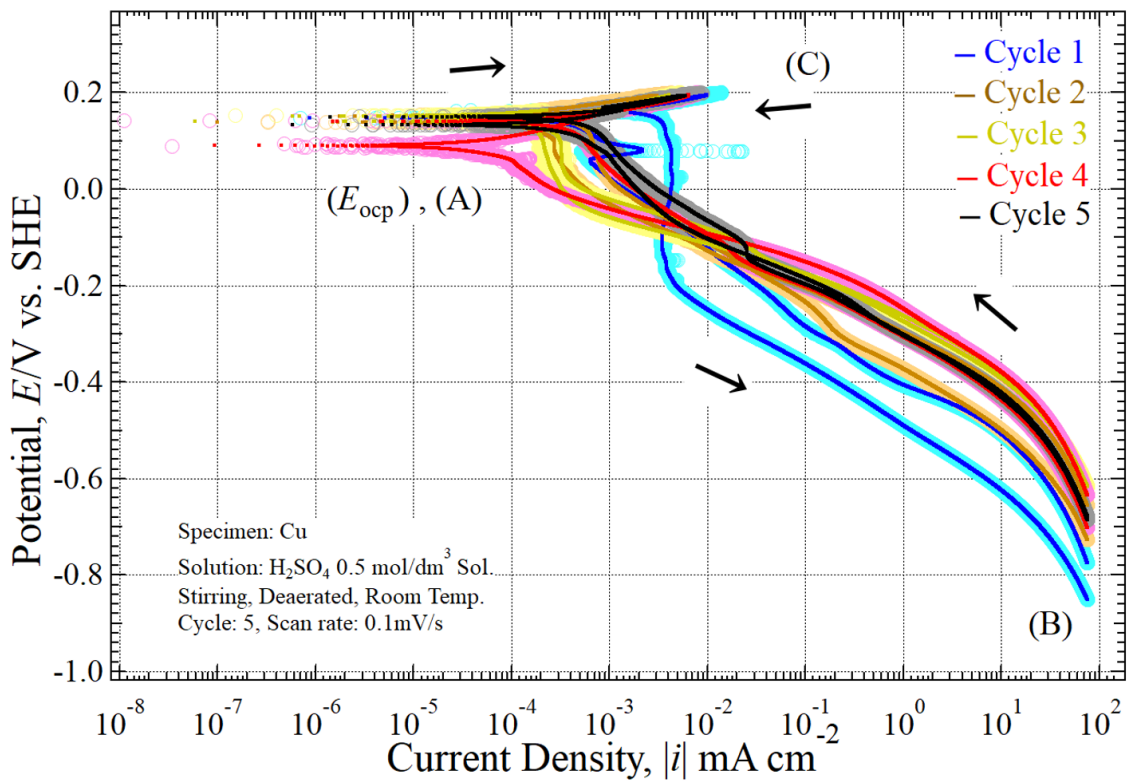


Figure 3.5 Polarization curve of the copper electrode in $0.5 \text{ mol dm}^{-3} \text{ H}_2\text{SO}_4$ solution, deaerated with H_2 gas bubbling, stirring, in room temperature in 5 Cycle

3.3.3. Polarization Resistance Result

Polarization resistance curve of these experiments are plotted by differentiating, $h_{\text{exp}}(i)$ ($= \Delta E_{\text{exp}}/\Delta i$). Then the result of $\log h_{\text{exp}}$ is plotted to the $\log h_{\text{exp}}-\log|i|$ curve. In this differentiation, the smoothing data in Figure 3.4 and Figure 3.5 are used because the smoothed data in Figure 3.4 and Figure 3.5 which overlapped the experiment data is acceptable to represent the experiment data. Therefore, the smoothed $E_{\text{exp}}(i)$ was used to make the polarization resistance curve. Figure 3.6 and Figure 3.7 show the polarization resistance curve of copper electrode in $0.5 \text{ mol dm}^{-3} \text{ H}_2\text{SO}_4$ solution, deaerated with H_2 gas bubbling, stirring at room temperature in cathode and anode condition (1 Cycle), in 5

Cycle set, respectively. As a reference of the proposed method, a purple dot line with a gradient of $d \log h / d \log |i| = -1$ was added in Figure 3.6 and Figure 3.7. The polarization resistance curve of copper electrode in Figure 3.6 has horizontal line of $h_{\text{exp}} (i \leq 1 \times 10^{-4} \text{ mA cm}^{-2}) \approx 23.2 \text{ k}\Omega \text{ cm}^2$ and $h_{\text{exp}} (i \geq 40 \text{ mA cm}^{-2}) \approx 0.004 \text{ k}\Omega \text{ cm}^2$. The polarization resistance curve of copper electrode in Figure 3.7 has many horizontal line of $h_{\text{exp}} (i \leq 6 \times 10^{-5} \text{ mA cm}^{-2})$ in the start of point (A) but at the end (point (B)) it has a same horizontal line in $h_{\text{exp}} (i \geq 45 \text{ mA cm}^{-2}) \approx 0.003 \text{ k}\Omega \text{ cm}^2$.

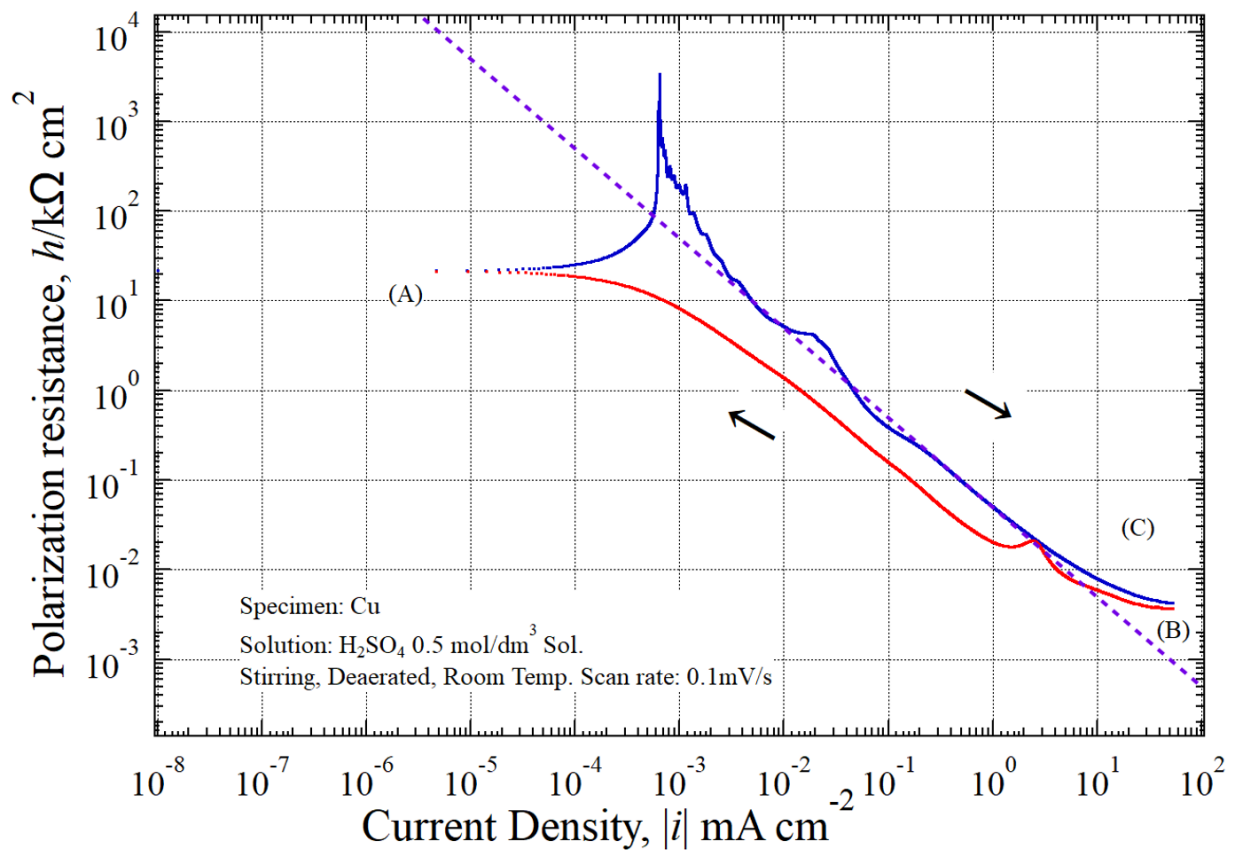


Figure 3.6 Polarization resistance curve of the copper electrode in 0.5 mol dm^{-3} H_2SO_4 solution, deaerated with H_2 gas bubbling, stirring, in room temperature and only in cathode and anode condition (1 Cycle)

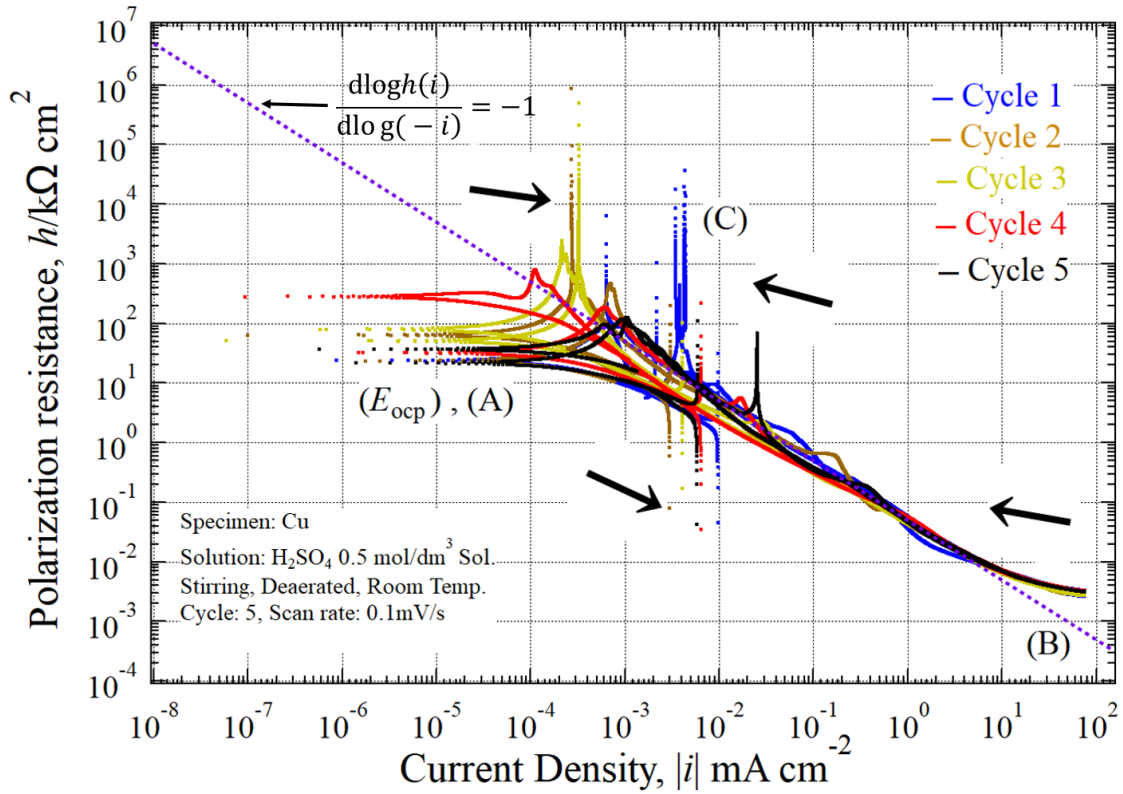


Figure 3.7 Polarization curve of the copper electrode in $0.5 \text{ mol dm}^{-3} \text{ H}_2\text{SO}_4$ solution, deaerated with H_2 gas bubbling, stirring, in room temperature and only in 5 Cycle

3.4. Discussion

3.4.1. Reaction on Copper Electrode

The value of $E(i)_{\text{exp}}$ in figure 3.4 and figure 3.5 were added to the E -pH diagram in figure 3.8. The green line is for $E(i)_{\text{exp}}$ -pH value for the 1 cycle measurement, the black line is for $E(i)_{\text{exp}}$ -pH value for the 5 cycle measurement. Since the second condition is 5 cycles measurement condition, equation 3.1 and 3.2 show the hybrid electrode system consists of two different single electrode reactions Red_1/Ox_1 and Red_2/Ox_2



The i is the net current density that flows through the hybrid electrode system which is the sum of i_1 and i_2 of its cathodic and anodic reaction. In other words, it can be described as:

$$i = i_1 + i_2 = i_{a1} + i_{c1} + i_{a2} + i_{c2} \quad (3.3)$$

Since the experiments that were measured cathode condition around (0.2 V vs. SHE to around -0.8 V vs. SHE), the pH solution of H₂SO₄ was around 0.3 (strong Acid), and DO was < 0.4 ppm. the possible reactions are:



By Assuming $[\text{Cu}^{2+}]_{\text{bulk}} \approx 10^{-6} \text{ mol.dm}^{-3}$ and $[\text{H}_2]_{\text{bulk}} \approx 10^{-3} \text{ mol.dm}^{-3}$ [24], E_{eq1} in equation (3.4) is -0.0018V and E_{eq2} in equation (3.5) is -0.16V. Therefore, the current density can be expressed as:

$$i_{\text{H}} = i_{\text{a,H}} + i_{\text{c,H}} \quad (3.6)$$

$$i_{\text{Cu}} = i_{\text{a,Cu}} + i_{\text{c,Cu}} \quad (3.7)$$

As expressed in equation (3.3), (3.6), and (3.7), the current density of the whole system can be expressed as:

$$i = i_{\text{H}} + i_{\text{Cu}} = i_{\text{a,H}} + i_{\text{c,H}} + i_{\text{a,Cu}} + i_{\text{c,Cu}} \quad (3.8)$$

Since the value of $i_{\text{c,Cu}}$ is depends on the concentration of Cu^{2+} , but its value is considered to be very small. Therefore, in this cathodic polarization state, the hydrogen generation is considered to occur most in the whole reaction system.

$$i = i_{\text{H}} + i_{\text{Cu}} \approx i_{\text{c,H}} \quad (3.9)$$

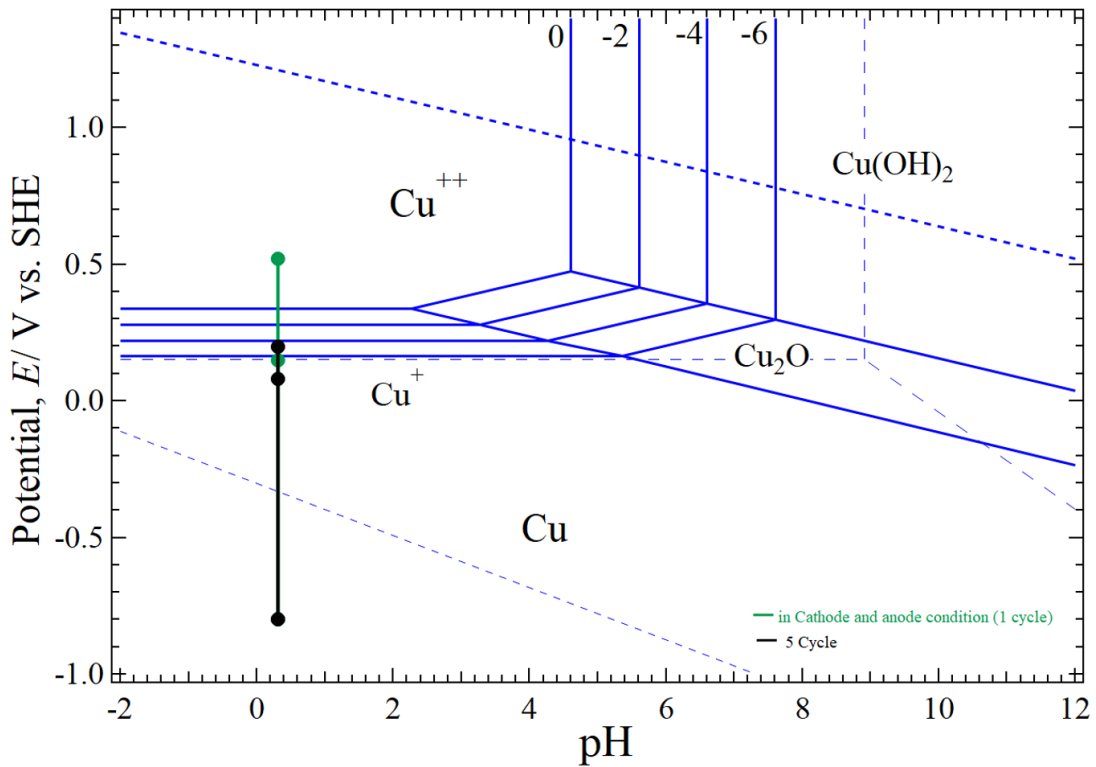


Figure 3.8 E -pH equilibrium diagram for the system copper-water at 25°C, that considering to Cu, Cu₂O and CuO and unconsidering to Cu(OH)₂

3.4.2. Proposed the Differential Polarization Method (DPM)

The differential polarization method (DPM) is established from electrochemical kinetics and it has relation. The explanation of DPM start from a single electrode reaction in equation 3.10 which characterized by Nernst's equation.



In this reaction, The potential in the equilibrium state (E_{eq}) of this reaction is expressed by the following Nernst's equation.

$$E_{\text{eq}} = E^0 + \frac{R}{z} \frac{T}{F} \ln \frac{\{\text{Ox}^{z+}\}_{\text{bulk}}}{\{\text{Red}\}_{\text{bulk}}} = E^0 + \frac{R}{z} \frac{T}{F} \ln \frac{y_{\text{Ox}^{z+}} [\text{Ox}^{z+}]_{\text{bulk}}}{y_{\text{Red}} [\text{Red}]_{\text{bulk}}}$$

$$\begin{aligned}
&= E^0 + \frac{R}{z} \frac{T}{F} \ln \frac{y_{\text{Ox}^{z+}}}{y_{\text{Red}}} + \frac{R}{z} \frac{T}{F} \ln \frac{[\text{Ox}^{z+}]_{\text{bulk}}}{[\text{Red}]_{\text{bulk}}} \\
&= E^{\phi} + \frac{R}{z} \frac{T}{F} \ln \frac{[\text{Ox}^{z+}]_{\text{bulk}}}{[\text{Red}]_{\text{bulk}}} \tag{3.11}
\end{aligned}$$

Overvoltage (η) is the differences between the applied potential (E) and the equilibrium potential (E_{eq}) that is eternally applied to the system. The potential-current curve or polarization curve presents the functional relationship of the current density i and overvoltage η . The functional relation $i(\eta)$ of this curve essentially involves two phenomena, which are (1) the charge process (Eq. 3) and the diffusion transfer process (Eq. 3.13-3.14).

The charge transfer process:

$$i(\eta) = i_0 \left\{ \left(\frac{[\text{Red}]_{\text{el}}}{[\text{Red}]_{\text{bulk}}} \right) \exp(f_a \eta) - \left(\frac{[\text{Ox}^{z+}]_{\text{el}}}{[\text{Ox}^{z+}]_{\text{bulk}}} \right) \exp(-f_c \eta) \right\} \tag{3.12}$$

The diffusion transfer process:

$$\left\{ \begin{aligned} \frac{[\text{Red}]_{\text{el}}}{[\text{Red}]_{\text{bulk}}} &= 1 - \frac{i}{i_{\text{Red,L}}} \end{aligned} \right. \tag{3.13}$$

$$\left\{ \begin{aligned} \frac{[\text{Ox}^{z+}]_{\text{el}}}{[\text{Ox}^{z+}]_{\text{bulk}}} &= 1 - \frac{i}{i_{\text{Ox}^{z+},\text{L}}} \end{aligned} \right. \tag{3.14}$$

When the charge process and the diffusion transfer process occur concurrently and steadily. The Eq 3.12-3.14 become:

$$i(\eta) = i_0 \left\{ \left(1 - \frac{i}{i_{\text{Red,L}}} \right) \exp(f_a \eta) - \left(1 - \frac{i}{i_{\text{Ox}^{z+},\text{L}}} \right) \exp(-f_c \eta) \right\} \tag{3.15}$$

Arranging the above equation become:

$$i(\eta) = \frac{\exp(f_a \eta) - \exp(-f_c \eta)}{\frac{1}{i_0} + \frac{\exp(f_a \eta)}{i_{\text{Red,L}}} + \frac{\exp(-f_c \eta)}{i_{\text{Ox}^{z+},\text{L}}}} = i_a(\eta) + i_c(\eta) \tag{3.16}$$

However,

$$i_a(\eta) = \frac{\exp(f_a \eta)}{\frac{1}{i_0} + \frac{\exp(f_a \eta)}{i_{\text{Red,L}}} + \frac{\exp(-f_c \eta)}{i_{\text{Ox}^{z+},\text{L}}}} (> 0) \tag{3.17}$$

$$i_c(\eta) = \frac{-\exp(-f_c \eta)}{\frac{1}{i_0} + \frac{\exp(f_a \eta)}{i_{\text{Red,L}}} + \frac{\exp(-f_c \eta)}{i_{\text{Ox}^{z+},\text{L}}}} \quad (< 0) \quad (3.18)$$

The polarization conductance, $g(\eta)$ is established by differentiated Eq. 3.16 which is expressed

$$\begin{aligned} g(\eta) &= \frac{di(\eta)}{d\eta} \\ &= \left((f_a \exp(f_a \eta) + f_c \exp(-f_c \eta)) \cdot \left(\frac{1}{i_0} + \frac{\exp(f_a \eta)}{i_{\text{Red,L}}} + \frac{\exp(-f_c \eta)}{-i_{\text{Ox}^{z+},\text{L}}} \right) \right) - \\ &= \frac{\left(\frac{f_a \exp(f_a \eta)}{i_{\text{Red,L}}} + \frac{f_c \exp(-f_c \eta)}{-i_{\text{Ox}^{z+},\text{L}}} \right) \cdot (\exp(f_a \eta) - \exp(-f_c \eta))}{\left(\frac{1}{i_0} + \frac{\exp(f_a \eta)}{i_{\text{Red,L}}} + \frac{\exp(-f_c \eta)}{-i_{\text{Ox}^{z+},\text{L}}} \right)^2} \\ &= \frac{(f_a \exp(f_a \eta) + f_c \exp(-f_c \eta))}{\frac{1}{i_0} + \frac{\exp(f_a \eta)}{i_{\text{Red,L}}} + \frac{\exp(-f_c \eta)}{-i_{\text{Ox}^{z+},\text{L}}}} \quad (3.19) \\ &= \frac{\left(\frac{f_a \exp(f_a \eta)}{i_{\text{Red,L}}} - \frac{f_c \exp(-f_c \eta)}{-i_{\text{Ox}^{z+},\text{L}}} \right) (\exp(f_a \eta) - \exp(-f_c \eta))}{\left(\frac{1}{i_0} + \frac{\exp(f_a \eta)}{i_{\text{Red,L}}} + \frac{\exp(-f_c \eta)}{-i_{\text{Ox}^{z+},\text{L}}} \right)^2} \end{aligned}$$

Arranging equation (3.17) and (3.18) to equation (3.19);

$$\begin{aligned} g(\eta) &= f_a i_a(\eta) - f_c i_c(\eta) \\ &= \left(\frac{(\exp(f_a \eta) - \exp(-f_c \eta))}{\frac{1}{i_0} + \frac{\exp(f_a \eta)}{i_{\text{Red,L}}} + \frac{\exp(-f_c \eta)}{-i_{\text{Ox}^{z+},\text{L}}}} \cdot \frac{\left(\frac{f_a \exp(f_a \eta)}{i_{\text{Red,L}}} - \frac{f_c \exp(-f_c \eta)}{i_{\text{Ox}^{z+},\text{L}}} \right)}{\frac{1}{i_0} + \frac{\exp(f_a \eta)}{i_{\text{Red,L}}} + \frac{\exp(-f_c \eta)}{-i_{\text{Ox}^{z+},\text{L}}}} \right) \\ g(\eta) &= f_a i_a(\eta) - f_c i_c(\eta) \quad (3.20) \\ &= i(\eta) \left(\frac{f_a}{i_{\text{Red,L}}} i_a(\eta) + \frac{f_c}{-i_{\text{Ox}^{z+},\text{L}}} i_c(\eta) \right) \end{aligned}$$

The net current density will roughly equal to the cathodic currents density value when being further polarized ($\eta \ll 0$).

$$i(\eta) \approx i_c(\eta) \quad (3.21)$$

Therefore, equation (3.20) can be clarified to:

$$g(\eta) = -f_c i_c(\eta) - i(\eta) \frac{f_c}{-i_{Ox^{z+},L}} i_c(\eta) = -f_c i(\eta) \left(1 + \frac{i(\eta)}{-i_{Ox^{z+},L}} \right) \quad (3.22)$$

Since the value of over potential is ($\eta = E - E_{eq}$), the polarization resistance is $h(i) =$

$\frac{dE}{di}$, and the mathematical relation to $g(\eta)$ can be:

$$\frac{di}{d\eta} \frac{d\eta}{di} = g(\eta) \frac{d(E - E_{eq})}{di} = g(\eta) \cdot h(i) = 1 \quad (3.23)$$

Arranging equation (3.22) and (3.23) be:

$$h(i) = \frac{1}{g(\eta)} = \frac{1}{-f_c i(\eta) \left(1 + \frac{i(\eta)}{-i_{Ox^{z+},L}} \right)} = \frac{RT}{\alpha_c nF} \left(\frac{1}{1 + \frac{i(\eta)}{-i_{Ox^{z+},L}}} \right) \left(\frac{1}{-i} \right) \quad (3.24)$$

When the value of $\frac{i(\eta)}{-i_{Ox^{z+},L}} \approx 0$, the equation (3.24) becomes:

$$h(i) = \frac{RT}{\alpha_c nF} \left(\frac{1}{-i} \right) \quad (3.25)$$

Logarithms of equation (3.25) is:

$$\log h(i) = \log \frac{RT}{\alpha_c nF} - \log(-i) \quad (3.26)$$

The gradient of equation (3.26) is:

$$\frac{d \log h(i)}{d \log(-i)} = -1 \quad (3.27)$$

TEM ($\eta = a + b \log |i|$) [10] in the cathodic polarized state is valid in the relation to the equation (3.27) as shown as:

$$\eta = a + b \log |i| = a + \frac{b}{2.3} \ln(-i) \quad (3.28)$$

The $h(i)$ expression for the tafel equation is obtained by differentiating equation (3.25):

$$h(i) = \frac{-b}{2.3} \left(\frac{1}{-i} \right) \quad (3.29)$$

From equation (3.29) will be obtained to the equation (3.27) by taking the logarithm and gradient of equation (3.29). The $E(i)$ area of equation (3.27) is included in the $E(i)$ area of equation (3.28) in both ways. Therefore, equation (3.27) is suitable in the calculation of tafel slope region in the experimental data.

3.4.3. Estimation of i_0 on Copper Electrode by Using TEM

There are 3 considering rule in applying the TEM:

- (1) The linearity of $\eta = a + b \log |i|$ should be extend over at least one order magnitude of $|i|$
- (2) The extrapolation should start at $|\eta| \geq 0.12$ V
- (3) Avoid high current areas as the effects of iR resistance and hydrogen bubbles.

The satisfy range due to the above rule can be found in Figure 3.4 Figure 3.5. The TEM area for i_0 estimation of Figure 3.4 is shown in Figure 3.9. The TEM area is $0.03 \text{ mA cm}^{-2} \leq |i| \leq 1 \text{ mA cm}^{-2}$ in cathode measurement. The Tafel equation for this measurement is shown in equation 3.30. From this Tafel equation, the i_0 for the measurement is $10^{-2.7} \text{ mA cm}^{-2}$ (equation 3.31). However, these result was far from the result that had published before $i_0 = 10^{-5.6}$ to $10^{-2.9} \text{ mA.cm}^{-2}$ [13].

$$\eta = -0.42 - 0.17 \log |i| \quad (3.30)$$

$$i_0 = 10^{-(0.46/0.17)} = 10^{-2.7} \text{ mA cm}^{-2} \quad (3.31)$$

The TEM area for i_0 estimation of Figure 3.5 is shown in Figure 3.10. Since the trend of cycles the paths show almost the same trend. The TEM calculation is only uses the backward routes of cycle 3 and cycle 4 in the same range of $|i|$ as shown in equation 3.32 and equation 3.33:

$$\text{Cycle 3} \quad 0.2 \text{ mA cm}^{-2} \leq |i| \leq 4 \text{ mA cm}^{-2} ; \eta = -0.28 - 0.27 \log |i| \quad (3.32)$$

$$\text{Cycle 4} \quad 0.3 \text{ mA cm}^{-2} \leq |i| \leq 3 \text{ mA cm}^{-2} ; \eta = -0.24 - 0.22 \log |i| \quad (3.33)$$

However, equation 3.34 and 3.35 show the result of i_0 in cycle 3 and cycle 4, respectively

$$\text{Cycle 3} \quad i_0 = 10^{-(0.28/0.27)} = 10^{-1.03} \text{ mA cm}^{-2} \quad (3.34)$$

$$\text{Cycle 4} \quad i_0 = 10^{-(0.24/0.22)} = 10^{-1.09} \text{ mA cm}^{-2} \quad (3.35)$$

However, these results were far from the result that had published before $i_0 = 10^{-5.6}$ to $10^{-2.9} \text{ mA.cm}^{-2}$ [13]. This condition is often pointed out as the problem when applying the TEM [27].

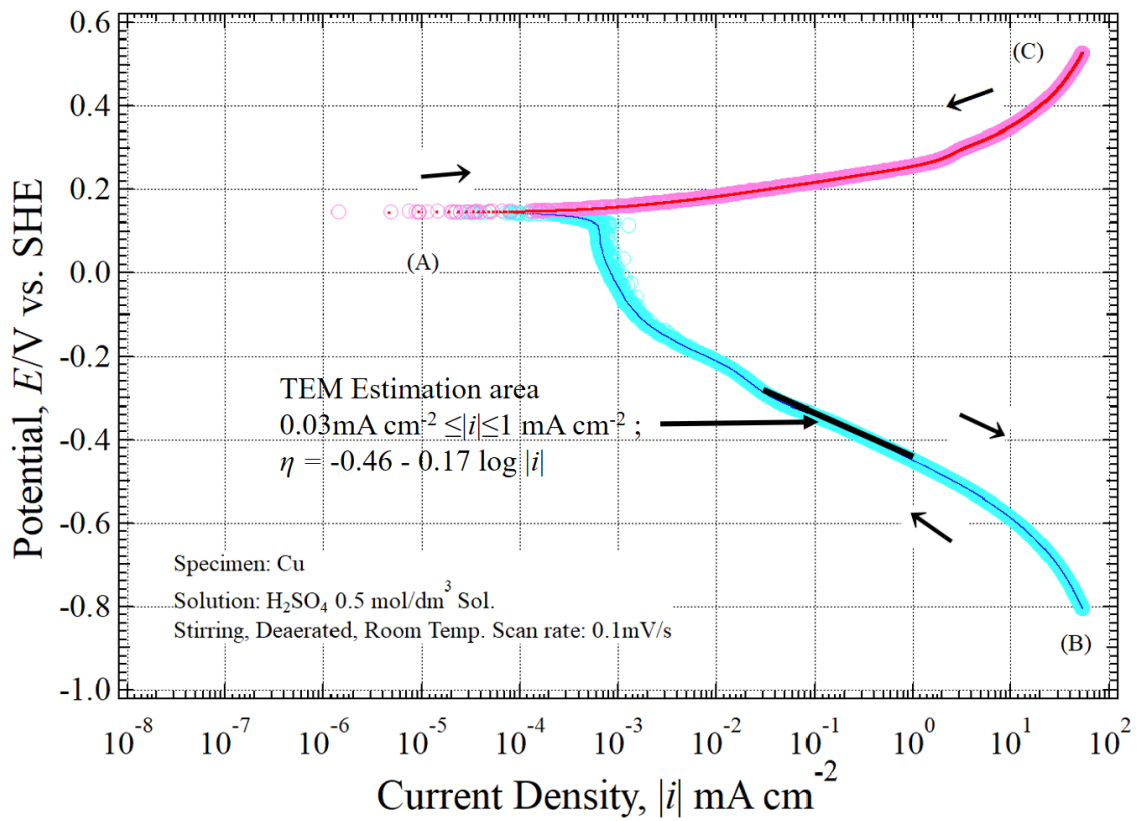


Figure 3.9 The TEM area for i_0 estimation of Figure 3.4

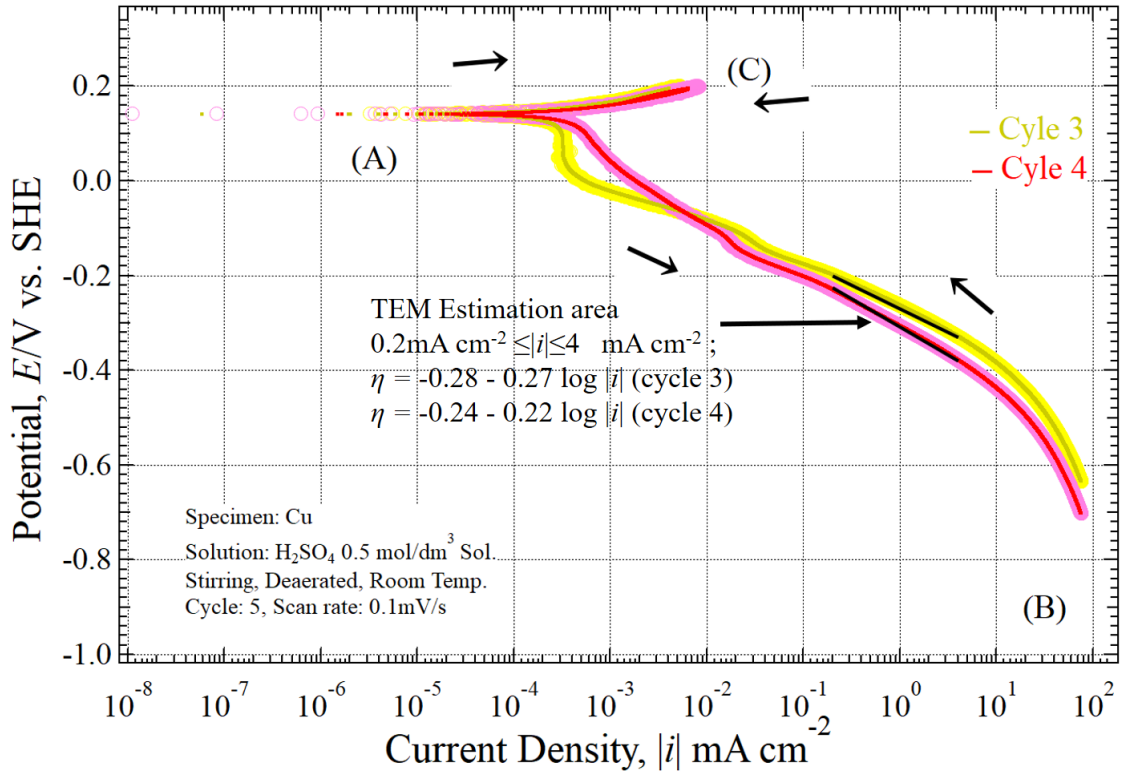


Figure 3.10 The TEM area for i_0 estimation of Figure 3.5

3.4.4. Estimation of i_0 on Copper Electrode by Using DPM

In order to compare both, It is necessary to calculate the $i_{H^+,L}$. Theoretically, the $i_{H^+,L} \rightarrow \infty$ is assumed. The $i_{H^+,L}$ can be calculate using formula in equation

$$i_{H^+,L} = -z F k_{H^+} [H^+]_{\text{bulk}} = -z F \frac{D_{H^+}}{\delta} [H^+]_{\text{bulk}} \quad (3.36)$$

δ is assumed to 0.03cm and the number of z is 1 or 2. However, equation (3.36) become:

$$\begin{aligned} i_{H^+,L} &= -z F k_{H^+} [H^+]_{\text{bulk}} = -z F \frac{D_{H^+}}{\delta} [H^+]_{\text{bulk}} \\ &= -(1\sim 2)(96.5 \\ &\times 10^3 \text{ A s mol}^{-1}) \left(\frac{7 \times 10^{-5} \text{ cm s}^{-2}}{0.03 \text{ cm}} \right) (10^{-3} \text{ mol dm}^{-3}) \\ &\approx -225 \sim -450 \text{ mA cm}^{-2} \end{aligned} \quad (3.37)[24,26]$$

The value of $|i_{H^+,L}| \approx -225 \sim -450 \text{ mA cm}^{-2}$ is over scaled and it is presumed that $h(i_{H^+,L})$ could not be observed. If the measurement range is expanded to $|i| \approx 10^3 \text{ mA cm}^{-2}$, the electrode surface becomes unstable due to radical hydrogen generation, and the measurement data becomes unstable.

In this dissertation by using the DPM, the consideration of removing physical factor oxide film and solution polarization resistance that commonly include in the result of $E_{\text{exp}}(i)$ and $h_{\text{exp}}(i)$ is included rationally.

The oxide film polarization resistance (l_c/k_c) of the cathodic site is arranged to the equation (3.25), be:

$$h(i) = \frac{RT}{\alpha_c z F} \left(\frac{1}{-i} \right) + \frac{l_c}{\kappa_c} \quad (3.38)$$

The solution polarization resistance (l_s/k_s) is always contained in the $h_{\text{exp}}(i)$, as :

$$h_{\text{exp}}(i) = h(i) + \frac{l_s}{\kappa_s} = \left\{ \frac{RT}{\alpha_c z F} \left(\frac{1}{-i} \right) + \frac{l_c}{\kappa_c} \right\} + \frac{l_s}{\kappa_s}$$

$$h_{\text{exp}}(i) = h(i) + \frac{l_s}{\kappa_s} = \left\{ \frac{RT}{\alpha_c z F} \left(\frac{1}{-i} + \frac{1}{i - i_{O_{x^+,L}}} \right) \right\} + \frac{l}{\kappa} \quad (\text{since; } \frac{l}{\kappa} = \frac{l_c}{\kappa_c} + \frac{l_s}{\kappa_s}) \quad (3.39)$$

For the DPM the $|i|$ range is $0.2 \text{ mA cm}^{-2} \leq |i| \leq 2 \text{ mA cm}^{-2}$ for 1 cycle measurement, and $0.3 \text{ mA cm}^{-2} \leq |i| \leq 3 \text{ mA cm}^{-2}$ for 5 cycle measurement. If $\alpha_c z$ is 0.55 for 1 cycle measurement and 0.58 for 5 cycles measurement (be explained later), equation 3.40 and equation 3.41 can show the value of $\frac{RT}{\alpha_c z F} \left(\frac{1}{i - i_{O_{x^+,L}}} \right)$ of 1 cycle measurement and 5 cycles measurement:

$$\frac{0.026}{\alpha_c z} \left(\frac{1}{i - i_{O_{x^+,L}}} \right) = \frac{0.026}{0.55} \left(\frac{1}{-0.2 \sim -2 \text{ mA cm}^{-2} + 225 \sim 450 \text{ mA cm}^{-2}} \right)$$

$$= 0.0001 \sim 0.0002 \text{ k}\Omega\text{cm}^2 \quad (3.40)$$

$$\frac{0.026}{\alpha_c z} \left(\frac{1}{i - i_{O_{x^+,L}}} \right) = \frac{0.026}{0.58} \left(\frac{1}{-0.3 \sim -3 \text{ mA cm}^{-2} + 225 \sim 450 \text{ mA cm}^{-2}} \right)$$

$$= 0.0001 \sim 0.0002 \text{ k}\Omega\text{cm}^2 \quad (3.41)$$

Seri O [17] reported that large increasing value of $|i|$ make the l/κ be a horizontal line. In Figure 3.6 and Figure 3.7, the horizontal line of polarization resistance graph can be found in $0.004 \text{ k}\Omega\text{cm}^2$ and in $0.003 \text{ k}\Omega\text{cm}^2$, respectively. Therefore, $l/\kappa \approx 0.004 \text{ k}\Omega\text{cm}^2$ for 1 cycle and $l/\kappa \approx 0.004 \text{ k}\Omega\text{cm}^2$ for 5 cycles. In other value, $\frac{0.026}{\alpha_c z} \left(\frac{1}{i - i_{\text{Ox}z+,L}} \right) = 0.0001 \sim 0.0002 \text{ k}\Omega\text{cm}^2 \approx 0 \text{ k}\Omega\text{cm}^2$. Therefore, equation 3.38 of cycle 1 can be shown in equation 3.42 and equation 3.43 for the 5 cycles:

$$\begin{aligned} h_{\text{exp}}(i) &= \frac{RT}{\alpha_c z F} \left(\frac{1}{-i} + \frac{1}{i - i_{\text{Ox}z+,L}} \right) + \frac{l}{\kappa} \approx \frac{RT}{\alpha_c z F} \left(\frac{1}{-i} \right) + \frac{l}{\kappa} \\ &= \frac{RT}{\alpha_c z F} \left(\frac{1}{-i} \right) + 0.004 \end{aligned} \quad (3.42)$$

$$\begin{aligned} h_{\text{exp}}(i) &= \frac{RT}{\alpha_c z F} \left(\frac{1}{-i} + \frac{1}{i - i_{\text{Ox}z+,L}} \right) + \frac{l}{\kappa} \approx \frac{RT}{\alpha_c z F} \left(\frac{1}{-i} \right) + \frac{l}{\kappa} \\ &= \frac{RT}{\alpha_c z F} \left(\frac{1}{-i} \right) + 0.003 \end{aligned} \quad (3.43)$$

The relation of $h_{\text{exp}}(i) - 0.004$ and i in 1 cycle are plotted in Figure 3.11 and relation of $h_{\text{exp}}(i) - 0.004$ and i in 5 cycles are plotted in Figure 3.12. For the measurement in 1 cycle, when equation 3.42 is applied, the range of $0.2 \text{ mA cm}^{-2} \leq |i| \leq 2 \text{ mA cm}^{-2}$ is coincided with the line of equation 3.27 and can be considered to calculate i_0 by using the TEM. For the measurement in 5 cycles, when equation 3.43 is applied, the forward and backward route of all cycle have the same route in the range of $0.3 \text{ mA cm}^{-2} \leq |i| \leq 3 \text{ mA cm}^{-2}$ and coincide with the line of equation 3.27.

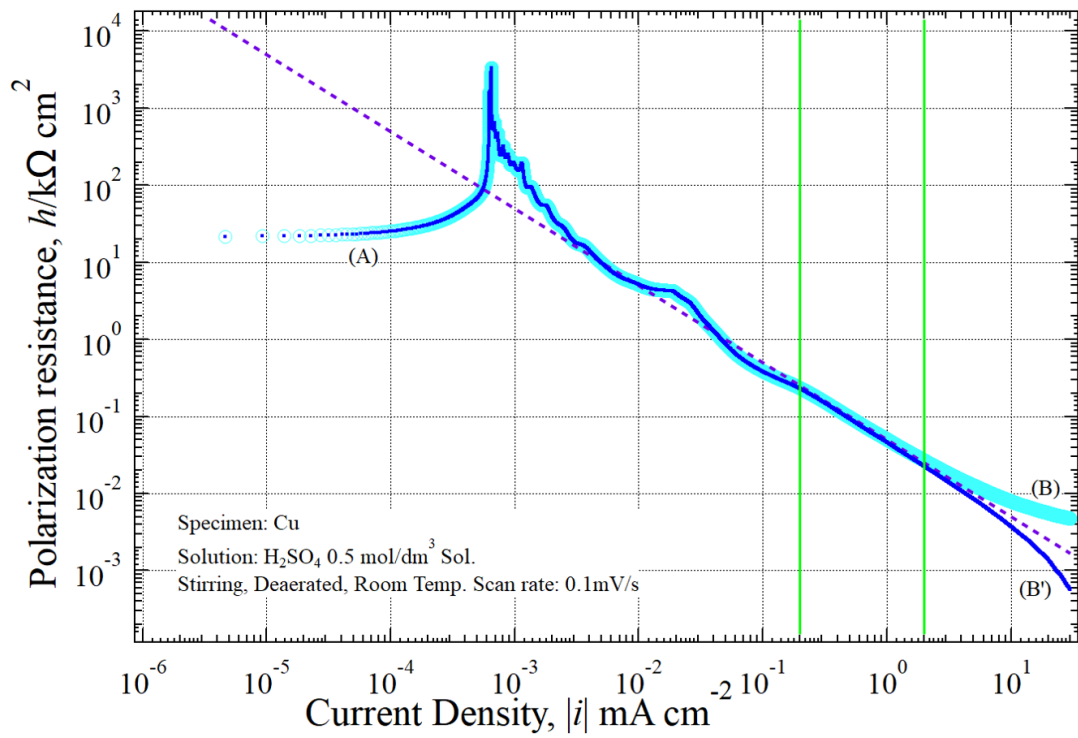


Figure 3.11 Polarization resistance data (Original curve) plots (light blue circle) and its revised plot $\{h_{\text{exp}}(i)-0.004\}$ (dark blue). A green vertical lines ($|i|=0.2 \text{ mAcm}^{-2}$ and 2 mAcm^{-2}) are added which satisfied the tafel slope. And the purple dashed line is added as the tafel slope.

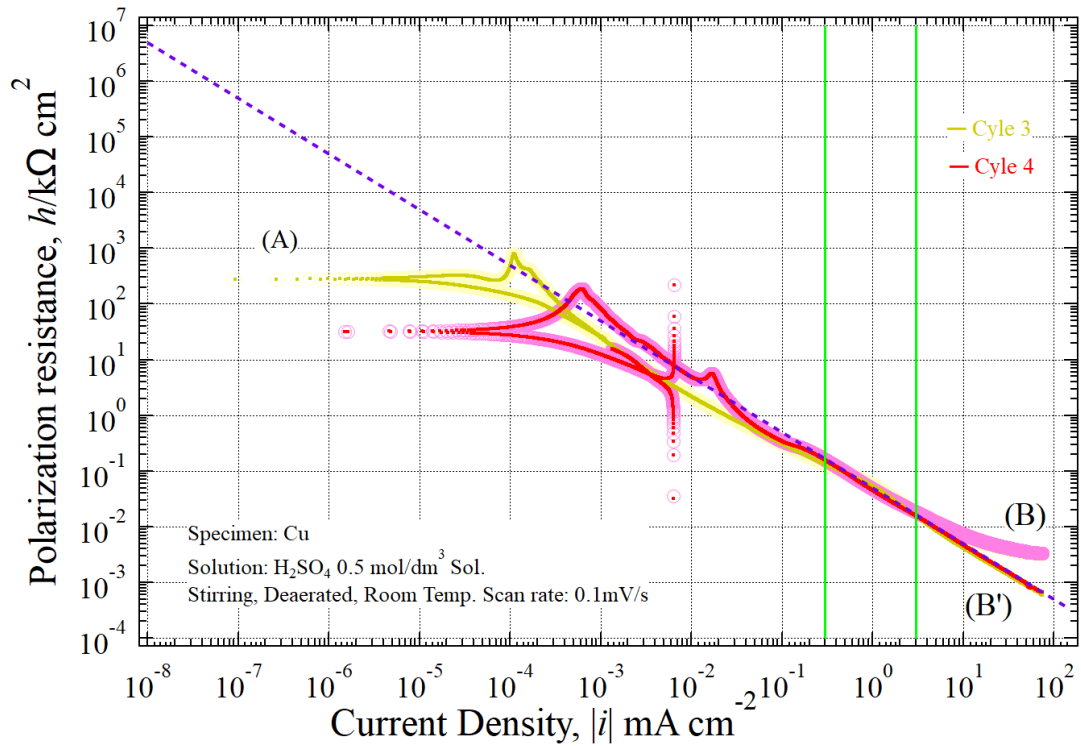


Figure 3.12 Polarization resistance data (Original curve) plots (light color circle) and its revised plot $\{h_{\text{exp}}(i)-0.003\}$ (dark color). A green vertical lines ($|i|=0.3$ mAcm⁻² and 3 mAcm⁻²) are added which satisfied the tafel slope. And the purple dashed line is added as the tafel slope.

The above paragraph was mentioned that the $\alpha_c z$ is 0.55 for 1 cycle measurement and 0.58 for 5 cycles measurement. However, the following constraints were used between α_c and z in determining α_c :

- The range of α_c is in range of $0 < \alpha_c < 1$
- z indicating the number of mobile charges is natural number (1,2,3,...)

Therefore, from equation 3.40 and 3.41, α_c can be calculated by using the experimental data and assuming $z=1$. The equation 3.44 shows the formula of α_c for 1 cycle and

equation 3.45 show the formula of α_c for 5 cycles:

$$\alpha_c = \frac{RT}{zF} \left(\frac{1}{-i} \right) \left(\frac{1}{h_{\text{exp}}(i) - 0.004} \right) = \frac{0.026}{(h_{\text{exp}}(i) - 0.004) (-i)} \quad (3.44)$$

$$\alpha_c = \frac{RT}{zF} \left(\frac{1}{-i} \right) \left(\frac{1}{h_{\text{exp}}(i) - 0.003} \right) = \frac{0.026}{(h_{\text{exp}}(i) - 0.003) (-i)} \quad (3.45)$$

The results of α_c are shown as a red circle line in figure 3.13 and 3.14, respectively for 1 cycle measurement in area ($|i|=0.2 \text{ mAcm}^{-2}$ and 2 mAcm^{-2}) and 5 cycle measurement ($|i|=0.3 \text{ mAcm}^{-2}$ and 3 mAcm^{-2}). The value of $\alpha_c=0.55$ and $z = 1$ are qualified for the above constraints for 1 cycle measurement and $\alpha_c=0.58$ and $z = 1$. Since the result of α_c is 0.55, the equation 3.4 can be mentioned as an irreversible reaction [17,18] and $z = 1$ means that a rate-limiting reaction of one electron is involved. Therefore, the *HER* that occurs on the surface of Cu is limited to the chemical species whose oxidation number changes from 1 to 0, and H^+ and H^0 can be considered. If H^0 of the reductant is of adsorbed hydrogen, the rate –limiting reaction of this system is as well-known as:



Under the initial condition ($-i_0, E_{\text{eq1}} = -0.018 \text{ V}$), Equation 3.42 and Equation 3.43 can be used to solve the i_0 of the 1 cycle measurement and 5 cycles measurement. Respectively. Therefore, equation 3.47 is the calculation of the i_0 of the 1 cycle measurement and equation 3.48 for 5 cycles measurement

$$\int_{E_{\text{exp}}(i)}^{-0.018} dE_{\text{exp}}(i) = \int_i^{-i_0} h_{\text{exp}}(i) d i = \int_i^{-i_0} \left\{ \frac{0.026}{0.55} \left(\frac{1}{-i} \right) + 0.004 \right\} d i$$

$$E_{\text{exp}}(i) = -0.018 + 0.047 \ln \frac{i_0}{-i} - 0.004 (i + i_0) \quad (3.47)$$

$$\int_{E_{\text{exp}}(i)}^{-0.018} dE_{\text{exp}}(i) = \int_i^{-i_0} h_{\text{exp}}(i) d i = \int_i^{-i_0} \left\{ \frac{0.026}{0.58} \left(\frac{1}{-i} \right) + 0.003 \right\} d i$$

$$E_{\text{exp}}(i) = -0.018 + 0.044 \ln \frac{i_0}{-i} - 0.003 (i + i_0) \quad (3.48)$$

The i_0 usually has small value in equation (3.11). Therefore, it can be approximated that

$i+i_0 = i$. Then,

$$E_{exp}(i) = -0.018 + 0.047 \ln \frac{i_0}{-i} - 0.004 i \quad (3.49)$$

$$E_{exp}(i) = -0.018 + 0.044 \ln \frac{i_0}{-i} - 0.003 i \quad (3.50)$$

The plot result of the relationship between i_0 and i from equation (3.49) are added to the Figure 3.14 (blue circle line) and i_0 and i from equation (3.50) are added to the Figure 3.15 (blue circle line). The results of both condition show that i_0 is around 10^{-5} mA cm⁻² for 1 cycle and 10^{-3} mA cm⁻² for 5 cycles. These results are in the range of **10^{-5.6} to 10^{-2.9}** mA.cm⁻². [13]..

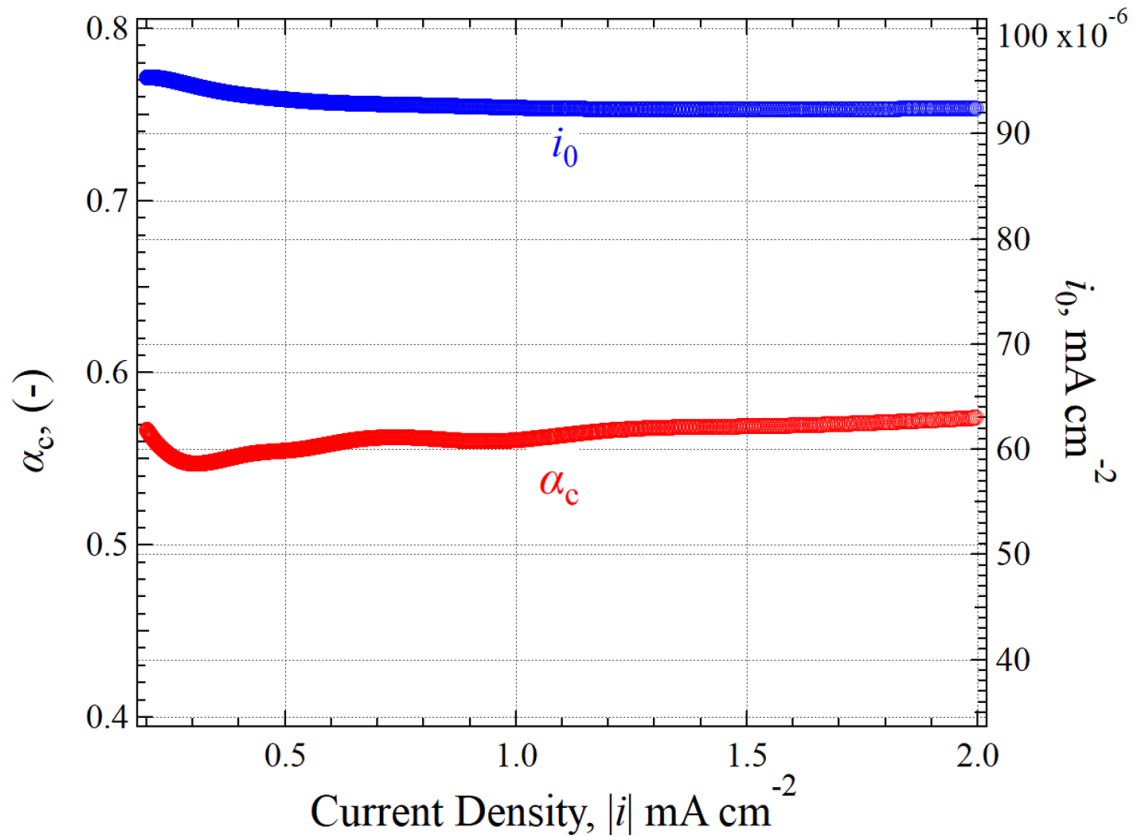


Figure 3.13 The result of α_c (red line) and i_0 (blue line) in range of estimated area for 1 cycle measurement ($|i|=0.2$ mAcm⁻² and 2 mAcm⁻²)

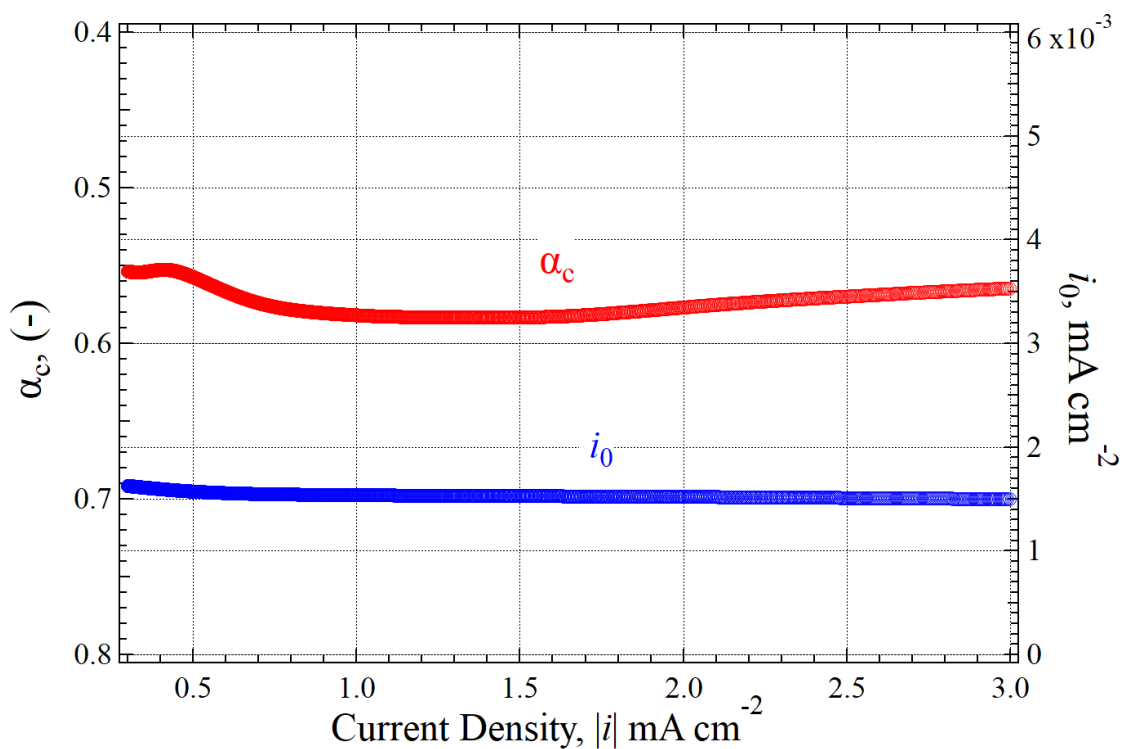


Figure 3.14 The result of α_c (red line) and i_0 (blue line) in range of estimated area for 5 cycles measurement ($0.3 \text{ mAcm}^{-2} \leq |i| \leq 3 \text{ mAcm}^{-2}$)

3.5 Conclusion

The measurement of i_0 of copper electrode by $0.5 \text{ mol dm}^{-3} \text{ H}_2\text{SO}_4$ solution in 1 cycle and 5 cycle measurement by using Tafel extrapolation method show the far results from published before $i_0 = 10^{-5.6}$ to $10^{-2.9} \text{ mA.cm}^{-2}$. However, the differential polarization method (DPM), the new proposed method, show that The results of i_0 in both condition are around $10^{-5} \text{ mA cm}^{-2}$ for 1 cycle and $10^{-3} \text{ mA cm}^{-2}$ for 5 cycles. These results are in the range of $10^{-5.6}$ to $10^{-2.9} \text{ mA.cm}^{-2}$. In addition, DPM also can be used to estimate the value of α_c . It is demonstrated that the proposed technique has advantages: (1) accurate finding of the Tafel slope region and (2) easy removing of physical resistances such as oxide film and solution resistance.

Reference

1. E. Gileadi: Physical Electrochemistry, (WILEY-VCH, Weinheim, 2011) pp. 329-362.
2. C. Hitz and A. Lasia: J. Electroanal. Chem. 532 (2002) 133-140.
3. S. Chen and A. Kucernak: J. Phys. Chem. 108 (2004) 13984 -13994.
4. Du, J.; Wang, J.; Ji, I.; Xu, X.; Chen, Z. A highly active and robust copper-based electro catalyst toward hydrogen evolution reaction with low over potential in neutral solution. ACS Applied Material & Interfaces, 8 (2016), pp 30205-30211.
5. Vaduva, C. C.; Naszilcsin, N.; Kellenberger, A.; Medeleanu, M. Catalytic enhancement of hydrogen evolution reaction on copper in the presence of benzylamine. International Journal of hydrogen Energy 36 (2011), pp 6994-7001.
6. Raoof, J .B.; Ojani, R.; KIani, A.; Nadimi, S.R. Fabrication of highly porous Pt coated nanostructured Cu-foam modified copper electrode and its enhanced catalytic ability for hydrogen evolution reaction. International Journal of hydrogen Energy 35 (2010), pp 452-458.
7. Lei, H.; Fang, H.; Han, Y.; Lai, W.; Fu, X.; Cao, R. Reactivity and Mechanism Studies of Hydrogen Evolution Catalyzed by Copper Corroles. ACS Catal. 2015, 5, 5145–5153.
8. N. Pentland, J.O.M. Bockris, E. Sheldon, Hydrogen evolution reaction on copper, gold, molybdenum, palladium, rhodium and iron. J Electrochem Soc, 104 (1957), pp. 182-194
9. Mckone, J. R.; Warren, E. L.; Bierman, M. J.; Boettcher, S. W.; Brunschwig, B. S.; Lewis, N. S.; Gray, H. B. Evaluation of Pt, Ni, and Ni-Mo Electro catalysts for Hydrogen Evolution on Crystalline Si Electrodes. Energy Environmental Science, 4

- (2011), pp. 3573–3583.
10. Tafel, J. Ueber die Polarisation bei Kathodischer Wasserstoffentwicklung. *Z.Physik. Chem.* 1905, 50A, 64–712.
 11. Vetter, K.J. *Electrochemical Kinetics*; Beckenstein, S.; Hoard, B., Translators; Academic Press: New York, NY, USA, 1967
 12. Bockris, J.O.M.; Reddy, A.K.N. *Modern Electrochemistry*; Plenum Press: New York, NY, USA, 1983; Volumes 1 and 2.
 13. Bard, A.J. (Ed.) *Hydrogen Encyclopedia of Electrochemistry of the Elements*; Marcel Dekker Inc.: New York, NY, USA, 1982; pp. 383–555.
 14. Kita, H. Periodic Variation of Exchange Current Density of Hydrogen Electrode Reaction with Atomic Number. *J. Res. Inst. Catalysis Hokkaido Univ.* 1965, 13, 151–168.
 15. Matsushima, T.; Enyo, M. Stoichiometric number and the mechanism of the hydrogen electrode reaction on noble metals in acidic solutions. *J. Res. Inst. Catalysis Hokkaido Univ.* 1969, 1, 14–27.
 16. Yoshizawa, S.; Watanabe, N. *Kyorittsu Zensho*. In *DenkKagaku I*; Kyoritsu Shuppan Co., Ltd.: Tokyo, Japan, 1980; p. 141.
 17. Seri, O.; Itoh, Y. Differentiating polarization curve technique for determining the exchange current density of hydrogen electrode reaction. *Electrochimica Acta* 2016, 218, 345–353.
 18. Seri, O. Differentiating approach to the tafel slope of hydrogen evolution reaction on nickel electrode. *Electrochemistry Communications* 2017, 81, 150–153.
 19. Bard, A.J.; Faulkner, L.R. *Electrochemical Methods*; John Wiley & Sons: New York, NY, USA, 1980; p. 102.

20. Gileadi, E. Physical Electrochemistry; Wiley-VCH Verlag GmbH & Co. KGaA: Weinheim, Germany, 2015; p. 77
21. Charlot, G.; Badoz-Lambling, J.; Tremillon, B. Les Reactions Electrochimiques; Maruzen Co. Ltd.: Tokyo, Japan, 1959.
22. Adams, R.N. Electrochemistry at Solid Electrodes; Marcel Dekker: New York, NY, USA, 1969.
23. V. Kreizer, I. K. Marshakov, N. M. Tutukina, and I. D. Zartsyn, The Effect of Oxygen on Copper Dissolution during Cathodic Polarization, Protection of Metals, Vol. 39, No. 1, 2003, pp. 30–33.
24. G. Charlot, J. Badoz-Lambling and B. Tremillon: Electrochemical Reactions, (Elsevier Publishing Co., Amsterdam-New York, 1962) pp. 46-116.
25. Adams, R.N. Electrochemistry at Solid Electrodes; Marcel Dekker: New York, NY, USA, 1969.
26. L. L. Shreir ed.: Corrosion, Vol. 1, (Newnes-Butterworths, London, 1978) 5:34-5:58.
27. N. Tanaka, R. Tamamushi, Kinetic parameters of electrode reactions, Electrochim. Acta 9 (1964) 963–989.

Chapter 4

Performance, Rate of Heat Release, and Combustion Stability of Dual-fuel Mode in a Small Diesel Engine

4.5 Introduction

A fast-growing number of population, industries and automobiles have consumed

massive stock from the limited remain stock of the fossil fuel. Hence, it causes the rapid increasing of atmosphere pollution which contributes to the global warming cause of greenhouse gases (GHG) emission from the engine. IPCC, 2014: Summary for policymakers reported that total anthropogenic CO₂ emission between 1750 and 2010 had tripled increased from 420±35 Giga ton CO₂ to 1300±110 Giga ton CO₂ [1]. This condition still increasing continuously due to the economic and population growth [2]. Therefore, many governments and researchers focus in reducing the GHG emission. Ministry of the Environment, Government of Japan reported that the total emissions were 1.322 Million tonnes of CO₂eq/year in 2016. This emission is decrease from 1.2 %, 7.3%, and 5.2% compared to those of 2015, 2013, 2005, respectively [3].

In industries and automobiles trend around these recent years, the comprehensive applicability of diesel engine as power source in transportation, industries and other needs have rapidly increased over past century. It may be due to the high thermal efficiency, excellent fuel economy and lower emission of unburned hydrocarbons (UHCs), carbon monoxide (CO), and carbon dioxide (CO₂) compared to the gasoline engine [4-6]. However, the pollutant emission exhaust of smoke, particulate matter (PM), and Nitrogen oxide (NO_x) of diesel engine is higher than the gasoline engines [7-8] which means pollutants from diesel engine potentially impact human health such as visibility, vocational carcinogen in human lung, influencing worst to the compromised lung function patients and have another negative impacts [9-10]. Therefore, Biofuels, such as: biodiesel fuel and biogas fuel, are the promising alternative energy source for diesel engine due to the resource availability, non-hazardous environment, economically, and engine efficiency.

Biodiesel fuel can be produced from vegetable oil or animal fat by transesterification

reaction, dilution, pyrolysis, and micro emulsification [11-12]. In addition, waste cooking oil is also considered to be used in biodiesel synthesis, which can decrease the competition with food demand [13]. Therefore, Biodiesel is one of the promising source energy that have a future of sustainability. Biodiesel has many advantages comparing to petroleum diesel: 1. It does not need engine modification or can be mixed with petroleum diesel [14,15]. 2. The combustion efficiency and ignition property of biodiesel are better than petroleum diesel due to its high cetane number [16]. 3. Carbon monoxide emission, smoke and particulate matter of biodiesel is less than petroleum diesel fuel [17-18]. 4. Biodiesel is non-toxicity, less sulfur and aromatic content and has high lubricity [19] which can decrease the wear of engine [20]. However, Biodiesel also has some disadvantages: 1. Biodiesel needs more amount of fuel compared to petroleum diesel in same power drive condition [21]. 2. Impurity of biodiesel can cause the corrosion in the diesel engine [22-23].

Biogas fuel is the other renewable resource energy that attracts many researchers to develop and apply in diesel engine. Generally, biogas is produced by anaerobic fermentation from the biological decomposition of organic matter such as biodegradable organic waste in landfill and agricultural. Table 4.1 shows the compositions of biogas from many resources [24]. The purification of biogas is important to remove the containing of hydrogen sulfide (H_2S) and water vapor that possible make corrosion [25]. In the application of biogas in diesel engine can reduce the pollutant emission [26]. However, biogas fuel can not be applied directly in diesel engine (CI Engine) as it can not work as start ignition automatically. It must be converted into spark ignition engine or in dual-fuel mode using diesel-biogas or biodiesel-biogas, which diesel or biodiesel performance as pilot fuel [27-28].

There are many researchers focused in the application of dual-fuel system in these recent years. K.Cacua et al. conducted an investigation to evaluate the effect of air enrich with oxygen on dual fuel engine using biogas as primary fuel [29]. M. Feroskhan et al. and A. Sarkar et al. reported the effect of charge preheating on the performance of dual fuel CI engine [30-31]. A. Yousefi et.al. reported that improving diesel injection timing decreases the unburned methane, which means higher thermal efficiency [32]. S. Verna et. al. conducted an experiment with various compression ratio (CR); 16.5 17.5, 18.5 and 19.5 with using exhaust gas recirculation (EGR) and found that higher CR improved the energy efficiency and EGR had positive effect to the engine [33]. H. Huang et. al compared the result of experiment and simulation using CFD software and confirmed that both result can be applied to the simulated practical diesel and natural gas in dual fuel engine mode [34]. Also, H. Huang et. al reported the effect of multiple injection on combustion in natural gas-diesel dual fuel mode engine [35].

Moreover, an interesting phenomena in brake thermal efficiency in dual-fuel mode diesel engine has been reported by Himsar A[36], and Nathan et. al[37]. Increasing the biogas energy ratio in diesel gradually, does not increase the brake thermal efficiency gradually. As a result, it will have a maximum condition of operation and fuel composition. This trend is an interesting phenomena that should be observed.

This research is focused on the study of diesel engine run in dual-fuel mode without substantial modification. The ROHR analysis will be used to analyze the combustion performance of the engine. The interesting phenomena of the brake thermal efficiency will also be discussed in this paper. Beside that the analysis of coefficient of variation mean effective pressure (COV_{imep}) and combustion peak pressure in recommended engine performances are discussed in this paper.

Table 4.1 Composition of Biodiesel from many sources.

Source	Composition						
	CH ₄ (%)	CO ₂ (%)	O ₂ (%)	N ₂ (%)	H ₂ S (ppm)	Benzene (mg/m ³)	Toluene (mg/m ³)
Landfill	37-67.9	24.9-40.1	<1-0.5	10-25	15.1-427.5	<1-35.6	10-287
Treatment	57.8-62.6	33.9-38.6	0-0.5	3.4-8.1	24.1-8000	0.1-5	0.1-5
Agricultural	45-75	25-55	0.01-2	0.01-5	10-30000	<300	<300

4.6 Materials and Methods

4.6.1 Simulated biogas and biodiesel properties

Methane(CH₄) gas and carbon dioxide (CO₂) gas are the main composition of biogas fuel (Table 4.1). Therefore, the simulated biogas contains only CH₄ and CO₂ gases which are used in this research. The CH₄ and CO₂ gas are produced by HOKKAIDO AIR WATER INC. Japan. The composition of each gas is explained in table 4.2. The simulated biogases of the following composition were used in the experiment: 40% CH₄ and 60 % CO₂ (labelled M40), 60% CH₄ and 40 % CO₂ (labelled M60), 80% CH₄ and 20 % CO₂ (labelled M80), and 100% CH₄ (labelled M100) with flow rate 5 l/m. The static mixer T6-12-2PT was used to produce an artificial biogas from mixing CH₄ and CO₂.

The pilot fuel was a biodiesel fuel from used cooking oil converted by using NaOH catalyst in transesterification reaction. The biodiesel was produced by Epoch Service Co., Ltd. Shiraoui, Japan. Table 4.3 shows the composition of biodiesel fuel. The biodiesel fuel acts as the source ignition on combustion chamber. The 100 % pure biodiesel was used in whole experiments without being mixed with diesel fuel. In this experiment used the

following fuel set up:

1. Biodiesel
2. Biodiesel + M40 (Methane : CO₂ = 40:60)
3. Biodiesel + M60 (Methane : CO₂ = 60:40)
4. Biodiesel + M80 (Methane : CO₂ = 80:20)
5. Biodiesel + M100 (Methane : CO₂ = 100:0)

Table 4.2 Specification of methane and carbon dioxide

Content	Chemical compound	
	Methane (CH ₄)	Carbon dioxide (CO ₂)
Molecular weight (g/mol)	16.043	44.01
Component Concentration (%)	99.99	>99.95
Density (273.15K, 0.1013 MPa)(g/L)	0.7168	1.977
Specific gravity (Air=1,21.1°C,1atm)	0.554	-
Vapor pressure (MPa abs) (20°C)	-	5.733
solubility(m ³ /m ³)(20°C)	0.033	0.878
Log Pow	1.09	0.83
Melting point(°C)	-182.5	-56.6
Boiling point(°C)	-161.5	-78.5
Flash point(°C)	-187.8	-
Spontaneous Ignition Temperature(°C)	600	-

Table 4.3 Biodiesel Composition

Items	Standard Value	Result	Method
Kinetic Viscosity [40°C]	3.50 mm ² /s ~ 5 mm ² /s	4.196 mm ² /s	JIS K 2283
Triglyceride	Max 0.20 mass %	0.00 mass%	EN 14105
Glycerin	Max 0.02 mass %	0.02 mass%	EN 14105
Methanol	Max 0.20 mass %	0.02mass %	EN 14110
Water	Max 500 ppm	565 ppm	JIS K 2275

4.6.2 Test System

Figure 4.1 shows the experimental set up. It consists of a unit of diesel engine, signal amplifier, dynamometer, gas tank, static mixer and measurement apparatus. In the single-fuel mode, the diesel engine has been tested without modification. The diesel engine was designed and developed to install the pressure indicator and the supplying artificial biogas. The intake system of the diesel engine was slightly modified for dual-fuel mode. The artificial biogas supplying apparatus consists of the gaseous tank of CH₄ and CO₂, the pressure regulator, the flow meter and the static mixer. The artificial biogas is produced by mixing CH₄ and CO₂, which is supplied from each gas tank. Both CH₄ and CO₂ gases are arbitrarily adjusted by a flowmeter and are supplied to combustion chamber through a static mixer. The specification of the diesel engine is shown in Table 4.4. The diesel fuel was injected at 23 degrees before top dead center. The combustion pressure was measured using pressure transducer Kyowa PE-200KJ coupled with amplifier to investigate combustion performance during the dual-fuel mode. The pressure transducer has been installed on the cylinder head of the diesel engine. The obtained combustion pressure data was averaged from cycle-to-cycle with coupled to a tachometer. The combustion pressure

history was collected by the data logger. The tachometer HT-430 was used to measure the engine rotation. The magnetic crankshaft angle sensor detects the crank angle to analyze the piston position. The crankshaft angle was collected by the data logger. The temperature couple sensor was installed around 3 cm close to the exhaust gas valve pipe. The data of exhaust gas was collected by the data logger. The data logger, Graphtec midi Logger GL900, was used to record a combustion pressure, crank angle and temperature of exhaust gas. All the data of the exhaust gas temperature, the crankshaft angle, and the combustion pressure that recorded by the data logger were used to analyse the performance and combustion of the diesel engine.

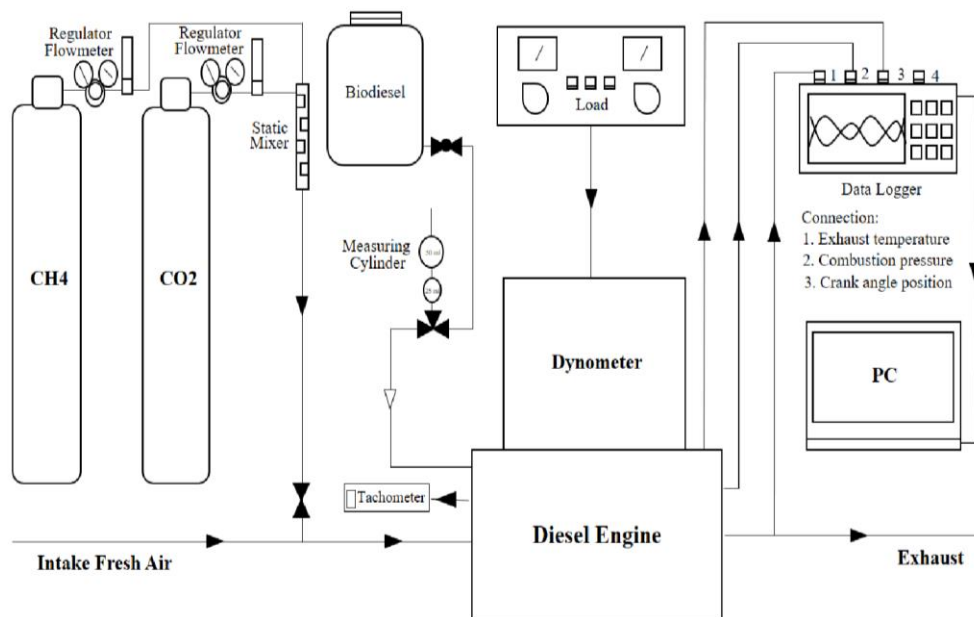


Fig. 4.1 Experimental set up

Table 4.4 Engine specification

Engine model	4 Stroke Air cooled, Single cylinder, Direct-injection
--------------	--

Product Number	DY-30
Compression Ratio	21
Bore × Stroke	76×66mm
Stroke Volume	0.000299 m ³
Maximum Power	4.84 kW/1750 rpm
Maximum Torque	31.57 Nm/1160 rpm
Fuel Injector Opening Pressure	19123 kPa
No. of nozzle hole (Diameter)	4 (0.22 mm)
Intake Air	Naturally Aspirated

In this study, the experimental procedures are explained as follows. The diesel engine is run in 5 fuel condition as explained in section 4.2.1. In every fuel condition, torques are varied from 3.5 Nm, 10.5 Nm, 17.6 Nm, and 24.6 Nm; engine speeds are varied from 1800 rpm, 2000 rpm, 2200 rpm, 2400 rpm, and 2600 rpm. These variations were conducted to measure the combination of engine performance from the low rpm to high rpm and from the low torque to high torque. The measurement is carried out for 5 minutes in stable condition of diesel engine in every torque and speed. Except of these condition, the engine could not be measured in the stable condition during the measurement which means the proper combination of torque and rpm are only by these variations. A total of 300 experiments have been performed and every experiment is repeated for three times and the results are averaged.

4.6.3 Analysis procedure

In order to evaluate the engine performance, several equations are used here. The

performance of diesel engine was analyzed using the thermal efficiency, the specific fuel consumption and the diesel fuel replacement ratio. These equations are defined as bellow.

The thermal efficiency η [%] that indicates how much heat input to the diesel engine will convert output power is shown as:

$$\eta = \frac{W_e}{W_f} \cdot 100 \quad (4.1)$$

Where W_e [kW] is the net horsepower, W_f [kW] is the fuel horsepower.

Net horsepower: W_e [kJ/h]

$$W_e = 3.60 \left(2\pi T \frac{0.4833N_e}{60} \right) \quad (4.2)$$

Torque: T [N·m]

$$T = wq_c l \quad (4.3)$$

where N_e [rpm] is the engine rotation, w [kgf] the weighing torque, l [m](=0.3581m) the shaft length of the dynamometer and q_c [N/kgf](=9.80N/kgf) the power conversion factor.

Fuel horsepower: W_f [kJ/h]

$$W_f = W_{diesel} + W_{biogas} \quad (4.4)$$

Fuel horsepower of diesel fuel: W_{diesel} [kJ/h]

$$W_{diesel} = 3.60(H_{diesel}G_{diesel}) \quad (4.5)$$

Fuel horsepower of biogas: W_{biogas} [kJ/h]

$$W_{biogas} = 3.60(H_{biogas}G_{biogas}) \quad (4.6)$$

Mass flow rate of diesel fuel: G_{diesel} [g/s]

$$G_{diesel} = \frac{\rho_{diesel}b}{t} \quad (4.7)$$

Mass flow rate of CH₄: G_{CH_4} [g/s]

$$G_{biogas} = \frac{v_{CH_4} \rho_{CH_4}}{60} \cdot P \quad (4.8)$$

where H_{diesel} and H_{biogas} [kJ/kg] are the lower calorific value of diesel fuel and CH_4 , ρ_{diesel} and ρ_{CH_4} [g/cm³] the density of diesel fuel and CH_4 , b [cc](=50cc) the fuel tank volume, t [s] the fuel consuming time, v_{CH_4} [L/min] the volume flow rate of CH_4 , P [%] the content of CH_4 fraction.

The specific fuel consumption (SFC) [g/kW·h] is a comparison of fuel consumption to the useful energy. Here, it can be viewed as how many gram of fuel is needed to result 1 kWh of electrical energy. For single-fuel operation mode, it can be calculated as bellow.

$$SFC_{single} = 3600 \cdot \frac{G_{diesel}}{W_e} \quad (4.9)$$

While for dual-fuel mode is defined as:

$$SFC_{dual} = 3600 \cdot \frac{G_{diesel} + G_{biogas}}{W_e} \quad (4.10)$$

The diesel fuel replacement ratio [%] shows how much the percentage of diesel fuel replaced by the biogas. It is defined as following formula.

$$r = \frac{G_{diesel} - G_{dual}}{G_{diesel}} \cdot 100 \quad (4.11)$$

where G_{diesel} [g/s] is the mass flow rate of diesel fuel, G_{dual} [g/s] the mass flow rate of diesel fuel in dual-fuel mode.

$$ber = \frac{W_{biogas}}{W_f} \quad (4.12)$$

Biogas energy ratio (ber) is calculated to analysis the value of energy input from biogas to the total energy in dual fuel mode.

$$\frac{dQ}{d\theta} = \frac{\lambda}{\lambda - 1} P \frac{dV}{d\theta} + \frac{1}{\lambda - 1} V \frac{dP}{d\theta} \quad (4.13)$$

Rate of heat release (ROHR) in eq. 4.13 is commonly used to analyze the combustion performance of the engine. Which λ is the ratio of specific heat ($\lambda=1.35$ in this research); P is combustion pressure; V is cylinder volume and θ is crankshaft angle.

$$COV_{imep} = \frac{\sigma_{imep}}{\bar{x}} \times 100 \quad (4.14)$$

Besides ROHR, coefficient of variation of indicated mean effective pressure (COV_{imep}) analysis is also important in combustion analysis. σ_{imep} is the standard deviation and \bar{x} is average *imep* value. By using the above equations, the performance of the diesel engine was analyzed.

4.7 Results and Discussion

4.7.1 Performance of dual fuel (biodiesel-simulated biogas)

The results of experiments are presented and discussed in detail here. Brake thermal efficiency, biodiesel replacement, biogas energy ratio, specific fuel consumption and exhaust gas temperature are discussed in every subsection.

4.7.1.1 Brake Thermal Efficiency

Brake thermal efficiency (BTE) is one of the indicators to evaluate the performance of diesel engine. Figure 4.2 show the BTE in variation applied torque with different engine speed. Generally, increasing the torque increase the value of BTE. However, the BTE in dual fuel mode is lower than diesel mode at low torque, 3.5 Nm and oppositely in the highest torque condition 24.6 Nm.

Due to the effect of engine speed; the highest BTE in 2600 rpm is 24.95 % in operation M100 with torque 24.6 Nm, the highest BTE in 2400 rpm is 26.28 % in operation M80 with torque 24.6 Nm, the highest BTE in 2200 rpm is 26.27 % in operation M100 with torque 24.6 Nm, the highest BTE in 2000 rpm is 26.72 % in operation M100

with torque 24.6 Nm, and the highest BTE in 1800 rpm is 27.79% in operation M80 with torque 24.6 Nm. Due to the effect of engine torque; the highest BTE in torque 3.4 Nm is 10.73 % in operation biodiesel with speed 2200 rpm, the highest BTE in torque 10.5 Nm is 21.79 % in operation M40 with speed 1800 rpm, the highest BTE in torque 17.6 Nm is 26.75 % in operation M40 with speed 1800 rpm, the highest BTE in torque 24.6 Nm is 27.79 % in operation M80 with speed 1800 rpm. This experiment result has a same trend with Bora et. al [38] that report the result of rice bran biodiesel and biogas in dual fuel diesel engine mode. This experiment results also show that brake thermal efficiency increased by increasing the load [39]

The effect of fuel composition in this research; In the low torque 3.5 Nm with all methane content ratio adjustment reduced the BTE, higher methane adjustment more reduced the BTE. It happened because the low temperature of the engine and the present of methane reduced the oxygen to help the combustion. In the medium torque 10.5 and

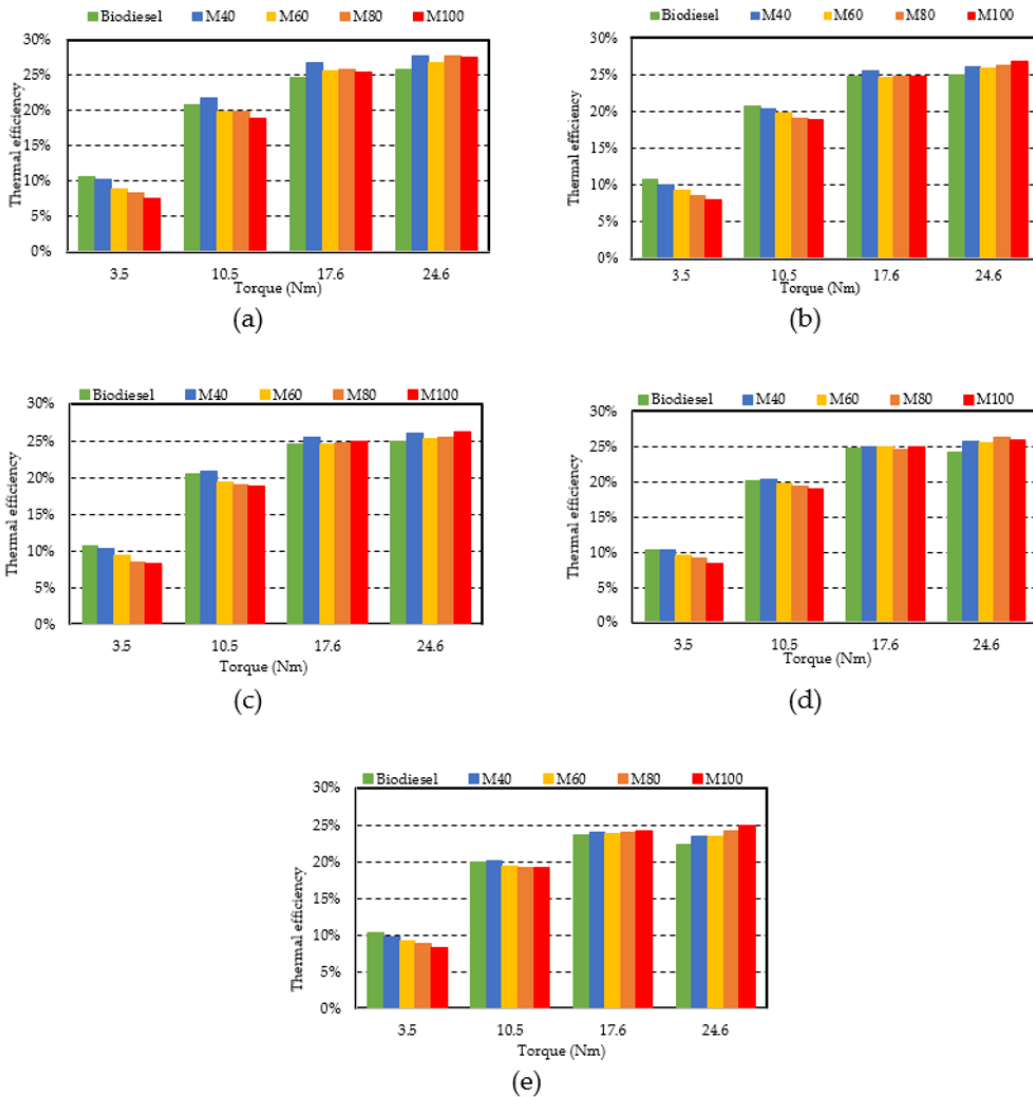


Figure 4.2 Brake thermal efficiency in variation applied torque at (a) 1800 rpm, (b) 2000 rpm, (c) 2200 rpm, (d) 2400 rpm, and (e) 2600 rpm.

17.6 Nm, The BTE increased in certain percentage of methane gas. This occurred due the content ratio of carbon dioxide in the combustion, carbon dioxide dissociated into carbon monoxide and oxygen as explained by Sarkar et.al [40]. Increasing oxygen in the mixture will improve engine performance. In high torque 24.6 Nm shown in all methane content ratio adjustment improve the BTE. However, the best achieved is in the lower rpm, this condition occurred because dissociation carbon dioxide need high temperature and the

low speed engine give more time to burn the fuel air mixture and produce better efficiency.

Overall low applied torque reducing the brake thermal efficiency. This condition occurred due to poor combustion of biogas in low temperature. As a proof the highest brake thermal efficiency achieved at 27.79% in operation M80, 1800 rpm with torque 24.6 Nm. The BTE is exactly influenced by torque, engine speed and biogas composition.

4.7.1.2 Biodiesel replacement and biogas energy ratio

Biodiesel replacement (BR) is calculated using Equation 4.11. BR calculation is important to know how much the percentage of biodiesel fuel that replaced by the biogas. Figure 4.3 shows graphs of relation between torque and BR results. Due to the effect of engine speed; the highest BR in 2600 rpm is 42.9 % in operation M100 with torque 3.5 Nm, the highest BR in 2400 rpm is 49.1 % in operation M100 with torque 3.5 Nm, the highest BR in 2200 rpm is 51.9 % in operation M100 with torque 3.5 Nm, the highest BTE in 2000 rpm is 56.5 % in operation M100 with torque 3.5 Nm, and the highest BR in 1800 rpm is 60.2% in operation M100 with torque 3.5 Nm. Due to the effect of engine torque; the highest BR in torque 3.4 Nm is 60.2% in operation M100 with speed 1800 rpm, the highest BR in torque 10.5 Nm is 54.8 % in operation M100 with speed 1800 rpm, the highest BR in torque 17.6 Nm is 49.2 % in operation M100 with speed 1800 rpm, the highest BR in torque 24.6 Nm is 40.6 % in operation M100 with speed 1800 rpm.

The above explanation show that the low torque applied and engine speed show higher biodiesel fuel replacement. This BR result also have a correlation to the BTR in section before. The highest BR value is 60.2 % in operation M100, 1800 rpm and torque 3.5 Nm.

The characteristic of biogas energy ratio has a similarity trend with biodiesel replacement. Figure 4.4 shows the biogas energy ratio in variation applied torque with

different engine speed. The low torque applied and engine speed show higher biogas energy ratio value. The highest biogas energy ratio value is 71.4 % in operation M100, 1800 rpm and torque 3.5 Nm. And this biogas energy ratio result is in the range of the result that conducted by Sarkar et. al. [41].

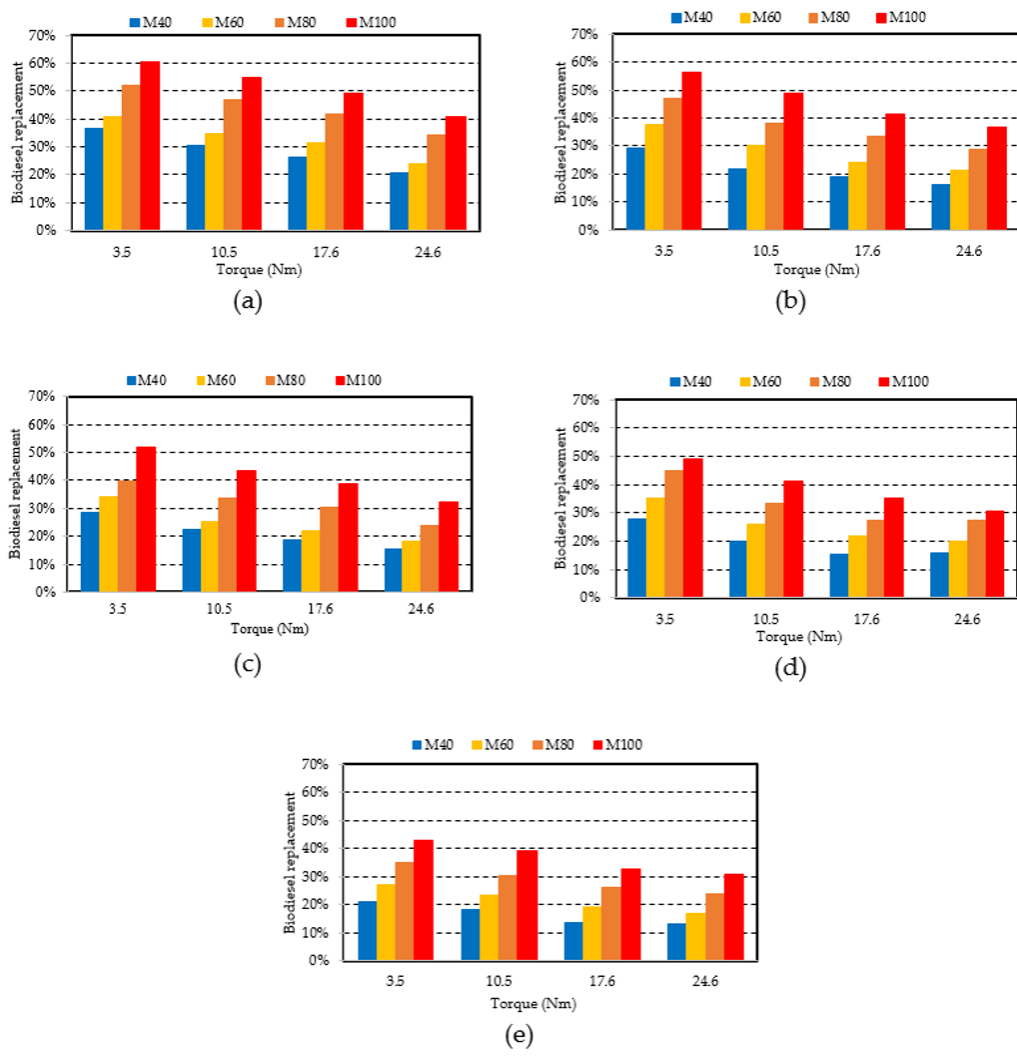


Figure 4.3 Biodiesel replacement in variation applied torque at (a) 1800 rpm, (b) 2000 rpm, (c) 2200 rpm, (d) 2400 rpm, and (e) 2600 rpm

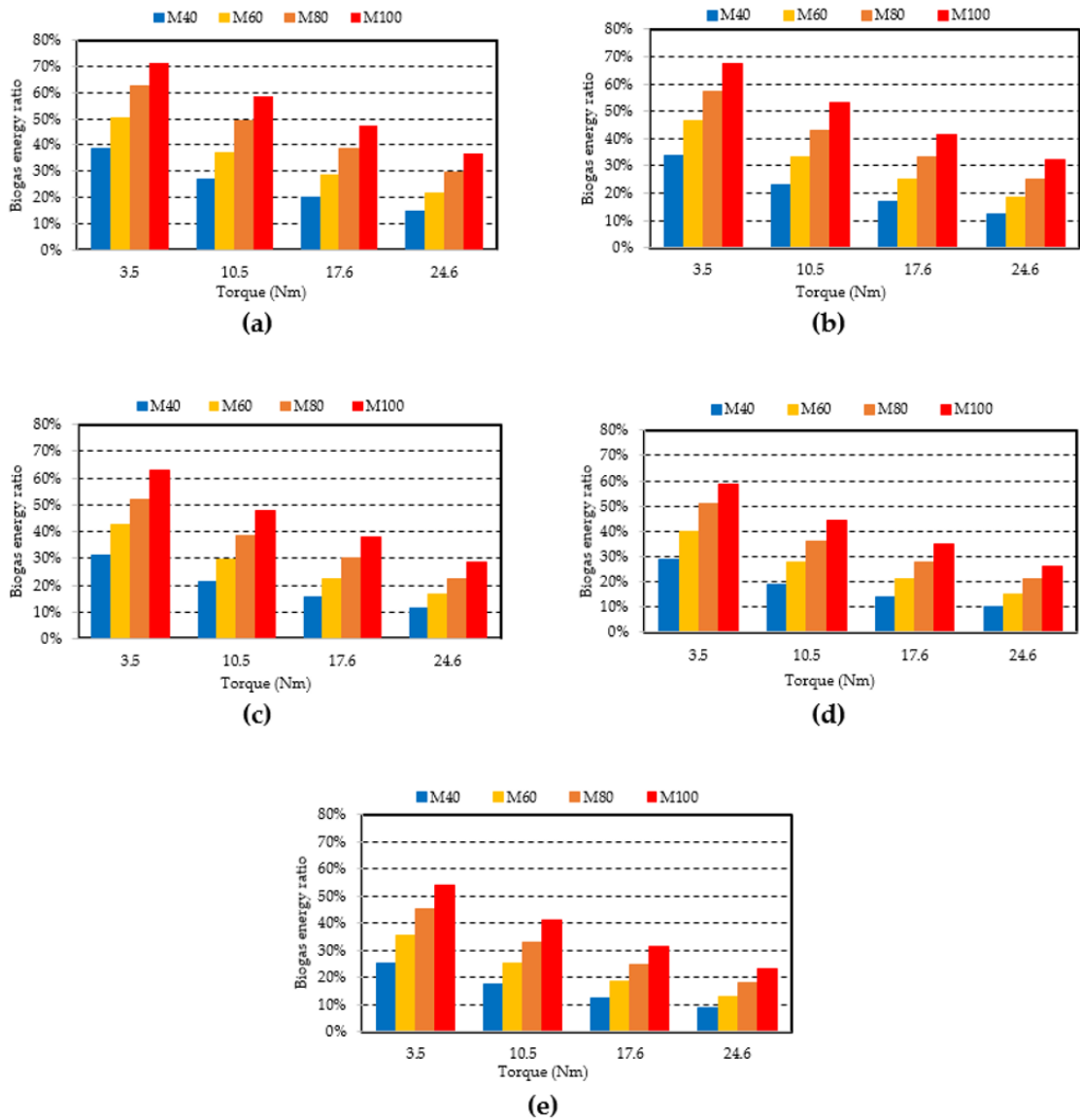


Figure 4.4 Biogas Energy ratio in variation applied torque at (a) 1800 rpm, (b) 2000 rpm, (c) 2200 rpm, (d) 2400 rpm, and (e) 2600 rpm

4.7.1.3 Specific fuel consumption

Specific fuel consumption (SFC) is used as an indicator to evaluate the engine ability to transform the amount of consumed fuel into mechanical energy produced. The low SFC value means the engine consume fuel less to produce mechanical energy, hence it is high efficiency. Equation 4.10 is used to calculate the SFC. Figure 4.5 shows specific fuel consumption in variation applied torque at different engine speeds. Generally, by

increasing engine torque decreased the SFC. The SFC is influenced by engine speed, engine torque and fuel composition. Figure 4.5 shows that the low torque applied and engine speed show higher SFC value. The SFC in this experiment varies from 303.93 g/kWh to 1010.64 g/kWh. The lowest SFC is in engine condition 1800 rpm, Fuel composition M100, and torque 24.6 Nm. The Highest SFC is in engine condition 1800 rpm, Fuel composition M100, and torque 3.5 Nm. However, this result is confirmed in the range as reported in reference [37], that the range of SFC is 0.42 kg/kWh to 2.57 kg/kWh.

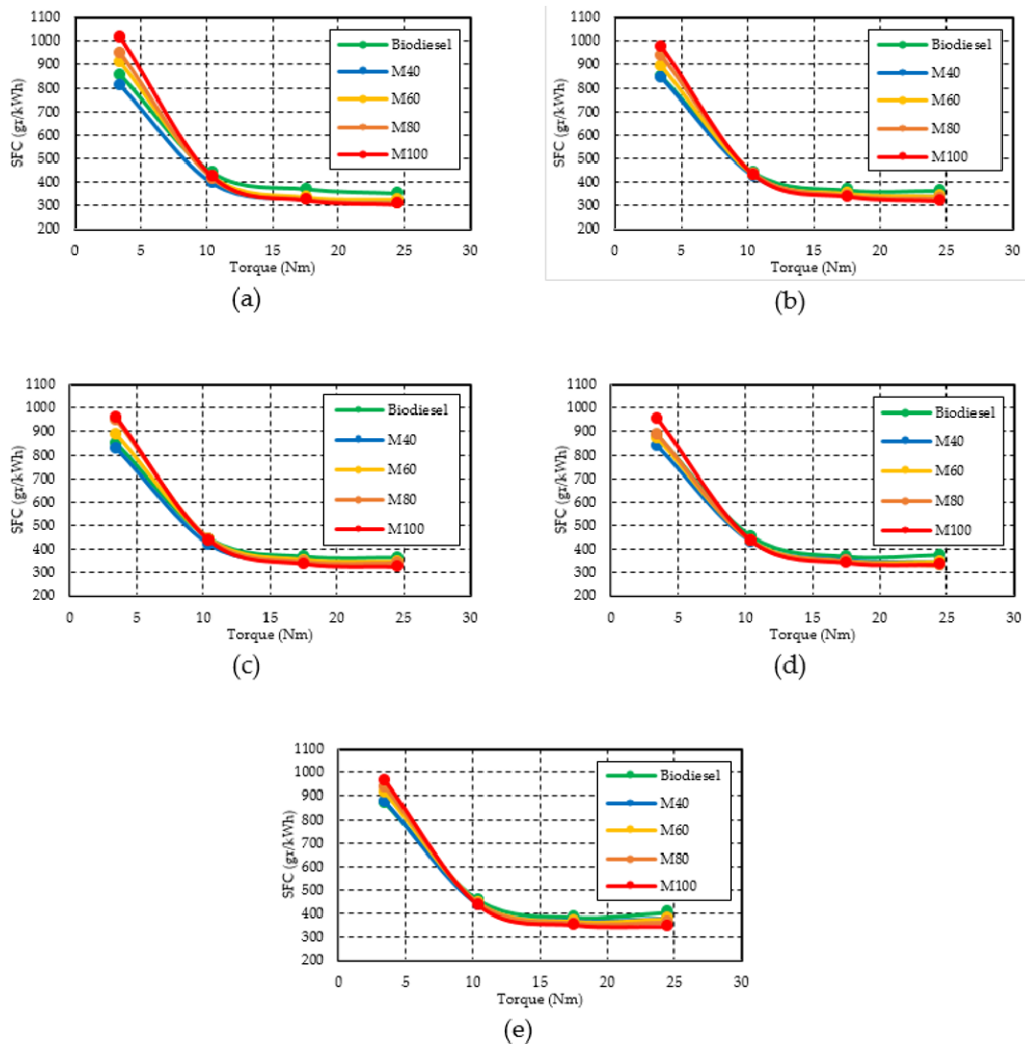


Figure 4.5 Specific fuel consumption in variation applied torque at (a) 1800 rpm, (b) 2000 rpm, (c) 2200 rpm, (d) 2400 rpm, and (e) 2600 rpm

4.7.1.4 Exhaust gas temperature

Exhaust gas temperature was measured in this experiment. Figure 4.6 shows the result of exhaust gas temperature in variation applied torque. In general, increasing engine torque increased the exhaust gas temperature. The exhaust gas temperature in this experiment varies from 61.64 °C to 312 °C. The lowest exhaust gas temperature is in engine condition 1800 rpm, biodiesel, and torque 3.5 Nm. The Highest is in engine condition 2600 rpm, biodiesel, and torque 24.6 Nm. However, experimental result of B.J. Bora et.al has a range of exhaust gas temperature under 400°C [38] which means these exhaust gas temperature results are also reasonable.

Figure 4.6 indicates that high CO₂ content in biogas has higher exhaust temperature than others DFM condition. Biodiesel mode has higher exhaust gas temperature than DFM M100 condition. Especially in the high speed like 2400 rpm and 2600 rpm, the methane gas needs more time for the burning process in the combustion. The condition did not make all the methane gas burned in this condition that caused decreasing exhaust gas temperature. This condition has to be controlled to prevent the knocking that may happen in the experiment, which can affect the life of the engine. The clear explanation of the combustion will be discussed in the next section 4.3.2.

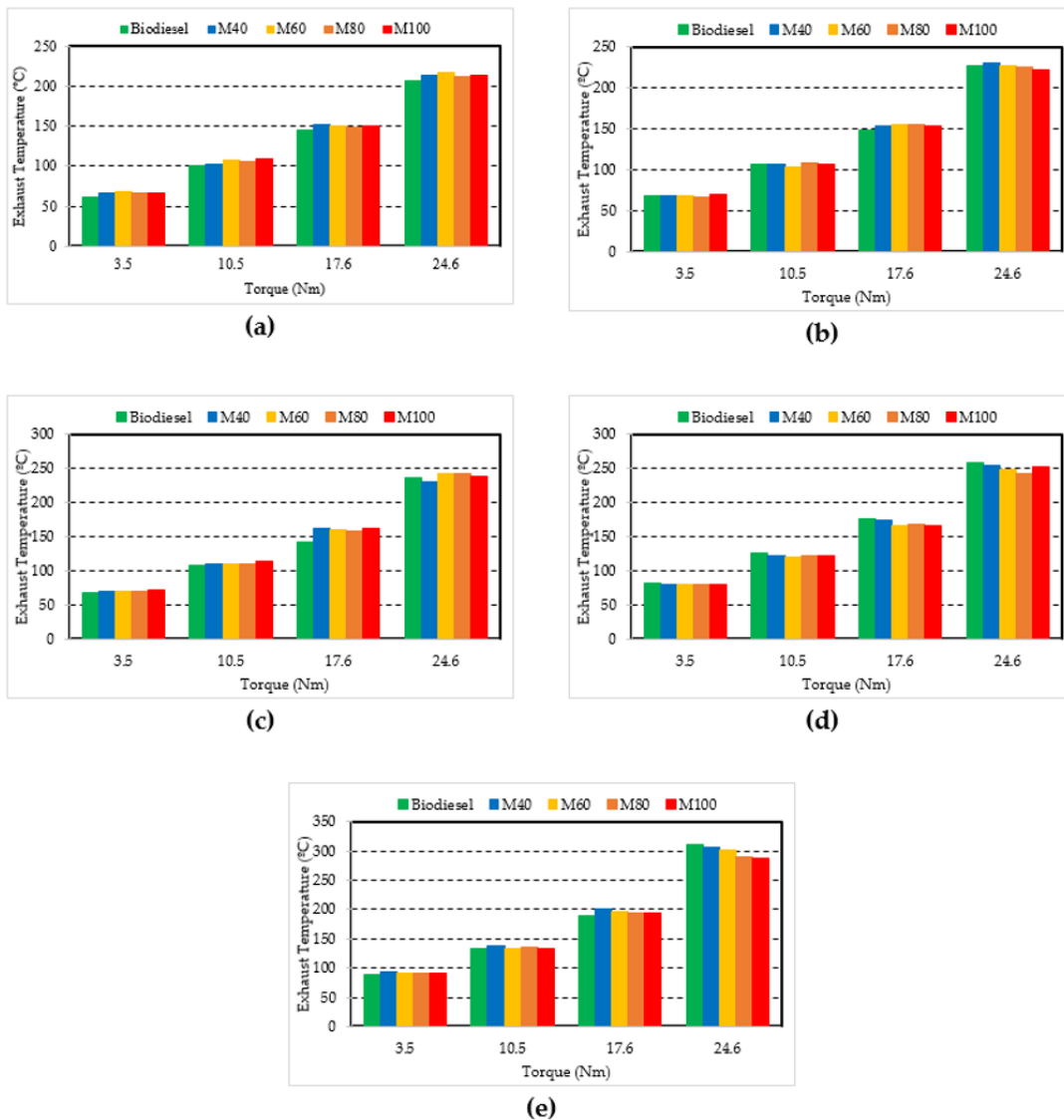


Figure 4.6 Exhaust gas temperature in variation applied torque at (a) 1800 rpm, (b) 2000 rpm, (c) 2200 rpm, (d) 2400 rpm, and (e) 2600 rpm

4.7.1.5 Analysis of methane composition of fuel setup

Section 4.3.1.1 and 4.3.1.2 show the result of brake thermal efficiency and biogas energy ratio to the torque of the diesel engine. The results show a fact that higher methane composition in dual fuel mode does not directly increase the thermal brake efficiency of the diesel engine. However, increasing the methane content decreased the brake thermal

efficiency. It can be observed by comparing the value of the Brake thermal efficiency result to biogas energy fuel ratio results. Two researchers found the same conditions of this problem. Nathan et. al [37] reported the relation of thermal brake efficiency and biogas energy ratio in different bmep from 2.5 bar to 4 bar. Himsar [36] reported the relation of thermal brake efficiency and biogas energy ratio in different flow rate of different composition of injected fuel. In this manuscript, the methane composition of fuel setup was conducted. Figure 4.7 shows the relation of brake thermal efficiency with biogas energy ratio in every fuel set up in different speeds and loads.

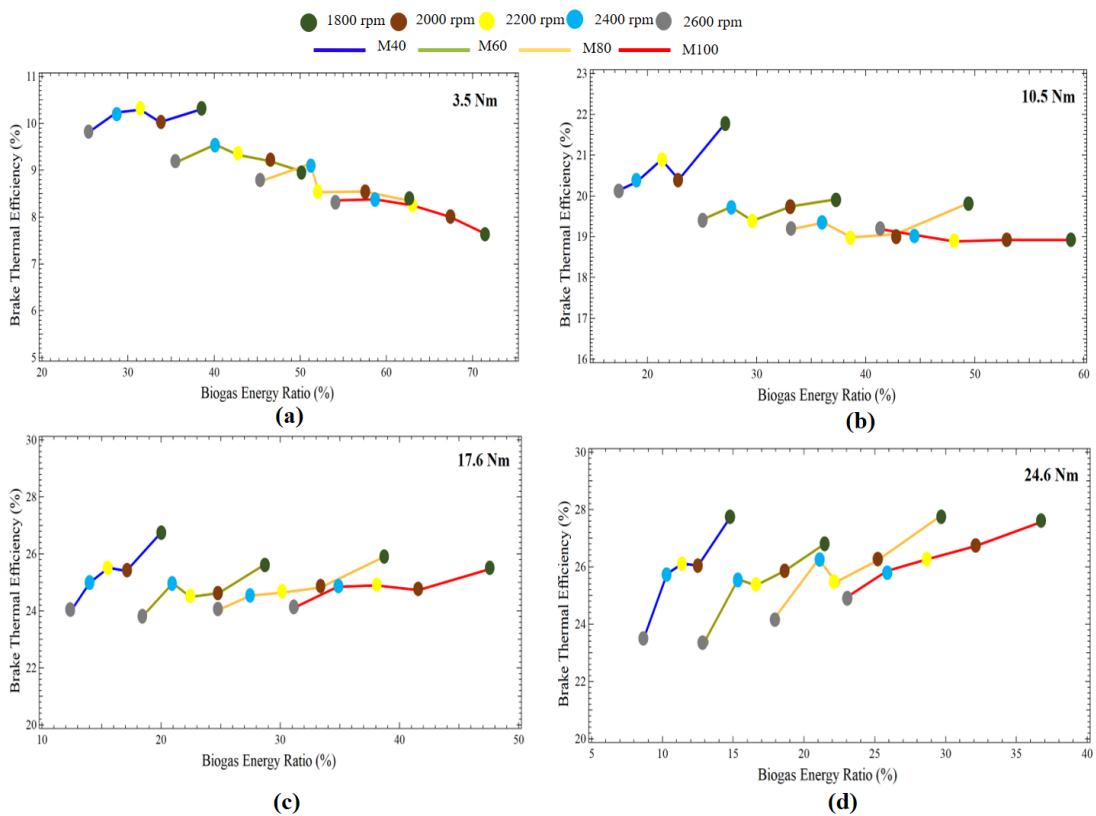


Figure 4.7 Brake thermal efficiency vs. biogas energy ratio in (a) 3.5 Nm (b) 10.5 Nm (c) 17.6 Nm and (d) 24.6 Nm.

In all torques and speeds conditions, M40 has the highest thermal brake efficiency with the lowest biogas energy ratio value. Contrarily, M100 has the lowest thermal brake efficiency with the highest biogas energy ratio value. An Interesting condition was found between M60 and M80. Increasing composition from M60 to M80 for 2000 rpm, 2200 rpm and 2600 rpm made the efficiency decreased in torque 3.5 Nm and 10.5 Nm but it increased in load 17.6 Nm and 24.6 Nm. However, increasing composition from M60 to M80 for 2400 rpm made the efficiency decreased in torque 3.5 Nm 10.5 Nm and 17.6 Nm but it increased in load 24.6 Nm. The trend of Figure 4.7 shows that increasing methane composition is more effective in the high speed and increasing the methane composition will definitely increase the efficiency in low speed. It may be due to the carbon monoxide that unaffected the brake thermal efficiency as reported by [42]. The relation of methane composition due the composition and ROHR will be discussed in the next section.

4.7.2 Combustion pressure and rate of heat release of dual fuel (biodiesel-simulated biogas)

Diesel engine has 4 steps work and it can be observed in the combustion process graph. Commonly in diesel engine, 4 Stages period in combustion process are: 1. Ignition delay period (Start of fuel injection), 2. Pre-combustion (all the fuel had injected and the pressure increase rapidly), 3. main combustion (the fuel is burned and produce power) 4. late combustion (less combustion and the pressure is going down). Since the combustion process of dual fuel mode is more complex than diesel mode. O.M.I Nwafor [40] divided the combustion process to be 5 in the dual fuel mode. The difference is in the ignition delay process because it needs time for the biogas fuel to be burned. All results of combustion pressure and ROHR in these experiments are shown from Figure 4.8 to Figure

4.12. The dot line is ROHR and the line is combustion pressure.

Figure 4.8 shows the combustion pressure and ROHR of the engine in biodiesel fuel and dual fuel mode in 1800 rpm with different torques. In the low torque 3.5 Nm (Figure 4.8a) and medium torque 10.5 Nm (Figure 4.8b), show that higher methane content ratio decreases the combustion peak pressure. In the medium 17.6 Nm (Figure 4.8c) shows that the combustion pressure between dual fuel mode and biodiesel mode in certain methane content has higher combustion pressure. In high torque 24.6 Nm (Figure 4.8d) shows that all the combustion pressure of dual fuel mode become higher than biodiesel mode.

The ROHR in 1800 rpm (low speed) in Figure 4.8 shows that in the low load the ROHR of dual fuel mode becomes lower and when the presence of methane increases, the ROHR value decreases. The high self-ignition temperature of methane and the presence of carbon dioxide affected the ROHR [37]. This proves that the dual fuel mode starts the ignition earlier due to higher temperature condition in the case of medium and high load.

Figure 4.9 shows the combustion pressure and ROHR of the engine in biodiesel fuel and dual fuel mode in 2000 rpm with different torque. Generally, the combustion pressure shows the similarity patterns as in 1800 rpm in Figure 4.8. However, the difference of ignition time delay was found in this condition. The shorter ignition delay was occurred compared to 1800 rpm, higher load produced shorter ignition delay. In the medium to high load, the ROHR of biodiesel became lower than dual fuel mode. As seen from diagram after the premixed combustion occurred from medium and high load, ROHR curve clearly shows higher mixing controlled combustion phase. Furthermore, more fuel injected during higher load extended the combustion process. The ROHR pattern during low load, medium load, and high load are reported in this literature [43].

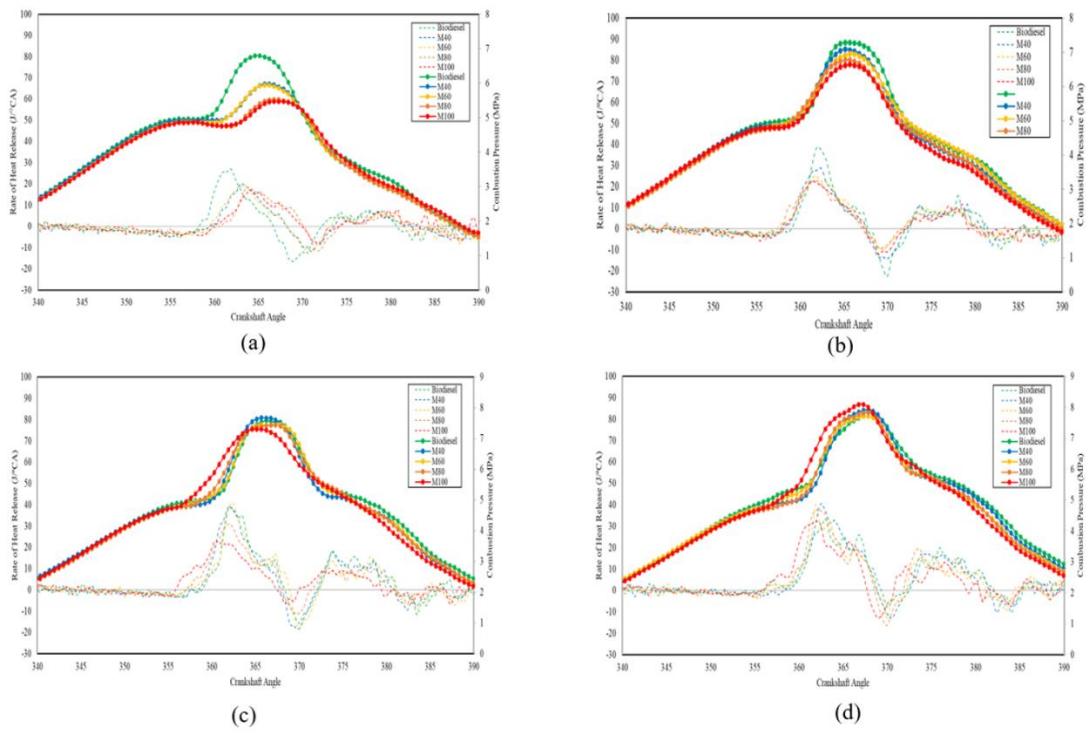


Figure 4.8 Pressure in cylinder and ROHR vs. crankshaft angle position of the engine with speed 1800 rpm at (a) 3.5 Nm (b) 10.5 Nm (c)17.6 Nm and (d) 24.6 Nm.

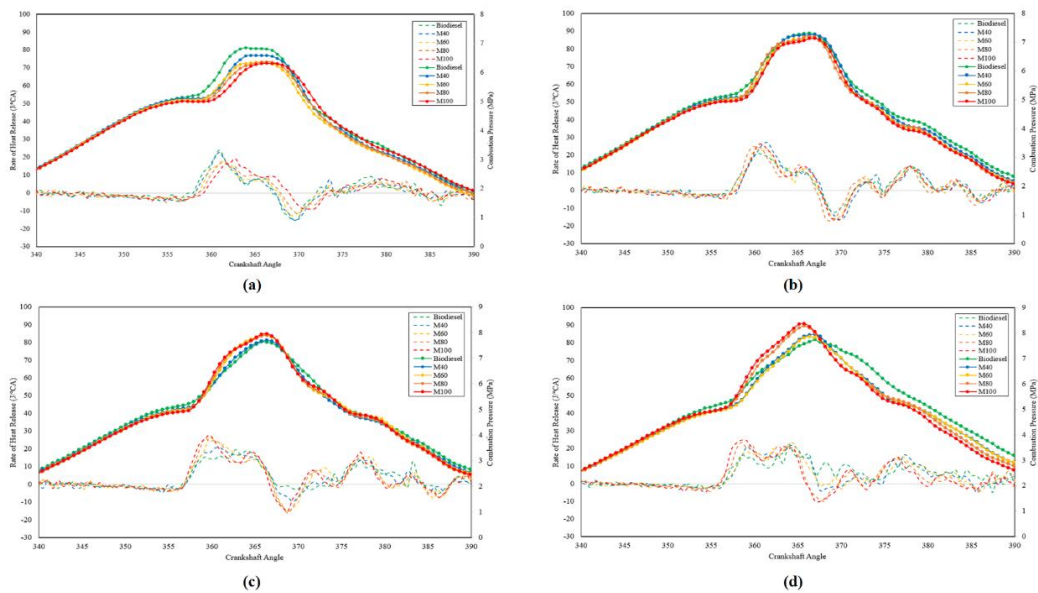


Figure 4.9 Pressure in cylinder and ROHR vs. crankshaft angle position of the engine with speed 2000 rpm at (a) 3.5 Nm (b) 10.5 Nm (c)17.6 Nm and (d) 24.6 Nm.

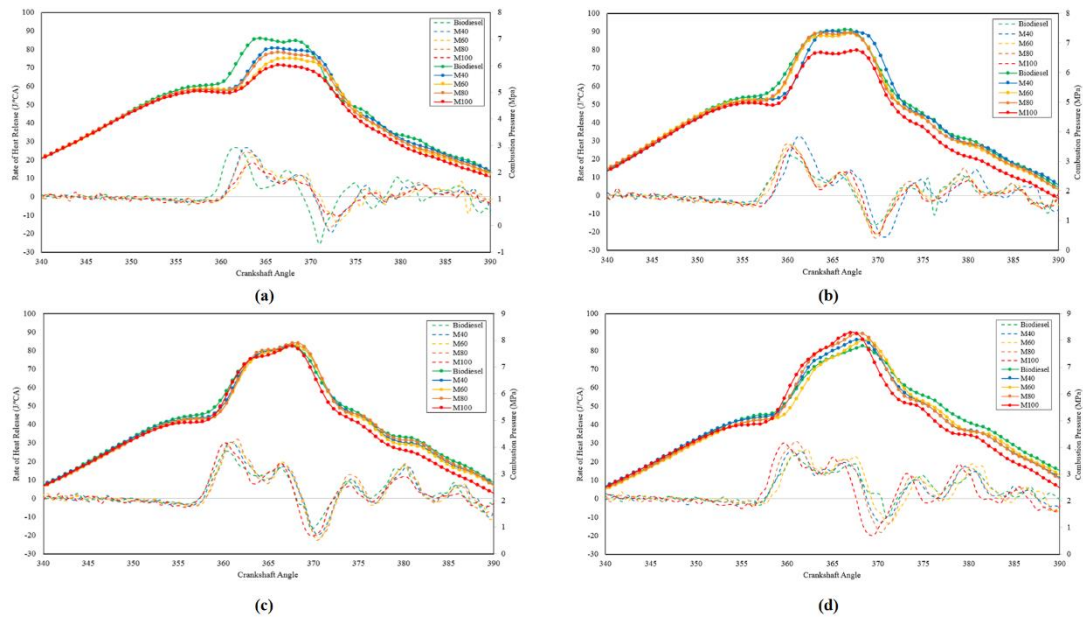


Figure 4.10 Pressure in cylinder and ROHR vs. crankshaft angle position of the engine with speed 2200 rpm at (a) 3.5 Nm (b) 10.5 Nm (c) 17.6 Nm and (d) 24.6 Nm.

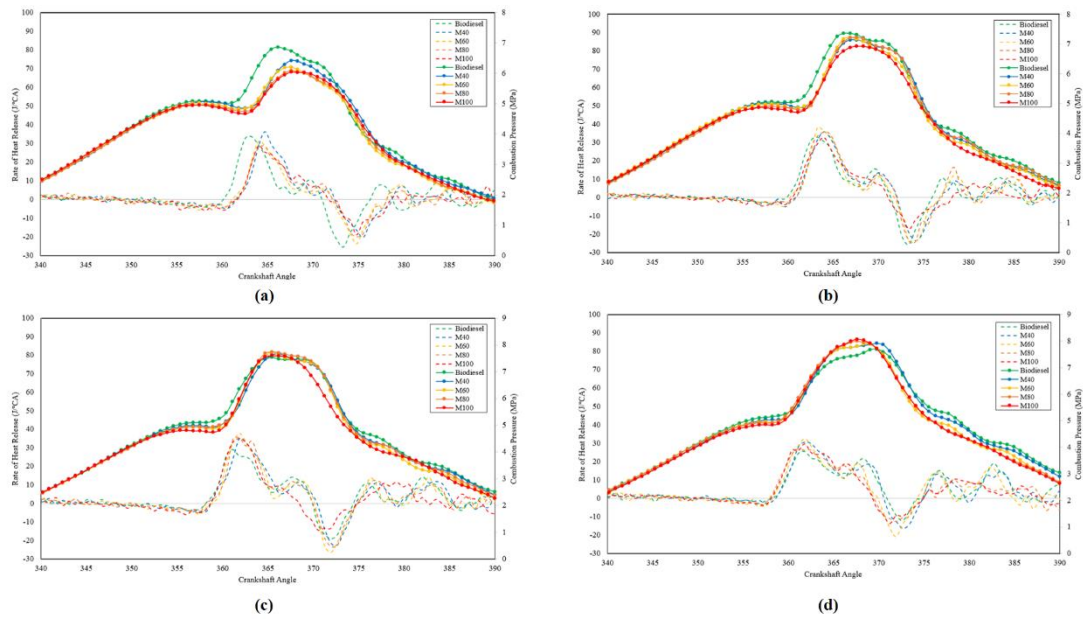


Figure 4.11 Pressure in cylinder and ROHR vs. crankshaft angle position of the engine with speed 2400 rpm at (a) 3.5 Nm (b) 10.5 Nm (c) 17.6 Nm and (d) 24.6 Nm.

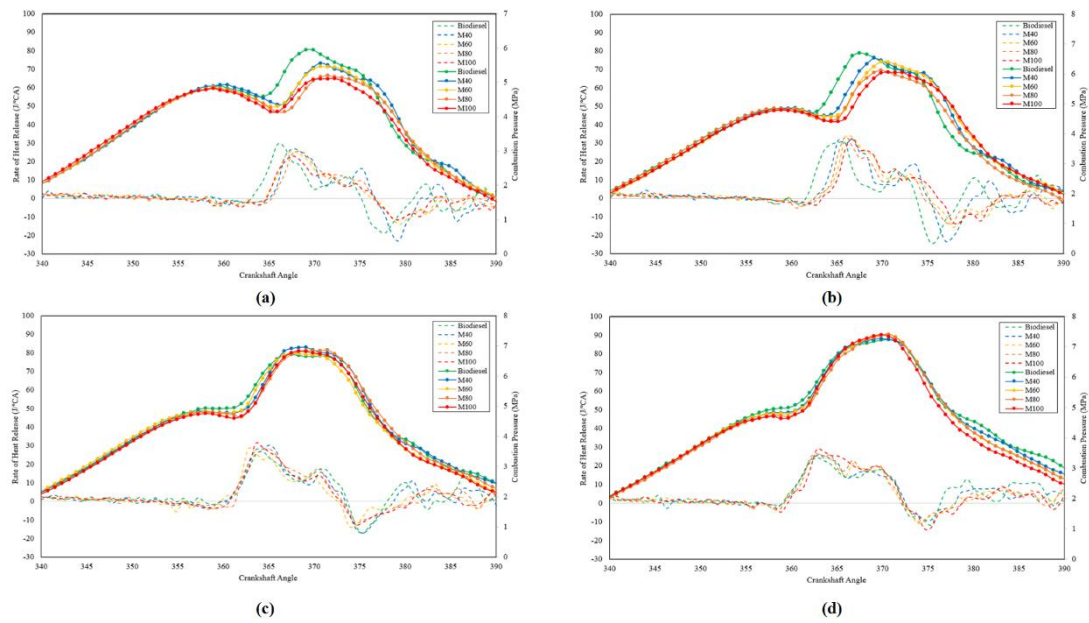


Figure 4.12 Pressure in cylinder and ROHR vs. crankshaft angle position of the engine with speed 2600 rpm at (a) 3.5 Nm (b) 10.5 Nm (c) 17.6 Nm and (d) 24.6 Nm.

Figure 4.10 and Figure 4.11 show the combustion pressure and ROHR of the engine in biodiesel fuel and dual fuel mode respectively in 2200 rpm and 2400 rpm with different torques in both condition, the curves between maximum pressure for each loads clearly shows that dual fuel in low load produces lower combustion peak pressure and higher methane content reduces the combustion peak pressure. However, in the medium to high load the combustion pressure becomes higher when dual fuel is applied. The ROHR curve shows that rapid combustion and longer mix controlled combustion occurred in higher load. The increase of speed and amount of fuel injected during high load increase the pressure and temperature which makes the ignition delay become shorter, in the high load the ignition starts 3 crankshaft angle degrees earlier. It also reported in the literature [44].

In the high engine speed 2600 rpm shown in Figure 4.12 the combustion pressure overall becomes lower compared to all the other engine speed before. High speed makes

less time in the combustion process and affects the combustion pressure and ROHR of the engine. In the low torque, 3.5 Nm longer ignition delay can be clearly found shifting to 4 crankshaft angle degrees after the top dead center. During higher load applied the ignition delay become shorter, but has longer in mix controlled combustion similar to the previous engine speed. It made a critical time for fuel to be burned especially in dual fuel mode that indicates some of the fuel was not burned. Increasing engine speed decreased the ROHR value. This condition shows that not all fuel was burned in the high speed condition. The unburned fuel may be released together with exhaust gas.

The combustion pressure, ROHR and the ignition delay is influenced by the presence and the content of the biogas, torque and engine speed. Overall, increasing the engine speed increased the ignition delay. In addition, the presence of higher methane content ratio in the low torque dropped the combustion peak pressure. Ignition delay can be influenced by some factors such as: 1. Physical delay (fuel is atomized, vaporized, mixed with the air) depends on type of fuel, injection pressure etc [28]. 2. Chemical delay (pre flame reaction takes place, depend on the temperature of the combustion chamber) [39]. However, biogas self-ignition point is higher than biodiesel, higher combustion temperature helps the ignition of the biogas. Mustafi et. al [45] report that perhaps this condition caused by biogas has higher specific heat compared to diesel.

4.7.3 Combustion stability

The combustion stability was analyzed to compare the stability of the combustion of each fuel using coefficient of variation of the indicated mean effective pressure (COV_{imep}) at 2400 rpm. Figure 4.13 shows the relation between COV_{imep} and torque. Total of variation of the averaged 30 engine cycles values were used to build COV_{imep} in this figure. Figure 4.13 shows that all the COV_{imep} results are acceptable due to being lower

than 10% [46,47]. Generally, five percent value of COV_{imep} is considered as the value of the cutoff for the combustion stability [48]. At low torque 3.4 Nm, increasing methane composition in gas fuel increased the value of COV_{imep} . However, increasing the torque decreased the COV_{imep} because higher load mean increases the amount of fuel injected and helps rich fuel mixture in the combustion chamber. Therefore, the most stable operation value is the biodiesel. In the dual fuel operation, there is a pattern that certain methane gas content with the present of the carbon dioxide produce more stable combustion.

Figure 4.14 shows the relation between COV_{imep} and biogas fuel ratio in 2400 rpm as an indicator stability of combustion. Increasing the methane gas, which means increasing biogas fuel ratio increases the COV_{imep} percentage value. The combustions were more stable in lower biogas energy ratios.

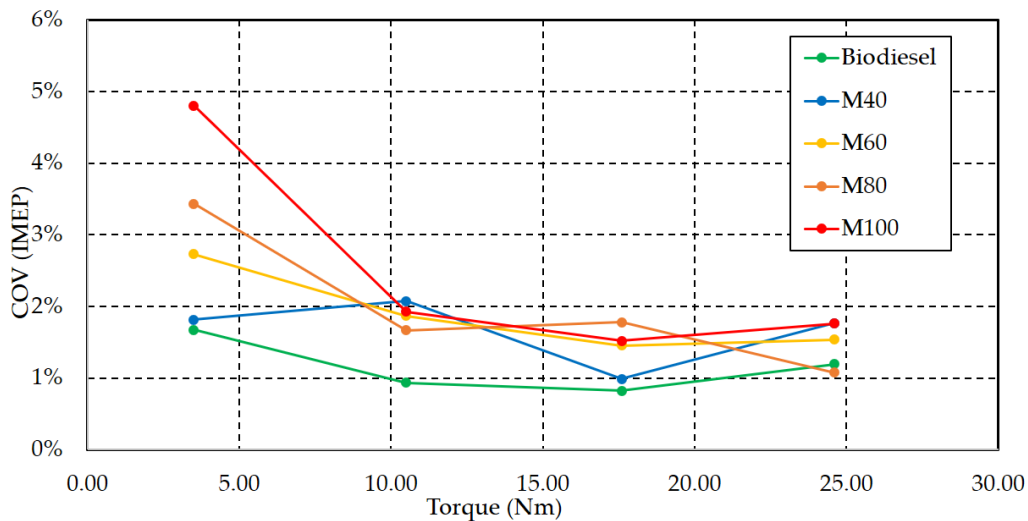


Figure 4.13 COV_{imep} vs. torque in 2400 rpm

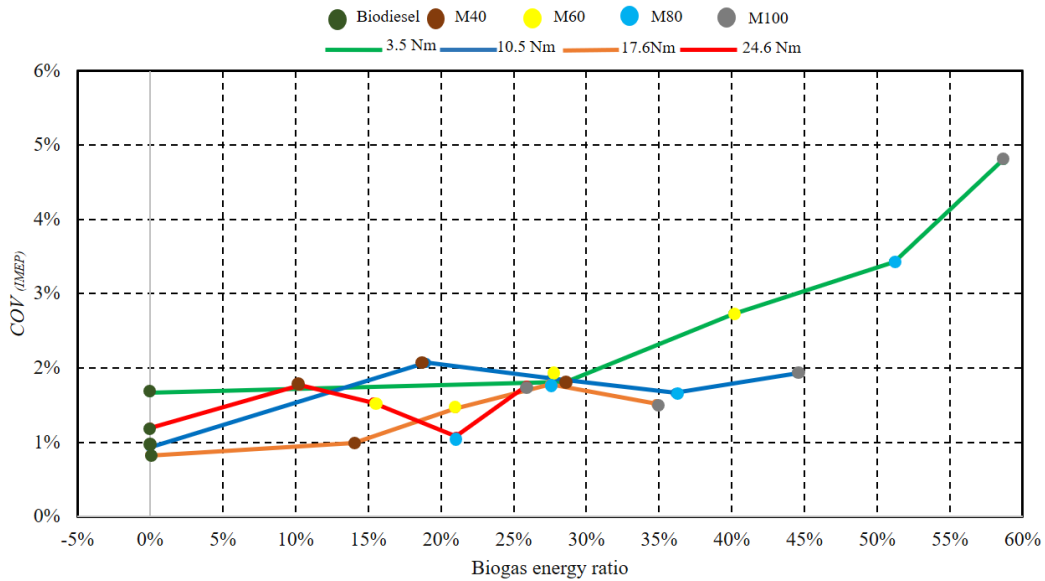


Figure 4.14 COV_{imep} vs. Biogas fuel ratio in 2400 rpm

4.8 Conclusions

The experiment was conducted in diesel engine without substantial modification run in dual fuel mode and biodiesel mode with variants of five fuels, five engine speeds and four torque variation. The performance, rate of heat release and the stability of combustion in both modes have been discussed in section 4.3. The results show:

1. In the low torque dual fuel mode decreased the thermal efficiency. Oppositely, the thermal efficiency increased in high torque. Furthermore, engine speed and methane content ratio uncertainty affected thermal efficiency. The highest thermal efficiency 27.79% was achieved when the engine speed was at 1800 rpm, 24.6 Nm, M80.
2. There is a condition that carbon dioxide content in the biogas can enrich the brake thermal efficiency of the engine. The highest brake thermal efficiency 27.79 %

was achieved at dual fuel mode M80.

3. Biodiesel replacement and biogas energy share become higher when low torque and low engine speed were applied in DFM with higher methane content ratio. The maximum 60.2% and 71.4% respectively for biodiesel replacement and biogas energy share at 1800 rpm, 3.5 Nm, M100.
4. The relation between biodiesel replacement, biogas energy ratio and brake thermal efficiency due to methane content show that there is a maximum effect of methane content ratio in dual fuel mode. From exhaust temperature shown in the high torque, and high engine speed, the exhaust temperature significantly decreased because of an increased unburned rich fuel mixture.
5. Engine speed, loads and methane content ratio uncertainty affected the specific fuel consumption. The highest specific fuel consumption 1010.64 g/kWh at 1800 rpm, 3.5 Nm, M100. The lowest specific fuel consumption 303.93 g/kWh at 1800 rpm, 24.6 Nm, M100.
6. The combustion pressure and the rate of heat release showed that methane content ratio affected engine speeds and loads conditions. Overall, low torque produces lower combustion pressure, and lower rate of heat release by using dual fuel mode particularly when more methane content ratio was adjusted. In addition, longer heat release with shorter ignition delayed in high torque operation.
7. The instability of the engine escalating when COV_{imep} values increased significantly from 1.7% to 4.89% when the methane content ratio rise in the low torque condition.

References

1. IPCC, Guidelines for National Greenhouse Gas Inventories, 2006.
2. IPCC, 2014: Summary for Policymakers. In: Climate Change 2014: Mitigation of Climate Change. Contribution of Working Group III to the Fifth Assessment Report of the Intergovernmental Panel on Climate Change [Edenhofer, O., R. Pichs-Madruga, Y. Sokona, E. Farahani, S. Kadner, K. Seyboth, A. Adler, I. Baum, S. Brunner, P. Eickemeier, B. Kriemann, J. Savolainen, S. Schlömer, C. von Stechow, T. Zwickel and J.C. Minx (eds.)]. Cambridge University Press, Cambridge, United Kingdom and New York, NY, USA.
3. Japan's National Greenhouse Gas Emission in Fiscal Year 2016 (Final Figure) < Executive Summary >, Ministry of the Environment, Government of Japan.
4. R.L. McCormic, C.J. Tennant, R.R. Hayes, S. Black, Sharp, Regulated Emissions from Biodiesel Tested in Heavy Duty Engines Meeting 2004 Emission Standards, SAE 2005-01-2200 (2005).
5. S.H. Yoon, C.S. Lee, Experimental investigation on the combustion and exhaust emission characteristics of biogas–biodiesel dual-fuel combustion in a CI engine, Fuel Process Technol, 92 (2011), pp. 992-1000.
6. J.-O. Müller, D.S. Su, R.E. Jentoft, U. Wild, R. Schlögl, Diesel engine exhaust emission: oxidative behavior and microstructure of black smoke soot particulate, Environ Sci Technol, 40 (2006), pp. 1231-1236.
7. S.H. Yoon, S.H. Park, C.S. Lee, Experimental investigation on the fuel properties of biodiesel and its blends at various temperatures, Energy and Fuels, 22 (2008), pp. 652-656.
8. G. El Diwani, N.K. Attia, S.I. Hawash, Development and evaluation of biodiesel fuel

- and by-products from jatropha oil, *Int J Environ Sci Technol*, 6 (2) (2009), pp. 219-224.
9. A. El-Zein, I. Nuwayhid, M. El-Fadel, S. Mroueh, Did a ban on diesel-fuel reduce emergency respiratory admissions for children? , *Sci Total Environ*, 384 (1–3) (2007), pp. 134-140.
 10. R.O. McClellan, T.W. Hesterberg, J.C. Wall, Evaluation of carcinogenic hazard of diesel engine exhaust needs to consider revolutionary changes in diesel technology, *Regul Toxicol Pharmacol*, 63 (2012), pp. 225-258.
 11. Sahar et. al., Biodiesel production from waste cooking oil: An efficient technique to convert waste into biodiesel, *Sustainable Cities and Society*, 41 (2018), pp. 220-226.
 12. S. Jaichandar, K. Annamalai, The Status of Biodiesel as an Alternative Fuel for Diesel Engine –An Overview, *Journal of Sustainable Energy & Environment* 2 (2011) 71-75.
 13. J. M Fonseca et. al., Biodiesel from waste frying oils: Methods of production and purification, *Energy Conversion and Management* 184 (2019), pp. 205-218
 14. A. Demirbas, *Biorefineries: for Biomass Upgrading Facilities*, Springer-Verlag, London (2010), 10.1007/978-1-84882-721-9.
 15. A. Demirbas, *Biofuels: Securing the Planet's Future Energy Needs*, Springer-Verlag London Limited (2009), 10.1007/978-1-84882-001-1.
 16. A.E. Atabani, et al., A comparative evaluation of physical and chemical properties of biodiesel synthesized from edible and non-edible oils and study on the effect of biodiesel blending, *Energy*, 58 (2013), pp. 296-304.
 17. P. Mohamed Shameer, et al., Effects of fuel injection parameters on emission characteristics of diesel engines operating on various biodiesel: a review, *Renew*

Sustain Energy Rev, 67 (2017), pp. 1267-1281

18. H. Liu, et al., Combustion and emission characteristics of a direct injection diesel engine fueled with biodiesel and PODE/biodiesel fuel blends, *Fuel*, 209 (Supplement C) (2017), pp. 62-68
19. D.C. Rakopoulos, C.D. Rakopoulos, E.G. Giakoumis, R.G. Papagiannakis, D.C. Kyritsis, Influence of properties of various common bio-fuels on the combustion and emission characteristics of high-speed DI (direct injection) diesel engine: vegetable oil, bio-diesel, ethanol, n-butanol, diethyl ether, *Energy*, 73 (2014), pp. 354-366, 10.1016/j.energy.2014.06.032
20. J. Pullen, K. Saeed, Factors affecting biodiesel engine performance and exhaust emissions Part I: Review, *Energy*, 72 (2014), pp. 1-16, 10.1016/j.energy.2014.04.015
21. H. Jung, D.B. Kittelson, M.R. Zachariah, Characteristics of SME biodiesel-fueled diesel particle emissions and the kinetics of oxidation, *Environ Sci Technol*, 40 (2006), pp. 4949-4955.
22. Fazal MA, Haseeb ASMA, Masjuki HH. Comparative corrosive characteristics of petroleum diesel and palm biodiesel for automotive materials. *Fuel Process Technol* 2010;91:1308–15
23. Singh B, Korstad J, Sharma Y.C. A critical review on corrosion of compression ignition (CI) engine parts by biodiesel and biodiesel blends and its inhibition. *Renewable and Sustainable Energy Reviews* 16 (2012) 3401-3408.
24. Cebula, J., Biogas purification by sorption techniques, *ACEE Journal*, 2, pp. 95-103, 2009.
25. S.E. Hosseini, M.A. Wahid, Biogas utilization: experimental investigation on biogas flameless combustion in lab-scale furnace, *Energy Convers Manage*, 74 (2013), pp.

26. B.B. Sahoo, N. Sahoo, U.K. Saha, Effect of engine parameters and type of gaseous fuel on the performance of dual-fuel gas diesel engines – a critical review, *Renew Sust Energy Rev*, 13 (2009), pp. 1151-1184.
27. Swami SN, Mallikarjuna JM, Ramesh A. An experimental study of the biogas-diesel HCCI mode of engine operation. *Energy Convers Manage* 2010;51:1347-53.
28. Karim GA. The dual fuel engine. In: Evans RI, editor. *Automotive alternatives*, new York: plenum press; 1987. pp 83-104
29. K. Cacua, A. Amell, F. Cadavid, Effects of oxygen enriched air on the operation and performance of a diesel-biogas dual fuel engine, *Biomass Bioenergy*, 45 (2012), pp. 159-167, 10.1016/j.biombioe.2012.06.003.
30. M. Feroskhan, S. Ismail, M. G. Reddy, A.S. Teja, Effects of charge preheating on the performance of a biogas-diesel dual fuel Diesel engine, *Engineering Science and Technology, an International Journal*, Volume 21, Issue 3, June 2018, Pages 330-337, 10.1016/j.jestch.2018.04.001.
31. A. Sarkar and U.J Saha , Role of global fuel-air equivalence ratio and preheating on the behaviour of a biogas driven dual fuel diesel engine, *Fuel*, Volume 232, 2018 , Pages 743-754, <https://doi.org/10.1016/j.fuel.2018.06.016>.
32. A. yousefi, H. Guo, M. Birouk, Effect of diesel injection timing on the combustion of natural gas/dieseldual-fuel engine at low-high load and low-high speed conditions, *Fuel*, 235 (2019) pp. 838-846.
33. S. verma, L.M. Das, S.C. Kaushik, S.S. Bhatti, The effects of compression ratio and EGR on the performance and emission characteristics of diesel-biogas dual fuel engine, *Applied thermal Engineering* 150 (2019), pp. 1090-1103.

34. H. huang et. al, Development of a new reduced diesel/natural gas mechanism for dual-fuel engine combustion and emission prediction, *Fuel* 236 (2019) pp. 30-42.
35. H. huang et. al, Experimental and numerical study of multiple injection effects on combustion and emission characteristics of natural gas–diesel dual-fuel engine, *Energy conversion and management* 183 (2019) pp. 84-96.
36. H. Ambarita , Performance and emission characteristics of a small diesel engine run in dual-fuel (diesel-biogas) mode, *Case Studies in Thermal Engineering*, Volume 10, September 2017, Pages 179-191, *Energy Convers. Manag.*, 51 (2010), pp. 1347-1353. 10.1016/j.csite.2017.06.003
37. S.S. Nathan, J.M. Mallikarjuna, A. Ramesh, An experimental study of the biogas–diesel HCCI mode of engine operation, *Energy Convers. Manag.*, 51 (2010), pp. 1347-1353
38. Bhaskor J. Bora, Ujjwal K. Saha, Experimental evaluation of a rice bran biodiesel e biogas run dual fuel diesel engine at varying compression ratios, *Renewable Energy* 87 (2016) 782e790, 10.1016/j.renene.2015.11.002.
39. M.D. Phan, W. Kanit, Study on biogas premixed charge diesel dual fuelled engine, *Energy Conversion and Management*, 48 (2007), pp. 2286-2308
40. O.M.I. Nwafor, Combustion characteristics of dual-fuel diesel engine using pilot injection ignition, *Institution of Engineers (India) Journal*, 84 (April 2003), pp. 22-25.
41. A. Sarkar and U.J Saha , Role of global fuel-air equivalence ratio and preheating on the behaviour of a biogas driven dual fuel diesel engine, *Fuel*, Volume 232, , Pages 743-754, <https://doi.org/10.1016/j.fuel.2018.06.016>
42. C.C.M. Luijten, E. Kerkhof, Jatropha oil and biogas in a dual fuel Diesel engine for rural electrification, *Energy Convers. Manag.*, 52 (2) (2011), pp. 1426-1438,

10.1016/j.enconman.2010.10.005

43. Amr Ibrahim, An experimental study on using diethyl ether in a diesel engine operated with diesel-biodiesel fuel blend, *Engineering Science and Technology, an International Journal*, 21 (2018), pp. 1024-1033.
44. D.C. Rakopoulos, C.D. Rakopoulos, Dimitrios C. Kyritsis, Butanol or DEE blends with either straight vegetable oil or biodiesel excluding fossil fuel: Comparative effects on diesel engine combustion attributes, cyclic variability and regulated emissions trade-off, *Energy*, 115 (2016), pp. 314-325.
45. N.N. Mustafi, R.R. Raine, S. Verhelst, Combustion and emissions characteristics of a dual fuel engine operated on alternative gaseous fuels, *Fuel*, 109 (2013), pp. 669-678, 10.1016/j.fuel.2013.03.007
46. Ahmet Uyumaz, Combustion, performance and emission characteristics of a DI diesel engine fuel blends with mustard oil biodiesel fuel blends at different engine loads, *Fuel* 212 (2018) 256–26.
47. A. Karmakar, S. Karmakar, S. Mukherjee, Properties of various plants and animals feed stocks for biodiesel production, *Bioresour Technol*, 101 (2010), pp. 7201-7210.
48. Seokhwan Lee, Tae Young Kim, Performance and emission characteristic of DI diesel engine operated with diesel/DEE blended fuel, *Applied Thermal Engineering*, 121 (2017) pp. 454-461.

Chapter 5

SUMMARY

In this dissertation, two topics about copper element have discussed; (1) about the

mechanism behind ant nest corrosion on copper tube and (2) Estimation of Exchange Current Density on Copper Electrode by Using Differential Polarization Method. The result of both topics are summarized as follows:

1. Ant nest corrosion occurred on copper tube that immersed in in 100 ppm HCHO+ 1000 ppm Cu(HCOO)₂ solution, 1000 ppm Cu(HCOO)₂ solution and 1000 ppm Cu(HCOO)₂ added HCOOH to pH=3 solution. It took 20 days immersion time to occur ANC on copper tube and around 10 days the corrosion occur on surface of copper tube in all solution condition. Copper tube that immersed in 100 ppm HCHO+ 1000 ppm Cu(HCOO)₂ solution, 1000 ppm Cu(HCOO)₂ solution almost have the same behaviour compared to copper tube that immersed in 1000 ppm Cu(HCOO)₂ added HCOOH to pH=3 solution. It shown from the chemical stable compound that produced (Cu₂O) in 20 days immersion. It was shown that the polarization curve for 0 days and 20 days do not appear changed. Analysis using the polarization resistance curves revealed. these is typical of extremely fast corrosion. The comproportional reaction and disproportionation reaction play an important role in the whole mechanism of ant nest corrosion on the copper tube.
2. The newly-proposed technique (DPM) showed that the i_0 and α_c can be estimated using the geometrical characteristics such as a horizontal line and straight slope line with $d\log h/d\log|i|=-1$. It was shown that the *HER* on copper electrode in 0.5 mol dm⁻³ H₂SO₄ solution has $i_0=10^{-3}$ mA cm⁻² and $\alpha_c=0.55$ in 1 cycle and 0.58 in 5 cycle. This result is in the range of 10^{-5.6} to 10^{-2.9} mA.cm⁻². It is demonstrated that the proposed technique has advantages: (1) accurate finding of the Tafel slope region and (2) easy removing of physical resistances such as oxide film and solution resistance.

The results of experiments are presented and discussed in section 4.3.1. Brake thermal efficiency, biodiesel replacement, biogas energy ratio, specific fuel consumption and exhaust gas temperature are summarized as follow; In the low torque dual fuel mode decreased the thermal efficiency. Oppositely, the thermal efficiency increased in high torque. Furthermore, engine speed and methane content ratio uncertainty affected thermal efficiency. There is a condition that carbon dioxide content in the biogas can enrich the brake thermal efficiency of the engine. Biodiesel replacement and biogas energy share become higher when low torque and low engine speed were applied in DFM with higher methane content ratio. The relation between biodiesel replacement, biogas energy ratio and brake thermal efficiency due to methane content show that there is a maximum effect of methane content ratio in dual fuel mode. From exhaust temperature shown in the high torque, and high engine speed, the exhaust temperature significantly decreased because of an increased unburned rich fuel mixture. Engine speed, loads and methane content ratio uncertainty affected the specific fuel consumption. The combustion pressure and the rate of heat release showed that methane content ratio affected engine speeds and loads conditions. Overall, low torque produces lower combustion pressure, and lower rate of heat release by using dual fuel mode particularly when more methane content ratio was adjusted. In addition, longer heat release with shorter ignition delayed in high torque operation. The instability of the engine escalating when COV_{imep} values increased significantly from 1.7% to 4.89% when the methane content ratio rises in the low torque condition.

APPENDIX I

***E*-pH diagram**

E-pH diagram (Pourbaix diagram) is used to identify the stable chemical compound that may present in the corrosive environment. *E*-pH diagram of Cu and

Cu(HCOO)₂ is used to clarify the chemical specimen that present in the environment that conducted in chapter 2.

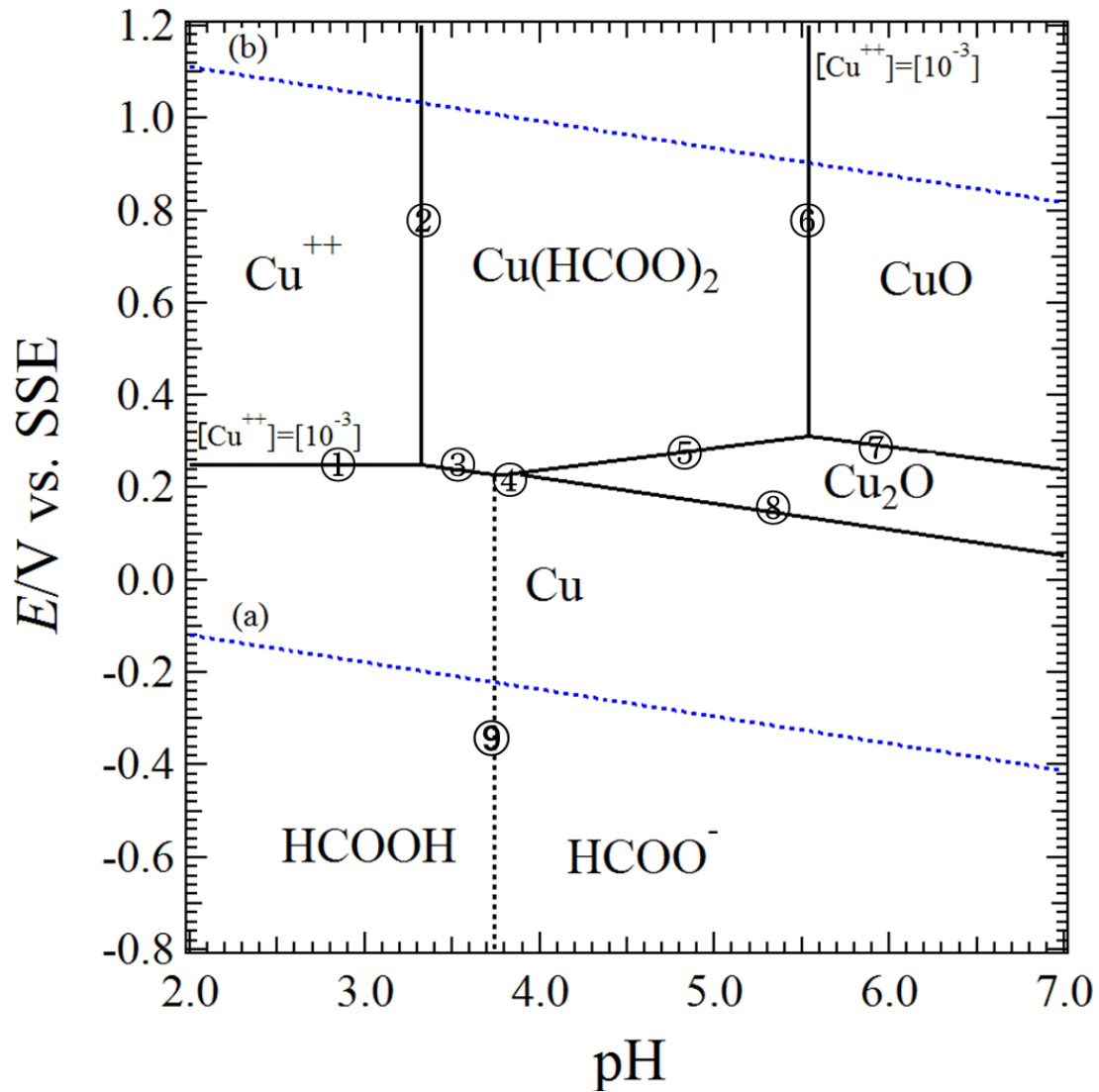


Figure E-pH Diagram of Cu and Cu(HCOO)₂, with assumption that the concentration of total dissolved copper ions $[Cu^{++}]$ was $10^{-3} \text{ mol.kg}^{-1}$



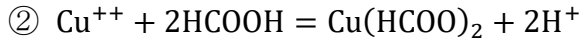
$$\mu_{Cu} = \mu_{Cu^{++}} + RT \ln[Cu^{++}] - 2FE$$

$$\mu_{\text{Cu}} = \mu_{\text{Cu}^{++}} + RT\ln[10^{-3}] - 2FE$$

$$0 = (65.49 \times 10^3) + (2.3 \times 8.314 \times 298 \times (-3)) - (2 \times 296500 \times E)$$

$$E = \frac{(65.49 \times 10^3) + (2.3 \times 8.314 \times 298 \times (-3))}{2 \times 96500}$$

$$E = 0.251 \text{ V vs SHE}$$



$$\mu_{\text{Cu}^{++}} + RT\ln[\text{Cu}^{++}] + 2\mu_{\text{HCOOH}} = \mu_{\text{Cu}(\text{HCOO})_2} + 2\mu_{\text{H}^+} + 2RT\ln[\text{H}^+]$$

$$\mu_{\text{Cu}^{++}} + RT\ln[10^{-3}] + 2\mu_{\text{HCOOH}} = \mu_{\text{Cu}(\text{HCOO})_2} + RT\ln[\text{H}^+]$$

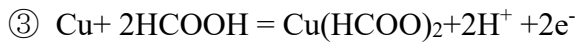
$$(65.49 \times 10^3) + (2.3 \times 8.314 \times 298 \times (-3)) + 2 \times (-361.35 \times 10^3)$$

$$= (-636.3 \times 10^3) + 2 \times 2.3 \times 8.314 \times 298 \log[\text{H}^+]$$

$$-38005.2468 = 13396.8312 \log[\text{H}^+]$$

$$-38005.2468 = -13396.8312 \text{pH}$$

$$\text{pH} = 3.335$$



$$\mu_{\text{Cu}} + 2\mu_{\text{HCOOH}} = \mu_{\text{Cu}(\text{HCOO})_2} + 2\mu_{\text{H}^+} + 2RT\ln[\text{H}^+] - 2FE$$

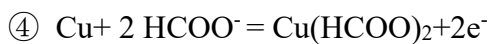
$$0 + 2 \times (-361.35 \times 10^3)$$

$$= (-636.3 \times 10^3) + 0 + 2 \times 2.3 \times 8.314 \times 298 \log[\text{H}^+]$$

$$- 2 \times 296500 \times E$$

$$E = \frac{86400 + 11396.8 \log[\text{H}^+]}{2 \times 96500}$$

$$E = 0.45 - 0.059 \text{pH}$$



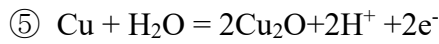
$$\mu_{\text{Cu}} + 2\mu_{\text{HCOO}^-} + 2RT\ln[\text{HCOO}^-] = \mu_{\text{Cu}(\text{HCOO})_2} - 2FE$$

$$0 + 2 \times (-351 \times 10^3) + 2 \times 2.3 \times 8.314 \times 298 \log[\text{HCOO}^-]$$

$$= (-636.3 \times 10^3) - 2 \times 296500 \times E$$

$$E = \frac{65700 + 11396.8 \log[\text{HCOO}^-]}{2 \times 96500}$$

$$E = 0.34 - 0.059 \log[\text{HCOO}^-]$$



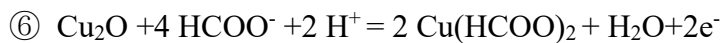
$$\mu_{\text{Cu}} + \mu_{\text{H}_2\text{O}} = 2\mu_{\text{Cu}_2\text{O}} + 2\mu_{\text{H}^+} + 2RT \ln[\text{H}^+] - 2FE$$

$$0 + (-237.129 \times 10^3)$$

$$= 2 \times (-146 \times 10^3) + 0 + 2 \times 2.3 \times 8.314 \times 298 \log[\text{H}^+] - 2 \times 296500 \times E$$

$$E = \frac{54871 + 11396.8 \log[\text{H}^+]}{2 \times 96500}$$

$$E = 0.471 - 0.059 \text{pH}$$



$$\mu_{\text{Cu}_2\text{O}} + 4\mu_{\text{HCOO}^-} + 4RT \ln[\text{HCOO}^-] + 2\mu_{\text{H}^+} + 2RT \ln[\text{H}^+] = \mu_{\text{Cu}(\text{HCOO})_2} + \mu_{\text{H}_2\text{O}}$$

$$(-146 \times 10^3) + 4 \times (-351 \times 10^3) + 4 \times (2.3 \times 8.314 \times 298 \log[\text{HCOO}^-]) + 0$$

$$+ 2 \times 2.3 \times 8.314 \times 298 \log[\text{H}^+]$$

$$= 2 \times (-636.3 \times 10^3) + (-237.129 \times 10^3) - 2 \times 96500 \times E$$

$$E = \frac{40271 - 22793.66 \log[\text{HCOO}^-] + 11396.8 \log[\text{H}^+]}{2 \times 96500}$$

$$E = 0.208 - 0.118 \log[\text{HCOO}^-] + 0.059 \text{pH}$$



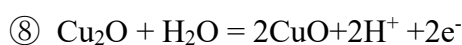
$$\mu_{\text{CuO}} + 2\mu_{\text{HCOO}^-} + 2RT \ln[\text{HCOO}^-] + 2\mu_{\text{H}^+} + 2RT \ln[\text{H}^+] = \mu_{\text{Cu}(\text{HCOO})_2} + \mu_{\text{H}_2\text{O}}$$

$$(-129.7 \times 10^3) + 2 \times (-351 \times 10^3) + 2 \times 2.3 \times 8.314 \times 298 \log[\text{HCOO}^-] + 0$$

$$+ 2 \times 2.3 \times 8.314 \times 298 \log[\text{H}^+] = (-636.3 \times 10^3) + (-237.129 \times 10^3)$$

$$41729 = 11396.8 \text{pH} - 11396.8 \log[\text{HCOO}^-]$$

$$\text{pH} = 3.66 - \log[\text{HCOO}^-]$$



$$\mu_{\text{Cu}_2\text{O}} + \mu_{\text{H}_2\text{O}} = \mu_{\text{CuO}} + 2\mu_{\text{H}^+} + 2RT \ln[\text{H}^+] - 2FE$$

$$(-146 \times 10^3) + (-237.129 \times 10^3)$$

$$= (-129.7 \times 10^3) + 0 + 2 \times 2.3 \times 8.314 \times 298 \log[H^+] - 2 \times 296500 \times E$$

$$E = \frac{123729 + 11396.8 \log[H^+]}{2 \times 96500}$$

$$E = 0.669 - 0.0591 \text{pH}$$

$$\textcircled{9} \frac{HCOOH}{HCOO^-}$$

$$\frac{HCOOH}{HCOO^-} \quad \text{pH} = 3.74$$

Acknowledgements

I would first like to express my sincere gratitude to my major supervisor, Professor Hideki Kawai, for his motivation, detail and immense knowledge, enthusiasm, for the continuous support of my doctoral study and research. All his kindness during my study in doctoral course have left a deep impression on my life. Also, thanks to Assistant Professor Yoshihiko Oishi for his support and help on my research

I would also like to express my highly appreciation to Professor Osami Seri, whose delightful personality and detailed knowledge about this research topic has guided me along the way. His encouragement, helpful, and patience suggestions will never ever be forgotten in my life.

I would like to thank to Professor Masashi Daimaruya and Professor Hiroyuki Fujiki for support in research and badminton club. I would also to thank to Associate Professor Masahiro Sakai and Assistant Professor Daichi Sasaki, for their support on my research about corrosion.

I would like to acknowledge the staff members of center for International relations. Deep appreciations are addressed to Mr. Jinro Endo, Ms. Hatsuki Noda, and Ms. Kozue Takekawa for helping me during staying in Muroran since 2014. I would like to acknowledge the members in Fluid Engineering Laboratory, Department of Mechanical Engineering, Muroran Institute of Technology. I enjoyed all the laboratory life since I entered this laboratory in 2014.

The scholarship supports by SGH Foundation Scholarship for Foreign Students 2018-2020 and JGC-S scholarship foundation 2017-2018 are highly appreciated.

I thank to my friends, Riki Hendra Purba, Wiyanti Fransisca Manulang, and also to Muroran Baptist Church member, for all the mental and spirit support.

I would like to thank my family: My father in heaven (+)Jaga Situmorang, My lovely Mother, Hermian Manihuruk, for all the support, pray, and the unconditional love. My sister and brother: Widya Yanti Situmorang, Jimmy Perianto Situmorang and Luhut Adi Irawan Situmorang, for the motivation, support and love.

Final and foremost, I would like to thank my Lord and Savior, Jesus Christ who has given me the strength, patience, and spirit to persevere my doctoral course. It was so tough for me in the first year of doctoral course. Hearth attack snatched my father from our family. It was hard for me to accept it. Not only that, I also could not extend my MEXT Scholarship for master course to doctoral course. But, God is rich with grace and mercy. He has not only provided for all of my needs but has given me everlasting life through his redemptive sacrifice on the cross. He is strengthening me day by day and cover me with his love by lovely people around me, my professor, my family, and my friends. I thank to God for this amazing doctoral course in my life.